Astronomy & Astrophysics

VLT/SPHERE imaging survey of the largest main-belt asteroids: Final results and synthesis[⋆,⋆⋆,⋆⋆⋆]

P. Vernazza[1], M. Ferrais[1], L. Jorda[1], J. Hanuš[2], B. Carry[3], M. Marsset[4], M. Brož[2], R. Fetick[1], M. Viikinkoski[5], F. Marchis[1,6], F. Vachier[7], A. Drouard[1], T. Fusco[1], M. Birlan[7,8], E. Podlewska-Gaca[9], N. Rambaux[7], M. Neveu[10], P. Bartczak[9], G. Dudziński[9], E. Jehin[11], P. Beck[12], J. Berthier[7], J. Castillo-Rogez[13], F. Cipriani[14], F. Colas[7], C. Dumas[15], J. Ďurech[2], J. Grice[16], M. Kaasalainen[5,†], A. Kryszczynska[9], P. Lamy[17], H. Le Coroller[1], A. Marciniak[9], T. Michalowski[9], P. Michel[3], T. Santana-Ros[18,19], P. Tanga[3], A. Vigan[1], O. Witasse[14], B. Yang[20], P. Antonini[21], M. Audejean[22], P. Aurard[23], R. Behrend[24,25], Z. Benkhaldoun[24,25], J. M. Bosch[26], A. Chapman[27], L. Dalmon[23], S. Fauvaud[28,29], Hiroko Hamanowa[30], Hiromi Hamanowa[30], J. His[23], A. Jones[31], D.-H. Kim[32,33], M.-J. Kim[32], J. Krajewski[34], O. Labrevoir[23], A. Leroy[35,36], F. Livet[37], D. Molina[38], R. Montaigut[39,35], J. Oey[40], N. Payre[23], V. Reddy[41], P. Sabin[23], A. G. Sanchez[42], and L. Socha[43]

(Affiliations can be found after the references)

ABSTRACT

Context. Until recently, the 3D shape, and therefore density (when combining the volume estimate with available mass estimates), and surface topography of the vast majority of the largest ($D \geq 100$ km) main-belt asteroids have remained poorly constrained. The improved capabilities of the SPHERE/ZIMPOL instrument have opened new doors into ground-based asteroid exploration.

Aims. To constrain the formation and evolution of a representative sample of large asteroids, we conducted a high-angular-resolution imaging survey of 42 large main-belt asteroids with VLT/SPHERE/ZIMPOL. Our asteroid sample comprises 39 bodies with $D \geq 100$ km and in particular most $D \geq 200$ km main-belt asteroids (20/23). Furthermore, it nicely reflects the compositional diversity present in the main belt as the sampled bodies belong to the following taxonomic classes: A, B, C, Ch/Cgh, E/M/X, K, P/T, S, and V.

Methods. The SPHERE/ZIMPOL images were first used to reconstruct the 3D shape of all targets with both the ADAM and MPCD reconstruction methods. We subsequently performed a detailed shape analysis and constrained the density of each target using available mass estimates including our own mass estimates in the case of multiple systems.

Results. The analysis of the reconstructed shapes allowed us to identify two families of objects as a function of their diameters, namely "spherical" and "elongated" bodies. A difference in rotation period appears to be the main origin of this bimodality. In addition, all but one object (216 Kleopatra) are located along the Maclaurin sequence with large volatile-rich bodies being the closest to the latter. Our results further reveal that the primaries of most multiple systems possess a rotation period of shorter than 6 h and an elongated shape ($c/a \leq 0.65$). Densities in our sample range from ~1.3 g cm^{-3} (87 Sylvia) to ~4.3 g cm^{-3} (22 Kalliope). Furthermore, the density distribution appears to be strongly bimodal with volatile-poor ($\rho \geq 2.7$ g cm^{-3}) and volatile-rich ($\rho \leq 2.2$ g cm^{-3}) bodies. Finally, our survey along with previous observations provides evidence in support of the possibility that some C-complex bodies could be intrinsically related to IDP-like P- and D-type asteroids, representing different layers of a same body (C: core; P/D: outer shell). We therefore propose that P/D-types and some C-types may have the same origin in the primordial trans-Neptunian disk.

Key words. minor planets, asteroids: general – methods: observational – techniques: high angular resolution

1. Introduction

Before the advent of the SPHERE/ZIMPOL instrument at the VLT (Beuzit et al. 2019), only a handful of the largest main-belt asteroids (e.g., (1) Ceres, (2) Pallas, (4) Vesta, (52) Europa, (511) Davida) had been the subject of in-depth studies using the first-generation high-angular-resolution imaging systems operating in the optical (HST) or in the near-infrared (NIR; VLT/NACO, Keck/NIRC2) (e.g., Thomas et al. 1997, 2005; Conrad et al. 2007; Carry et al. 2008, 2010; Schmidt et al. 2009; Merline et al. 2013). Although sparse, VLT/NACO and Keck/NIRC2 imaging data had been collected for many $D \geq 100$ km asteroids, these data were rarely acquired with excellent seeing conditions and/or when the targets were at opposition, leading to suboptimal resolution for the observations of these bodies (Hanuš et al. 2017). It follows that until recently, the 3D shape, and therefore density, (when combining the volume estimate with available mass estimates) and surface topography of the vast majority of the largest ($D \geq 100$ km) main-belt asteroids have remained poorly constrained. The improved capabilities of the SPHERE/ZIMPOL instrument operating at the diffraction limit in the optical (angular resolution of ~20 mas at 600 nm) have opened new doors into

---

ground-based asteroid exploration, enabling investigation of the following fundamental questions:

- What is the diversity in shape among large asteroids and are the shapes close to equilibrium?
- How do large impacts affect asteroid shape?
- What is the bulk density of large asteroids and is there a relationship with their surface composition? Is there any evidence of differentiation among those bodies?
- Is the density of those bodies that are predicted to be implanted bodies from the outer Solar System (P/D-types) compatible with that of small ($D \leq 300$ km) trans-Neptunian objects?
- What physical properties drive the formation of companions around large asteroids?

To shed some light on these questions, as part of an ESO large programme (199.C-0074; PI: P. Vernazza) conducted between May 2017 and September 2019, we have been carrying out disk-resolved observations with SPHERE/ZIMPOL of a substantial fraction of all $D \geq 200$ km main-belt asteroids (20 of 23 objects) throughout their rotation. The three $D \geq 200$ km asteroids absent from our list are 65 Cybele, 107 Camilla (already observed with SPHERE by Pajuelo et al. 2018), and 451 Patientia. Our survey also comprised 19 asteroids with 100 km $\leq D \leq 200$ km and 3 objects with 85 km $\leq D \leq 100$ km. Importantly, our survey covered the main compositional classes present in the main belt (A, B, C, Ch/Cgh, E/M/X, K, P/T, S, V; DeMeo et al. 2009).

So far, several targets of our observing program have already been the subject of dedicated papers (Vernazza et al. 2018; Viikinkoski et al. 2018; Fétick et al. 2019; Carry et al. 2019, 2021; Hanuš et al. 2019, 2020; Yang et al. 2020b; Ferrais et al. 2020; Marsset et al. 2020; Dudziński et al. 2020; Marchis et al. 2021; Brož et al. 2021) and we briefly summarize some of these findings below.

Our observations of (4) Vesta have allowed us to recover most of the main topographic features present across its surface, unveiled by the NASA Dawn mission (Fétick et al. 2019). This includes the south pole impact basin and its prominent central peak, several $D \geq 25$ km-sized craters, and also Matronalia Rupes, including its steep scarp and its small and large arcs. Observations of (2) Pallas have revealed a heavily cratered "golf ball-like" surface that is most likely the consequence of its high inclination and eccentricity, which imply high-impact velocities on that body (Marsset et al. 2020). (10) Hygiea observations have revealed a basin-free spherical shape while it suffered a catastrophic disruption, which is at the origin of one of the largest asteroid families (Vernazza et al. 2020). Observations of (16) Psyche, the target of a forthcoming NASA discovery mission, imply a primordial shape close to that of a Jacobi ellipsoid and a density compatible with that of stony-iron meteorites (Viikinkoski et al. 2018; Ferrais et al. 2020). Observations of (31) Euphrosyne, the tenth largest asteroid, allowed the discovery of a satellite (Yang et al. 2020b) and observations of (41) Daphne and (87) Sylvia, two multiple systems, imply a homogeneous internal structure in the first case and a differentiated interior for Sylvia (Carry et al. 2019, 2021). Observations of (89) Julia, a $D \sim 140$ km S-type asteroid and the parent body of a small collisional family that consists of 66 known members with $D < 2.5$ km, have revealed the presence of an impact crater (~75 km wide) that could be the origin of this family (Vernazza et al. 2018). This particular case illustrates the progress made since the discovery by HST of Vesta's south pole impact basin at the origin of its family. Finally, (216) Kleopatra observations

have allowed us to substantially revise its mass and volume estimates (Marchis et al. 2021; Brož et al. 2021). Furthermore, we showed that Kleopatra is the largest critically rotating asteroid, with the surface corresponding to the L1 equipotential.

Here, we report all the data that have been acquired by our large programme, namely SPHERE/ZIMPOL images for 42 targets. These images have been used to reconstruct the 3D shape of all targets with both the All-Data Asteroid Modeling (ADAM) and the Multi-resolution PhotoClinometry by Deformation (MPCD) reconstruction methods (Capanna et al. 2013; Viikinkoski et al. 2015a; Jorda et al. 2016). We then present a shape analysis of our target sample as well as our best estimate of the density of our targets. Finally, we use these constraints to provide partial answers to the questions listed above.

2. Observations

The baseline observational strategy adopted for our large programme has been to image each target with SPHERE/ZIMPOL (i) around opposition to ensure an optimal spatial resolution (we restricted the observing period so that its angular diameter remained greater than at least 85% of that at opposition), (ii) every ~60° in rotation phase in order to obtain a satisfactory surface coverage, and (iii) with seeing conditions of better than 0.8″ and an airmass of below 1.6 in order to ensure great observing conditions and thus high-quality data. To fulfil these criteria and given that large programmes have the highest priority at ESO, we performed our large programme entirely in service mode. We would like to stress that this strategy has been key to the success of our programme.

Our full set of images provides a satisfactory rotational coverage (at least four epochs per target, with the objective being six epochs per target) for 39 asteroids (see Table A.2 for a complete list of all observations). All ZIMPOL observations were obtained in the narrowband imaging configuration (N_R filter; filter central wavelength = 645.9 nm, width = 56.7 nm). The observing strategy has been the same for all targets within our ESO large programme, namely the asteroid target was used as a natural guide star for AO correction during each series of images (five images per epoch).

These images were subsequently reduced (see Vernazza et al. 2018 for a description of the data-reduction steps) and deconvolved with the MISTRAL algorithm (Fusco et al. 2003; Mugnier et al. 2004) using a point-spread function (PSF). At the beginning of our observing programme, we were observing a stellar PSF either before or just after every asteroid observation. However, because the deconvolution with the stellar PSF was not systematically producing satisfactory results, we investigated alternative methods to increase the sharpness of the image. We noticed that in several cases, we reached a better result by using stellar PSFs acquired on different nights. We therefore tested the deconvolution process with synthetic PSFs modeled by a 2D Moffat function. The deconvolution always converged towards an acceptable solution by varying the Moffat parameters (Fétick et al. 2019). We therefore switched to a systematically parametric PSF to deconvolve our images (e.g., Fétick et al. 2019; Viikinkoski et al. 2018). Notably, the case of Vesta has confirmed the accuracy of our image-deconvolution algorithm (Fétick et al. 2019). Overall, the use of a parametric PSF has been highly beneficial for our programme as it left more observing time for our asteroid targets. In Fig. 1, we show one deconvolved image of every large programme target whereas Fig. A.1 shows one image per epoch for each target.
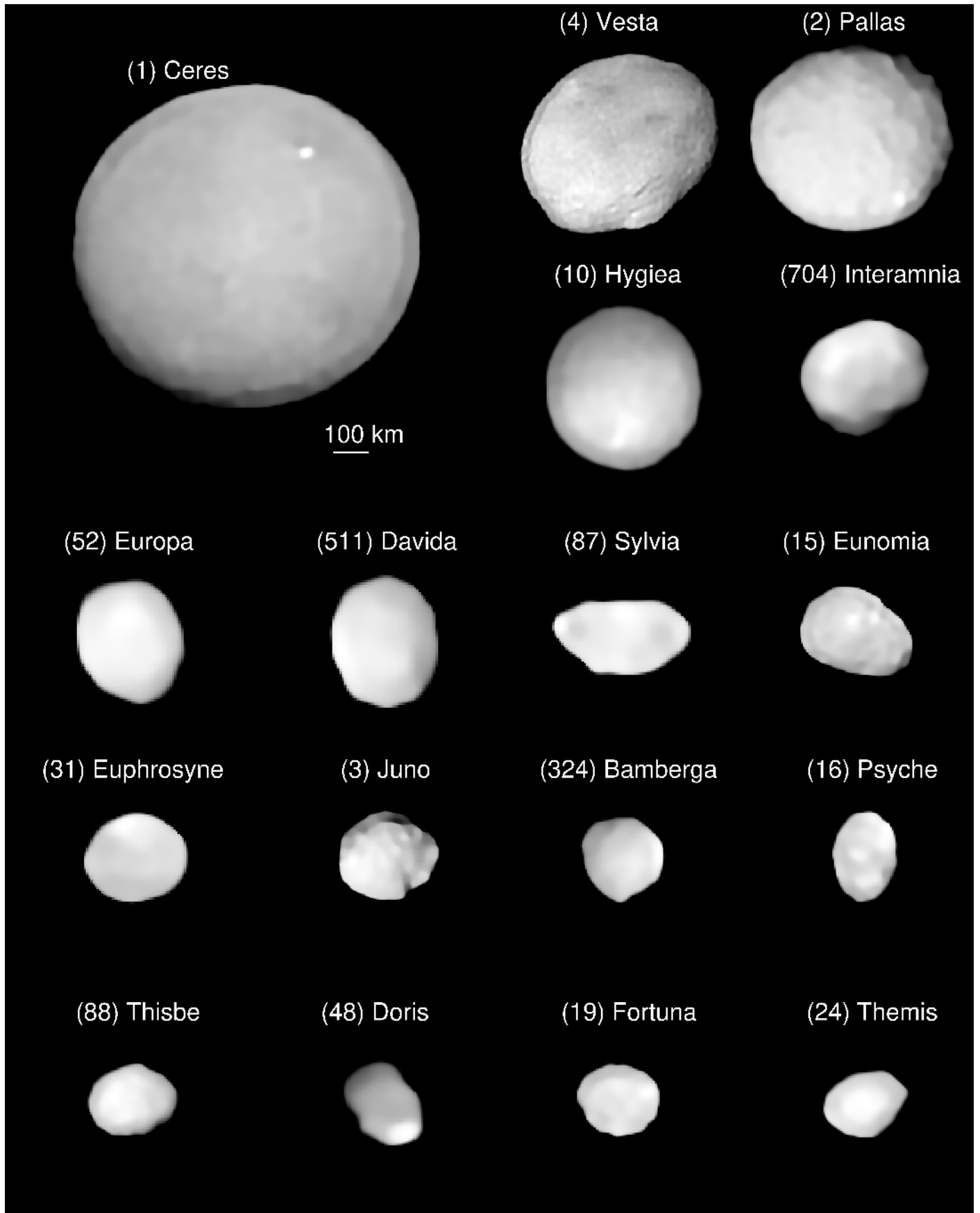
Fig. 1. (*A*) VLT/SPHERE images of all *D* > 210 km asteroid targets deconvolved with the MISTRAL algorithm (Fusco et al. 2003). The relative sizes are respected, and the scale is indicated on the plot. The objects are ordered according to decreasing values of their volume equivalent diameter.
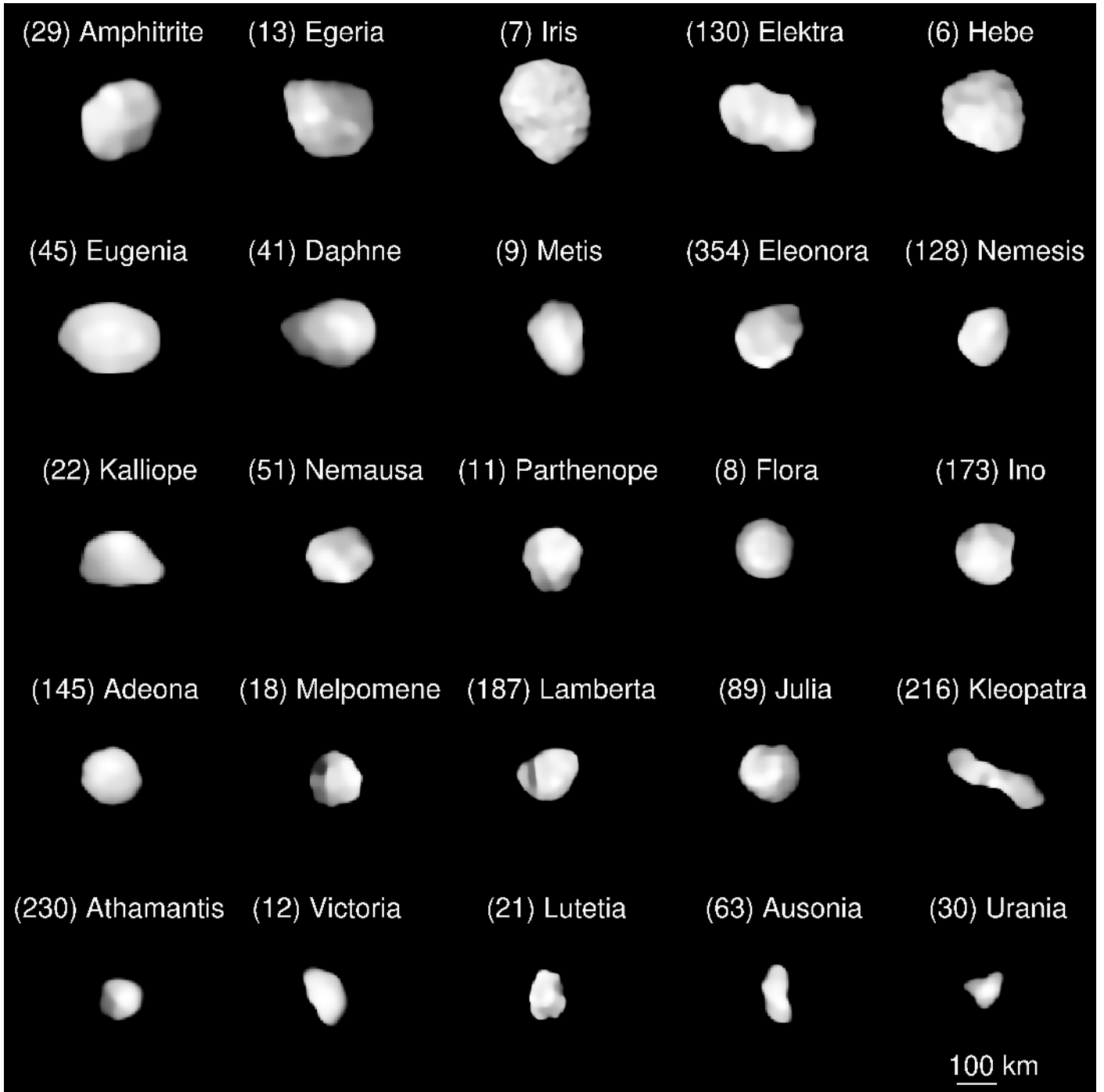
Fig. 1. continued. (*B*) VLT/SPHERE deconvolved images of all *D* < 210 km asteroid targets with the MISTRAL algorithm (Fusco et al. 2003).

3. Determination of the 3D shape

Reconstruction of the 3D shape of our targets has always followed a well-defined scheme. Our SPHERE data along with light curve data have been used to constrain the rotational parameters (spin axis and period) and have allowed us to reconstruct a first 3D shape of every target with the ADAM model (Viikinkoski et al. 2015a). We used all available "dense-in-time" light curves from the DAMIT[1] database (Ďurech et al. 2010) and supplemented them with additional data either from a different source (such as ALCDEF[2]) or based on our new observations. All light-curve data that were used for the reconstruction and that are not included in DAMIT are listed in Table A.3. We excluded the "sparse-in-time" data from surveys such as the Catalina Sky Survey for their redundancy as rich dense datasets are usually available. A large fraction of the listed data are based on observations from the SuperWASP survey that were processed by Grice et al. (2017). Photometry for several asteroids was obtained by the TRAPPIST telescopes (Jehin et al. 2011) and through the

---

[1] https://astro.troja.mff.cuni.cz/projects/damit/

[2] https://minplanobs.org/alcdef/

Gaia-GOSA[3] observing campaign. The strength of the ADAM model is that it makes use of all types of data (light curves but also stellar occultations when available), not just AO data. Given that the SPHERE data provide only a partial surface coverage for most of our targets, light-curve data were often necessary to constrain the uncovered aspect angles. We note that the SAGE model (Bartczak & Dudziński 2018), improved over the course of our large programme, has now the same type of strength as the ADAM model as it can constrain the spin axis and reconstruct the 3D shape of an asteroid using not only light curves but also AO data (Dudziński et al. 2020). We note that the SAGE model was key in constraining the rotational parameters of two targets (128 Nemesis and 324 Bamberga), illustrating the benefit of having multiple reconstruction methods.

The 3D shape produced with the ADAM model was subsequently used as input to the MPCD model (Capanna et al. 2013). The strength of the MPCD method with respect to the ADAM or SAGE models is that it tries to capture small topographic details from the high-resolution SPHERE images. Unlike the ADAM and SAGE approaches, the MPCD method was designed for space missions and uses only SPHERE data along with a decimated version of the ADAM model as input. It is therefore not surprising that the images generated with the MPCD models using the OASIS software (Jorda et al. 2010) usually show the smallest residuals with respect to the SPHERE images (Appendix B). Nonetheless, the ADAM and MPCD models are systematically very close to each other and the rms residuals between the volume equivalent diameters estimated with both methods amounts to 1.6 km (0.8%). We also calculated the difference between the ADAM and MPCD equivalent diameters of all our targets to search for a possible bias between the two methods. The result amounts to ~1.0 km, excluding a significant bias.

Importantly, our VLT/SPHERE observations of (1) Ceres (5 epochs) and (4) Vesta (6 epochs), targets of the Dawn mission, provide a direct demonstration of the accuracy of our approach. Despite the limited number of images for both objects, our inferred dimensions (a, b, c and the volume equivalent diameter) are accurate to within less than 3% and our derived volumes are accurate to within less than 0.4% of those derived from the Dawn observations (Russell et al. 2012, 2016). Although Ceres and Vesta are the two main-belt asteroids with the largest angular diameter, we are confident that our volume estimates for the remaining large programme targets should reach uncertainties of a few percent at most ($\leq$10%). Indeed, our inferred values for the volume equivalent diameter of (21) Lutetia (one of the smallest targets within our observing programme) with the ADAM ($D = 100 \pm 2$ km) and MPCD ($D = 98 \pm 2$ km) models are compatible with that derived from the Rosetta observations ($D = 98 \pm 2$ km) (Sierks et al. 2011).

Finally, we computed the geometric albedo of our targets using our diameter estimates in tandem with the most recent estimates of the absolute magnitude of these bodies (see Table 1).

4. Shape analysis

The analysis of the shape of our targets was performed in the same way as described in Vernazza et al. (2020) and Ferrais et al. (2020). First, we calculated the sphericity index (Wadell 1935) of all targets, the latter being a function of the surface area and of

---

[3] http://www.gaiagosa.eu/
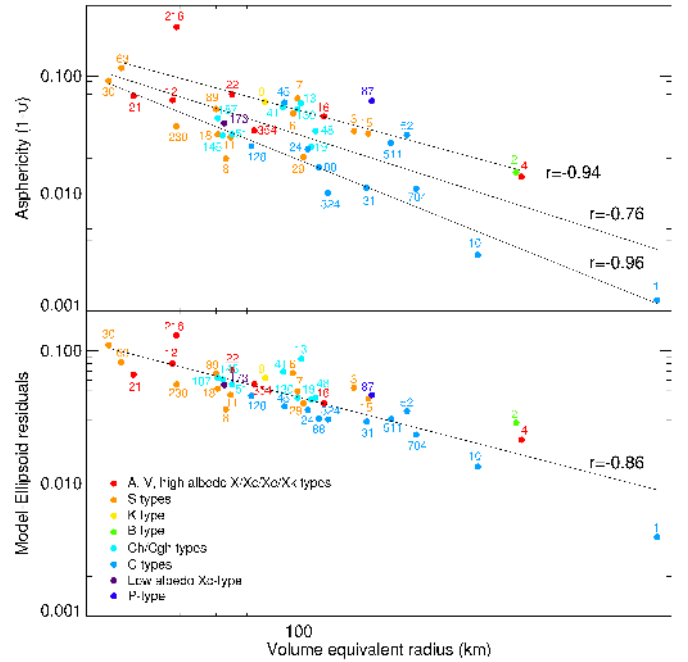
Fig. 2. *Upper panel*: asphericity of our large programme targets as a function of their volume equivalent radius. Both quantities appear highly correlated whereas the distribution of the asphericity as a function of target radius appears bimodal at first order (see Fig. 3). The correlation coefficient increases significantly when each subsample is considered separately. *Lower panel*: departure of the shape of our targets from their best-fit ellipsoid as a function of their volume equivalent radius. As in the case of the asphericity, both quantities appear highly correlated.

the volume. Second, we computed the radial differences between the shape models of our targets and their best-fitting ellipsoid, and derived the (model – ellipsoid) average residual relative to the mean radius (in %) for every object. The sphericity index as well as the (model – ellipsoid) average residual are reported for every target as a function of their volume equivalent radius in Fig. 2. A very strong correlation appears between both quantities and the volume equivalent radius of our targets ($r = -0.76$ and $r = -0.86$ for $N = 42$ implying a >99.95% confidence level that these correlations are not random). These correlations demonstrate that the size, and therefore the mass, is a key factor in determining the main aspects of the 3D shape of an asteroid (for the considered range of diameters).

Furthermore, the distribution of the sphericity index of our asteroid sample as a function of the volume equivalent radius appears to be bimodal at first order (see Fig. 3) and not continuous or unimodal. For each size bin, there appears to be a group of more spherical bodies and a group of more elongated objects (hereafter "spherical" and "elongated"). The dip test (Hartigan & Hartigan 1985), which measures multimodality in a sample by the maximum difference, over all sample points between the empirical distribution function and the unimodal distribution function that minimizes that maximum difference gives a 99.4% confidence level against unimodality. Of importance, all objects that are the largest remnants of a catastrophic disruption and thus likely formed via reaccumulation ((8) Flora, (10) Hygiea, (31) Euphrosyne) belong to the spherical group.

As the angular momentum is the determining factor of the oblateness of an object provided that it formed as a fluid (likely the case for many of our targets; see discussion), we first compared the c/a axes ratio of all targets to their rotation period. It

Table 1. Taxonomic type, volume-equivalent diameter (D), mass (m), density (ρ), geometric albedo, and c/a ratio of our large programme targets.

	Asteroid	Class	Family (F) Satellite (S)	D [km]	m [10^{18} kg]	ρ [g cm^{-3}]	Albedo	c/a
1	Ceres [*]	C		939.4 ± 0.2	938.40 ± 0.01	2.161 ± 0.001	0.096	0.9247 ± 0.0003
2	Pallas	B	F	511 ± 4	204.2 ± 2.7	2.92 ± 0.08	0.155	0.79 ± 0.03
3	Juno	S	F	254 ± 2	27.0 ± 2.4	3.15 ± 0.28	0.202	0.78 ± 0.02
4	Vesta [*]	V	F	523.2 ± 0.2	259.0 ± 0.1	3.453 ± 0.004	0.38	0.7769 ± 0.0004
6	Hebe	S		195 ± 3	12.4 ± 2.4	3.18 ± 0.64	0.268	0.75 ± 0.04
7	Iris	S		199 ± 10	13.5 ± 2.3	3.26 ± 0.74	0.279	0.58 ± 0.07
8	Flora	S	F	146 ± 2	4.0 ± 1.6	2.4 ± 1.0	0.224	0.82 ± 0.05
9	Metis	K		173 ± 2	8.0 ± 1.9	2.94 ± 0.70	0.18	0.61 ± 0.05
10	Hygiea	C	F	433 ± 8	87.4 ± 6.9	2.06 ± 0.20	0.063	0.94 ± 0.05
11	Parthenope	S	F	149 ± 2	5.5 ± 0.4	3.20 ± 0.27	0.187	0.88 ± 0.05
12	Victoria	A		116 ± 2	2.7 ± 1.3	3.4 ± 1.7	0.167	0.69 ± 0.03
13	Egeria	Ch		202 ± 3	9.2 ± 2.1	2.13 ± 0.49	0.087	0.76 ± 0.06
15	Eunomia	S		270 ± 3	30.5 ± 1.9	2.96 ± 0.21	0.187	0.67 ± 0.05
16	Psyche	M/Xk		223 ± 3	22.6 ± 2.9	3.89 ± 0.53	0.155	0.59 ± 0.02
18	Melpomene	S		141 ± 2	4.5 ± 0.9	3.06 ± 0.62	0.221	0.81 ± 0.06
19	Fortuna	Ch		211 ± 2	8.8 ± 1.4	1.80 ± 0.29	0.056	0.79 ± 0.05
21	Lutetia [*]	M/Xc		98 ± 2	1.70 ± 0.02	3.45 ± 0.21	0.194	0.65 ± 0.03
22	Kalliope	M/X	S	150 ± 5	7.7 ± 0.4	4.36 ± 0.50	0.198	0.59 ± 0.02
24	Themis	C	F	208 ± 3	6.2 ± 2.9	1.31 ± 0.62	0.06	0.76 ± 0.08
29	Amphitrite	S		204 ± 2	12.7 ± 2.0	2.86 ± 0.45	0.194	0.82 ± 0.03
30	Urania	S		88 ± 2	1.3 ± 0.9	3.7 ± 2.7	0.214	0.68 ± 0.05
31	Euphrosyne	C	F/S	268 ± 4	16.5 ± 2.6	1.64 ± 0.27	0.05	0.86 ± 0.07
41	Daphne	Ch	S	187 ± 13	6.1 ± 0.9	1.78 ± 0.45	0.052	0.65 ± 0.08
45	Eugenia	C	S	188 ± 2	5.8 ± 0.1	1.66 ± 0.07	0.065	0.55 ± 0.03
48	Doris	Ch		215 ± 3	6.9 ± 2.9	1.32 ± 0.55	0.066	0.72 ± 0.01
51	Nemausa	Cgh		150 ± 3	3.9 ± 1.6	2.2 ± 0.9	0.09	0.77 ± 0.04
52	Europa	C		319 ± 4	23.9 ± 3.8	1.41 ± 0.23	0.052	0.67 ± 0.04
63	Ausonia	S		93 ± 3	1.2 ± 0.2	2.96 ± 0.61	0.195	0.45 ± 0.02
87	Sylvia	X/P	F/S	274 ± 4	14.3 ± 0.5	1.33 ± 0.07	0.04	0.53 ± 0.02
88	Thisbe	C		218 ± 3	11.6 ± 2.2	2.14 ± 0.42	0.057	0.81 ± 0.07
89	Julia	S	F	140 ± 3	4.3 ± 3.2	3.0 ± 2.2	0.216	0.7 ± 0.03
128	Nemesis	C	F	163 ± 5	3.4 ± 1.7	1.5 ± 0.8	0.067	0.83 ± 0.04
130	Elektra	Ch	S	199 ± 2	6.4 ± 0.2	1.55 ± 0.07	0.067	0.57 ± 0.04
145	Adeona	Ch	F	144 ± 3	2.4 ± 0.3	1.52 ± 0.21	0.048	0.92 ± 0.03
173	Ino	Xc		145 ± 3	2.2 ± 1.3	1.4 ± 0.8	0.061	0.76 ± 0.06
187	Lamberta	Ch		141 ± 2	1.9 ± 0.3	1.28 ± 0.22	0.052	0.86 ± 0.07
216	Kleopatra	M/Xe	S	118 ± 2	3.0 ± 0.3	3.45 ± 0.41	0.152	0.18 ± 0.02
230	Athamantis	S		118 ± 2	2.3 ± 1.1	2.7 ± 1.3	0.146	0.76 ± 0.07
324	Bamberga	C		227 ± 3	10.2 ± 0.9	1.67 ± 0.16	0.06	0.96 ± 0.05
354	Eleonora	A		165 ± 3	7.5 ± 2.7	3.18 ± 1.14	0.172	0.75 ± 0.08
511	Davida	C		298 ± 4	26.6 ± 7.3	1.92 ± 0.53	0.063	0.7 ± 0.06
704	Interamnia	C		332 ± 5	35.2 ± 5.1	1.84 ± 0.28	0.067	0.86 ± 0.03

Notes. Uncertainties correspond to 1σ values. We also highlight the bodies visited by spacecraft [*], that are members of a collisional family (F) or that possess one or two satellites (S). Apart from the three targets visited by a space mission (Ceres, Vesta and Lutetia), all reported values were derived in the present study.

appears that both quantities are correlated ($r = 0.48$ for $N = 42$, a 99.7% confidence level that this correlation is not random; Fig. 4). We notice that multiple systems tend to possess a rotation period below 6 h and a c/a axis ratio ≤ 0.65 (except 31 Euphrosyne). We also compared the distribution of the rotation period within the two groups of the bimodality (Fig. 5). It appears that on average, elongated objects possess a shorter rotation period (average: 6.4 h) with respect to more spherical bodies (average: 12.2 h). In particular, 16 out of the 18 ($\sim$89%) more elongated objects possess a rotation period of shorter than 8 h. However, the distribution of the more spherical bodies appears

to be flat. This raises some questions regarding the origin of the spherical shape of some rapidly rotating bodies as for example in the case of (31) Euphrosyne (Yang et al. 2020b).

Finally, we compare the specific angular momentum and the normalized angular velocity of our targets (Descamps 2015) with the expected values for Maclaurin and Jacobi ellipsoids as well as dumb-bell shapes (Fig. 6). It appears that all but one of the bodies fall along the Maclaurin sequence. The only body falling onto the dumb-bell sequence is 216 Kleopatra. Next, we computed both the mean distance in the H and Ω space (md) and the reduced chi-square to evaluate the impact of the
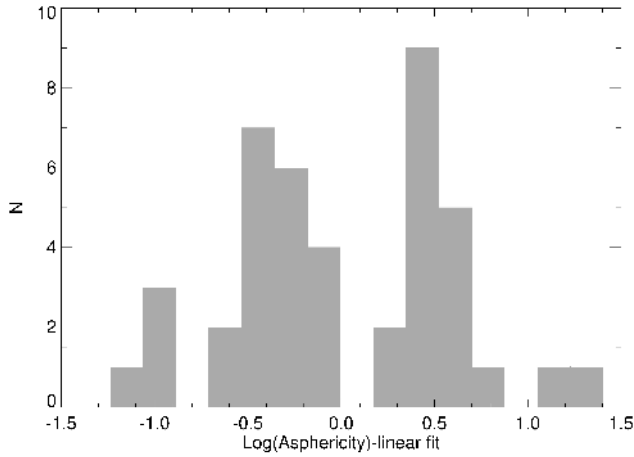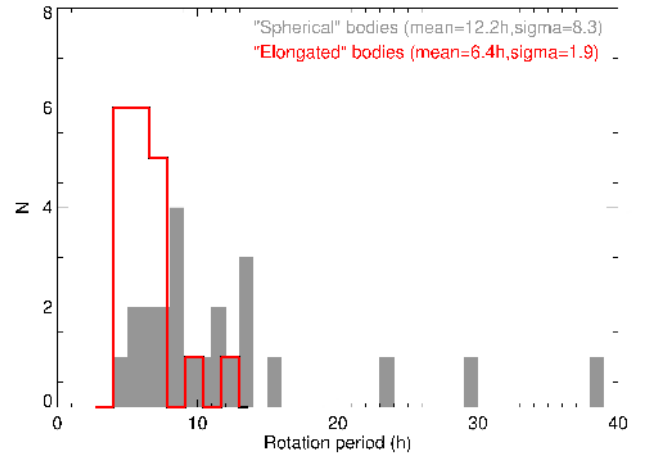
Fig. 3. Histogram of the distance between the asphericity of our targets and the linear best fit to the whole sample. The distribution appears bimodal at first order and the dip test rejects the unimodality of the distribution with a 99% confidence level.
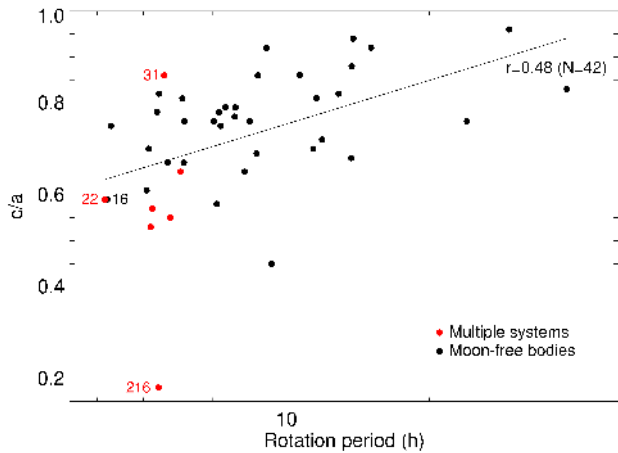
Fig. 4. Relationship between the rotation period of large asteroids and their oblateness (c/a ratio). We observe a linear relation between both physical properties with a correlation coefficient of $r = 0.48$ ($N = 42$), a 99.8% confidence level that this correlation is not random. All multiple systems observed within our programme possess a rotation period of below 6 h and a c/a axis ratio of below 0.65 except (31) Euphrosyne.

Fig. 5. Distribution of the rotation period of "elongated" and "spherical" bodies (see text). All but two "elongated" bodies possess a rotation period shorter than 8 h.

shape, bulk composition (density), and size on the distance of the bodies to the Maclaurin sequence. Concerning the calculation of the reduced chi-square, we removed both Ceres and Vesta from the computation because of their extremely small error bars compared to the other objects. It is interesting to note that:

– Spherical bodies (md = 0.017; $\chi^2 = 0.36$) tend to be closer to the Maclaurin sequence than elongated bodies (md = 0.035; $\chi^2 = 1.69$).
– Low-density ($\rho \leq 2.2$ g cm^{-3}) volatile-rich bodies (md = 0.017; $\chi^2 = 0.77$) tend to be closer to the Maclaurin sequence than volatile-poor bodies with $\rho \geq 2.7$ g cm^{-3} (md = 0.033; $\chi^2 = 1.12$).
– Bodies with volume-equivalent diameters above 200 km (md = 0.022; $\chi^2 = 0.63$) tend to be closer to the Maclaurin sequence than bodies with a volume-equivalent diameter of less than 200 km (md = 0.030; $\chi^2 = 1.21$).

– In spite of large error bars, it appears that most objects in our sample (31/41) fall below the Maclaurin equilibrium curve.

To ascertain that the bulk composition (density) and mass are both determining factors in the distance to the Maclaurin sequence, we computed the chi-square for $D \geq 200$ km bodies ($N = 18$) by first removing four volatile-poor ($\rho \geq 2.7$ g cm^{-3}) bodies and then four volatile-rich ($\rho \leq 2.2$ g cm^{-3}) bodies. In the first case, the chi-square decreases to ~0.21, a value three times lower than that of the whole sample. In the second case, the chi-square increases to ~0.80, a value ~1.27 times greater than that of the whole sample. This highlights the small contribution of volatile-rich bodies to the overall chi-square and the large contribution of volatile-poor bodies to the latter. Of great interest, there is a small fraction of bodies that appear the closest ($\chi^2 = 0.0064$) to the Maclaurin sequence, namely large ($D \geq 220$ km) volatile-rich bodies (excluding 31 Euphrosyne from the sample which is an odd case). This subpopulation (10 Hygiea, 24 Themis, 88 Thisbe, 324 Bamberga, 704 Interamnia), which only comprises spherical bodies, appears to be the main origin of the md and chi-square differences illustrated in the three panels of Fig. 6. In conclusion, both the bulk density (hence composition) and the mass of a body appear to be determining factors in its distance to the Maclaurin equilibrium figure with large volatile-rich bodies being by far the closest to the sequence.

5. Density

We computed the density of all targets using an average of available mass estimates and our derived volume equivalent diameters (Fig. 7). The volume equivalent diameters were determined as follows. For those targets whose surface coverage was lower than 80%, we relied on the ADAM diameter value only, whereas for the remaining cases (coverage ≥80%) we computed the average of the ADAM and MPCD diameters. The mass estimates were determined as follows. For those objects with a large number of available mass estimates (≥10), we included only the values within two sigma of the mean. For those objects with fewer estimates, we removed outlier values. In the case of three targets ((8) Flora, (128) Nemesis, (173) Ino) with mass estimates following a bimodal distribution, we selected the peak corresponding to the most meaningful density rather than the average value.
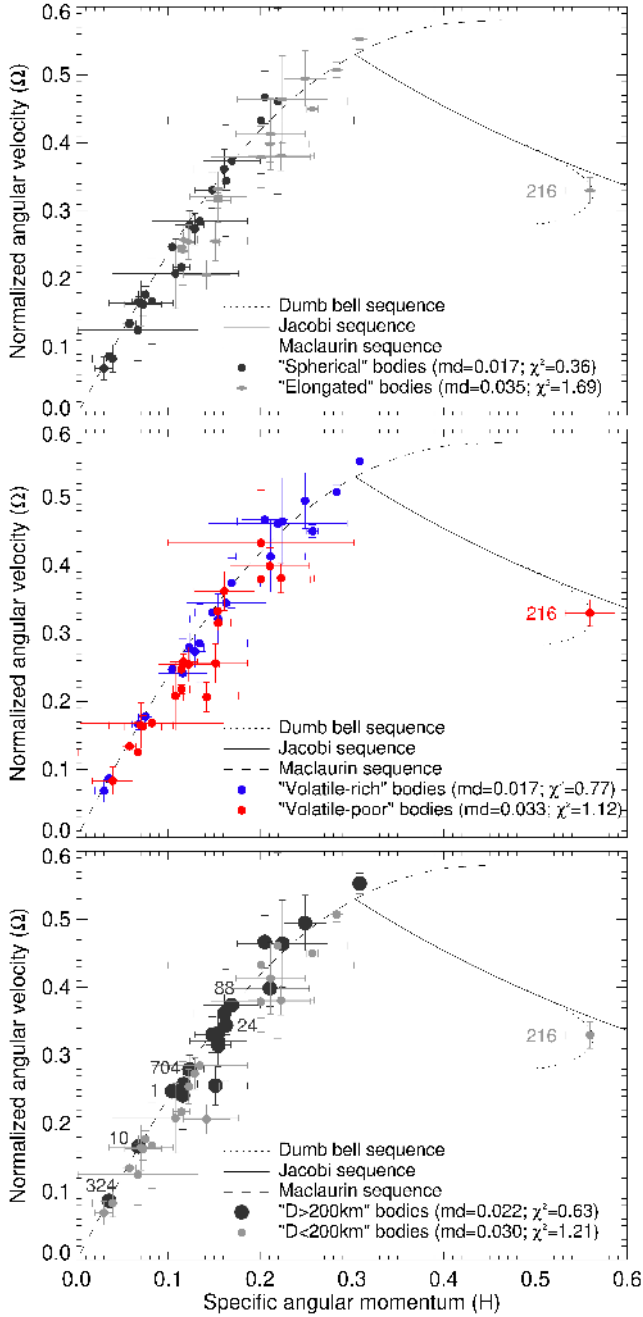
Fig. 6. Comparison of the specific angular momentum and the normalized angular velocity of our targets with the expected values for Maclaurin and Jacobi ellipsoids as well as dumb-bell shapes. Our targets are successively grouped as a function of their oblateness (*upper panel*), volatile content (*middle panel*), and size (*lower panel*). Both the mean distance (md) and chi-square of each group with respect to the Maclaurin sequence are indicated in each panel. We note that (216) Kleopatra is not included in these calculations. Large volatile-rich spherical bodies that fall very close to the Maclaurin sequence are highlighted in the bottom panel.

In most cases (asteroids without a companion), the error in density is largely dominated by the uncertainty of the mass estimate. We note that we added two $D \geq 150$ km targets that are not part of the large programme (C-type (93) Minerva and P-type (107) Camilla; Marchis et al. 2013; Hanuš et al. 2017; Pajuelo et al. 2018) to Fig. 7 to slightly improve the statistics. The

density values for these two objects are robust given that they are multiple systems with well-defined masses and volumes.

Densities in our sample range from ∼1.3 g cm^{-3} (P-type asteroids (87) Sylvia and (107) Camilla) to ∼4.3 g cm^{-3} (M/X-type asteroid (22) Kalliope), highlighting the wide diversity in composition of the asteroid belt. Notably, there is a clear difference in density (nearly a factor of two) between bodies affiliated to volatile-poor meteorites ($\rho_{mean} = 3.26$ g cm^{-3} for A-, V-, high albedo X-, Xc-, Xe-, Xk- and S-type asteroids that are related to achondrites, stony iron meteorites, CB, CH, enstatite, and ordinary chondrites; Vernazza & Beck 2017) and bodies related to volatile-rich meteorites (CI/CM chondrites) and/or interplanetary dust particles ($\rho_{mean} = 1.69$ g cm^{-3} for C-, Cgh-/Ch- and P-type asteroids; Vernazza et al. 2015a; Vernazza & Beck 2017). This dichotomy in density is confirmed by applying the dip test to our sample which gives a 99.1% confidence level against unimodality. Given that asteroid albedos also follow a bimodal distribution (Masiero et al. 2011), two main groups of asteroids emerge (Fig. 8), namely (a) asteroids with a geometric albedo below 0.1 and a density below 2.2 g cm^{-3} and (b) asteroids with a geometric albedo higher than 0.145 and a density greater than 2.7 g cm^{-3}. A simple explanation for this dichotomy may be the chondrule versus matrix content of these bodies. Indeed, low-albedo asteroids (C, P, D) have been mostly associated (based on spectroscopic observations) with chondrule-poor matrix-rich extra-terrestrial materials (CI and CM chondrites, Tagish Lake, IDPs) whose bulk density is significantly lower than that of chondrule-rich meteorites. Conversely, chondrule-rich extra-terrestrial materials (ordinary chondrites, enstatite chondrites, but also CV/CK chondrites) have been associated with asteroid types (S, E, M, K) that usually possess a geometric albedo of greater than 0.14. In short, the relative abundance of matrix and chondrules is perhaps the main origin of the observed dichotomy in addition to the carbon and volatile content.

As a next step, we computed the average and rms density of the main compositional classes (see Fig. 7). To estimate the amount of macroporosity within large asteroids, we restricted ourselves to the mean density of two major compositional classes (S and Ch/Cgh) that possess a well-identified meteoritic analog and that supposedly did not differentiate (Vernazza et al. 2014; Carry et al. 2019). Specifically, we assumed that ordinary chondrites are the meteoritic analogs of S-type asteroids (Vernazza et al. 2014, 2015b) and CM chondrites those of Ch/Cgh-types (Vernazza et al. (2016) and references therein). Asteroid densities appear systematically lower than those of their meteoritic analogs ($\rho_S = 3.05$ g cm^{-3} versus $\rho_{OC} = 3.33$ g cm^{-3}, $\rho_{Ch/Cgh} = 1.7$ g cm^{-3} versus $\rho_{CM} = 2.13$ g cm^{-3}; regarding meteorites, the bulk density is provided throughout the manuscript), implying the presence of some amount of macroporosity (∼8% for S-types and ∼20% for Ch-/Cgh-types) within these bodies. Furthermore, there is a small density trend within two major compositional classes (S and C types) where larger bodies (median diameters for large S and C-types: 204 km and 332 km respectively) possess higher densities on average with respect to smaller ones (median diameters for small S and C-types: 141 and 208 km respectively) ($\rho_{largeS} = 3.08$ g cm^{-3}, $\rho_{smallS} = 3.01$ g cm^{-3}, $\rho_{largeC} = 1.84$ g cm^{-3}, $\rho_{smallC} = 1.65$ g cm^{-3}). We note that the small variation in diameter within our Ch/Cgh sample in tandem with the large uncertainty of our mass estimates may explain why such a trend is not seen in that group. Overall, both a higher macroporosity value for Ch/Cgh-type bodies with respect to the more massive S-type bodies and the aforementioned
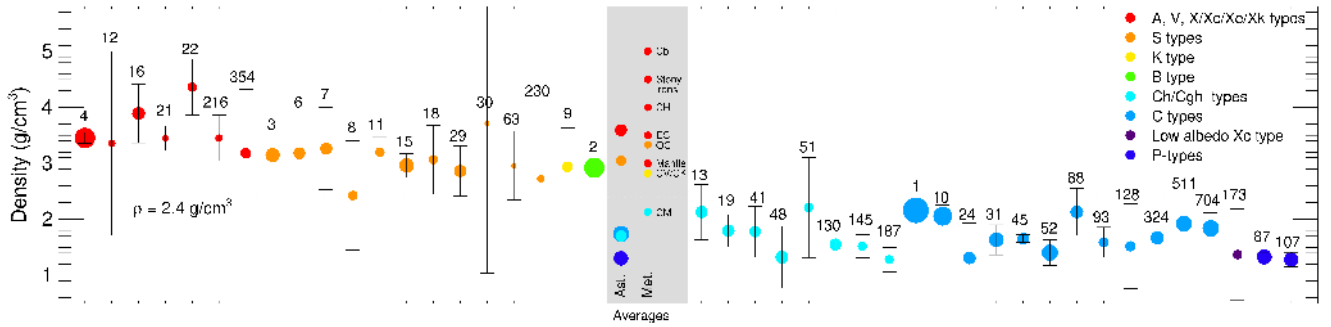
Fig. 7. Density distribution of our large programme asteroid targets. The density distribution appears strongly bimodal (see text) with volatile-poor bodies on the left of the gray zone and volatile-rich bodies on its right. Two multiple systems (93 Minerva and 107 Camilla; Marchis et al. 2013; Pajuelo et al. 2018) imaged outside of our observing program were also added because of their accurate density determination. Asteroids are grouped following their spectral classification. The relative sizes of the dots follow the relative diameters of the bodies in logarithmic scale. Error bars are one sigma. In the center of the figure, the gray zone shows the average density of the main asteroid groups (left) and of their likely meteoritic analogs (right).
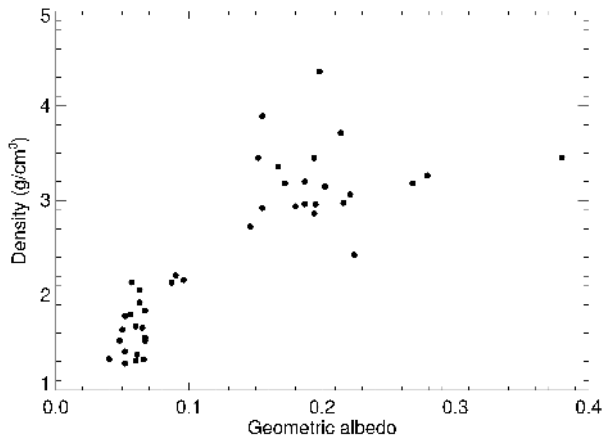
Fig. 8. Relationship between the geometric albedo of large asteroids and their density. We observe two groups of objects: those with high albedos (≥ 0.14) and densities (≥ 2.7 g cm^{-3}) and those with low albedos (≤ 0.1) and densities (≤ 2.2 g cm^{-3}).

density trend between larger and smaller S- and C-type bodies suggest that the amount of macroporosity decreases with increasing size, and therefore mass, in agreement with the findings of Carry (2012). Finally, it appears that macroporosity is minimal (≤ 5–10%) for objects with masses $\geq 10^{19}$ kg.

6. Surface topography

As expected, the main topographic features observed in the images are impact craters and basins. Thanks to the unprecedented resolution of SPHERE/ZIMPOL, craters with minimum diameters of $D \sim 25$–70 km (depending on the geocentric distance during the observations) could be detected from the ground for the first time. The most prominent ones are also captured in the reconstructed shape models (see Appendix B).

As outlined in Vernazza et al. (2020) in the cases of (10) Hygiea and (1) Ceres, there appears to be a crater dichotomy between volatile-poor and volatile-rich bodies which cannot solely be explained by the difference in heliocentric distance. As a matter of fact, volatile-rich bodies are located on average further away from the Sun than volatile-poor ones (typically a factor of 2 in geocentric distance and therefore surface resolution).

We interpret this dichotomy as a consequence of different crater morphologies on volatile-rich versus volatile-poor bodies. Whereas bowl-shaped craters are easily identifiable from the

ground, leading to a clear contrast between the crater floor and walls and the crater rim, the same is not true in the case of complex craters with a flat floor. Notably, impacts in volatile-poor surfaces form bowl-shaped craters up to much larger diameters than in the case of volatile-rich surfaces (e.g., Hiesinger et al. 2016). In the case of Ceres for example (Schenk et al. 2021), all craters with diameters above ~12 km are complex (flat floored) which explains why craters can hardly be recognized in our images although Ceres' surface is saturated in craters. In contrast, several craters with diameters in the 24–45 km range could be easily identified in our images of (4) Vesta (Fétick et al. 2019) using observations from the Dawn mission as benchmark (Marchi et al. 2012).

Finally, the case of (2) Pallas (Marsset et al. 2020) has taught us that the inclination of the orbit of a body is a key parameter driving its collisional history (the higher the inclination, the more violent the collisional history because of higher mean impact velocities). A dedicated paper presenting an in-depth analysis of all impact craters detected by our survey is in preparation.

7. Discussion

In this section, we attempt to provide partial answers to the questions listed in the introduction based on data from our large programme.

7.1. What is the diversity in shapes among large asteroids and are the shapes close to equilibrium?

Apart from (216) Kleopatra and its dumb-bell shape (Marchis et al. 2021), all our targets with $D > 100$ km possess shapes compatible with that of an ellipsoid and whose departure from a perfect ellipsoid strongly increases with decreasing size. Furthermore, the rotation period appears in most cases to be a determining factor in the resulting shape, with faster rotating bodies being more elongated than slower rotating objects. Along these lines, the rotation period is a key factor in the observed bimodality of the shapes (particularly true for objects with diameters above ~140 km), and separates increasingly spherical bodies from those that are more elongated. Except (216) Kleopatra, the shapes of all of the bodies are compatible with a Maclaurin equilibrium figure. We note that we cannot exclude that some bodies formed as Jacobi ellipsoids, as suggested in the case of (16) Psyche (Ferrais et al. 2020).

Table 2. Overview of the current knowledge regarding the surface and bulk composition of large asteroids ($D > 100$ km) belonging to the main taxonomic classes.

Asteroid type	Surface composition	Families	Bulk density	Differentiated (yes/no)
S	Ordinary chondrites	Homogeneous	Ordinary chondrites	No
Ch/Cgh	CM chondrites	Homogeneous	CM chondrites	No
C/Cb/Cg	Chondritic smooth IDPs ?	Heterogeneous ?	<CM chondrites	?
P	Chondritic porous IDPs	Heterogeneous	<CI/TL	Likely yes
M/X	ECs, CB/CH, unsampled material?	?	<CB, >CH, ≫EC	Likely yes (21, 22) 16, 216: TBD

However, only a handful of bodies are really close to the Maclaurin sequence ($\chi^2 = 0.0064$). These are all large ($D \geq 220$ km) volatile-rich ($\rho \leq 2.2$ g cm^{-3}) bodies. The "equilibrium" shapes of large volatile-rich bodies may suggest that the interiors of these bodies had a fluid-like behavior until recent times, a likely consequence of their high content of volatiles and of thermal heating due to the decay of long-lived radionuclides (e.g., Carry et al. 2021) leading to continuous relaxation. The evolutionary history of these bodies may therefore have followed that of Ceres for which a paucity of large impact basins has been observed (Marchi et al. 2016), suggesting that the interiors and/or outer shells of these bodies have behaved like fluids (i.e., significantly relaxed) over long timescales. The fact that large volatile-poor bodies such as (2) Pallas and (4) Vesta depart from equilibrium can be understood as a direct consequence of an absence of recent relaxation and that they may no longer be geologically active. In their cases, late major impacts have excavated a fraction of their volume without affecting the rest of the overall shape, leading them to depart from the equilibrium figure. For smaller volatile-poor bodies, this mechanism is in competition with re-accumulation following a large catastrophic impact (Vernazza et al. 2020; Yang et al. 2020b) which brings them closer to the Maclaurin equilibrium figure.

7.2. How do large impacts affect asteroid shape?

All objects in our survey ((8) Flora, (10) Hygiea, (31) Euphrosyne) that are members of a large collisional family that formed following a catastrophic disruption belong to the "spherical" group. Numerical simulations of such impact events (Vernazza et al. 2020; Yang et al. 2020b,a) imply that the parent bodies were entirely disrupted and that the largest remnants formed via re-accumulation and that their shapes should be rather spherical, exactly as observed. In the case of smaller yet major impacts (e.g., (2) Pallas, (3) Juno, (4) Vesta), the shape is modified by the formation of large impact basins.

In summary, extremely large impacts reset the shapes of large asteroids and cause the shape to become roughly spherical and close to that of an ellipsoid. Conversely, smaller impacts cause the shape to become less spherical and to increase its departure from that of an ellipsoid.

7.3. What is the bulk density of large asteroids and is there a relationship with their surface composition? Is there any evidence of differentiation among those bodies?

Characterizing the density of the largest asteroids has been one of the main science objectives of our large programme. Indeed, density is the physical property that best constrains the bulk composition of asteroids provided that their interiors contain a minimal fraction (<20%) of macroporosity. This is likely the case for the largest ($D \geq 100$ km) asteroids whereas the interiors of smaller bodies ($D \leq 100$ km) may be largely occupied by voids (reaching up to 50–60% in the case of the smallest bodies; e.g., Carry 2012; Scheeres et al. 2015).

Our programme has confirmed the presence of a low level of macroporosity (<20%) in the interior of the largest asteroids with the latter becoming almost negligible (≤5%) in the interiors of the most massive bodies (with $m \geq 10^{19}$ kg). However, this assumes that the bulk density of meteorites is representative of that of their parent bodies. Most importantly, our analysis reveals a strong dichotomy in density between volatile-poor ($\rho = 3.26$ g cm^{-3}) and volatile-rich ($\rho_S = 1.69$ g cm^{-3}) bodies.

Hereafter, we summarize the constraints delivered by our large programme regarding the bulk composition of the main taxonomic classes. Specifically, we combine our density measurements with previous spectroscopic observations of the surfaces of main-belt asteroids (including asteroid families) to constrain the formation and evolution of the main taxonomic classes (Table 2). We note that we do not discuss the case of our single V-type target Vesta here (see instead a review of the Dawn mission results by Russell et al. 2015) nor those of A- and K-type asteroids given the large uncertainties on their density estimates.

7.3.1. X, Xc, and Xe types

High-albedo ($\rho_v \geq 0.15$) X/Xc/Xe-complex asteroids (which is the case of our four targets: (16) Psyche, (21) Lutetia, (22) Kalliope, (216) Kleopatra) likely comprise the parent bodies of (1) iron meteorites (e.g., Cloutis et al. 1990; Shepard et al. 2015 and references therein), (2) enstatite chondrites (ECs), and aubrites (e.g., Vernazza et al. 2009, 2011; Ockert-Bell et al. 2010; Shepard et al. 2015), (3) CB and CH chondrites (e.g., Hardersen et al. 2011; Shepard et al. 2015; Krämer Ruggiu et al. 2021), and (4) anomalous metal-rich chondrites (e.g., Reddy et al. 2019). While stony-iron meteorites (mesosiderites, pallasites) could be plausible analogs for these asteroid types because of their similarity in density, their spectral properties appear to be at odds with those of these asteroid types (Ferrais et al., in prep.). We therefore consider it highly unlikely that these meteorites are analogs of these asteroid types. Pallasites are likely analogs of A-type asteroids (Cruikshank & Hartmann 1984; Sunshine et al. 2007), whereas mesosiderites may be analogs of V-type asteroids (e.g., Burbine et al. 2007, Ferrais et al., in prep.).

Besides Lutetia, which has been associated with enstatite chondrites (Vernazza et al. 2009, 2011), none of the remaining

asteroids possess a well-identified meteoritic analog in terms of surface composition (we note that the Lutetia-EC association cannot be considered as unquestionable). However, the densities derived by our survey are strong evidence at this stage that iron is neither the representative material of the surfaces of these asteroids, as implied by radar observations (Shepard et al. 2015, 2017, 2018) nor of their bulk composition. In addition, there is great variability in the metal content of the surfaces of these objects. Specifically, two of our X-complex targets possess a low radar albedo (Lutetia and Kalliope have a radar albedo in the 0.18–0.24 range; Shepard et al. 2015) whereas the remaining two targets possess a high radar albedo (Psyche and Kleopatra have a radar albedo in the 0.37–0.43 range; Shepard et al. 2017, 2018). Finally, three of these bodies show evidence of a ~0.9 micron and/or ~3 micron feature (Psyche, Kalliope and Kleopatra; Hardersen et al. 2011; Usui et al. 2019) whereas Lutetia is featureless in the visible and NIR range (e.g., Vernazza et al. 2011).

Our density estimates for our four X-complex targets are amongst the highest measured so far for main-belt asteroids, with both Kalliope and Psyche being the two densest bodies known so far after the telluric planets. If one considers that the amount of porosity of a high-density $D \sim 100$ km body (Lutetia, Kleopatra) should be in the 15–25% range whereas it should be below 10% for a $D \geq 150$ km body (Psyche, Kalliope), then the average density of the materials making up these bodies should be in the ~4.0–4.8 g cm^{-3} range. In the case of Lutetia, assuming an EC-like surface composition ($\rho_{EC} = 3.45$–3.80 g cm^{-3}; Macke et al. 2010), a denser interior may be implied, and therefore a thermal history including differentiation (Vernazza et al. 2011; Weiss & Elkins-Tanton 2013). A similar thermal history has also been proposed in the case of Kalliope (Ferrais et al., in prep.). For the remaining bodies, CH chondrites or a mixture of CH and CB chondrites (Ferrais et al., in prep.) may be plausible analogs, whereas CB chondrites alone seem excluded given their high density ($\rho_{CB} \sim 5$ g cm^{-3}; Macke et al. 2011). It might also be the case that no representative meteorites are available in our collections for these bodies. We therefore cannot presently exclude that both Kleopatra and Psyche are undifferentiated bodies.

Regarding the formation location of our four X-complex targets, the latter may be diverse. The connection between Lutetia and enstatite chondrites favors an origin in the terrestrial planet region (Vernazza et al. 2011). However, most large M-types, including (16) Psyche and (22) Kalliope, are located in the outer part of the asteroid belt (Gradie & Tedesco 1982; DeMeo & Carry 2013, 2014). Yet, the bodies scattered from the terrestrial planet region into the main belt are preferentially implanted in the inner and middle belt (Raymond & Izidoro 2017), likely precluding an inner Solar System origin for most large metal-rich bodies.

Finally, laboratory analyses of CB/CH chondrites and anomalous metal-rich chondrites should be a main focus in the near future for a more accurate understanding of the composition and overall thermal history of these bodies.

7.3.2. S-types

S-type asteroids comprise the parent bodies of the most common type of meteorites, namely ordinary chondrites (~80% of the falls), and also possibly those of some rare types of differentiated meteorites such as lodranites and acapulcoites (see Vernazza et al. 2015b for a detailed review on this topic). Vernazza et al. (2014) analyzed the visible and NIR spectral properties of nearly 100 S-type asteroids among which all our S-type targets are

found. These authors discovered that the surface composition of these bodies is compatible with that of H, L, and LL ordinary chondrites. Furthermore, they reported little compositional variation amongst the largest S-type collisional families, suggesting a rather homogeneous internal structure for the largest S-type asteroids.

Our derived densities for the largest S-type asteroids are consistent with those of ordinary chondrites and some level of macroporosity ($\leq 10\%$; see also Viikinkoski et al. 2015b; Marsset et al. 2017; Hanuš et al. 2019; Dudziński et al. 2020), implying – contrary to asteroid (4) Vesta – the absence of large-scale differentiation for these bodies, which is in agreement with both spectroscopic observations (Vernazza et al. 2014) and the thermal history of ordinary chondrites (Huss et al. 2006; Monnereau et al. 2013).

7.3.3. B-type (2) Pallas

The true nature and origin of (2) Pallas remains a mystery despite the breathtaking images acquired for that object within our large programme (Marsset et al. 2020). Its spectral properties in the visible and NIR, including its ~2.7 μm hydration feature (e.g., Takir & Emery 2012; Usui et al. 2019), are unlike those of any meteorite in our collection but suggest a connection to low albedo C-complex asteroids. In contrast, both its geometric albedo (0.155) and its density (2.92 g cm^{-3}) bring Pallas closer to rocky bodies (Marsset et al. 2020), in particular S-type asteroids.

A sample return mission to that object or to one of its family members currently appears to be a necessary future step for deciphering its formation and evolution unless a meteorite originating from Pallas is recovered in the coming years.

7.3.4. Ch/Cgh-types

Ch- and Cgh-type asteroids comprise the parent bodies of CM chondrites (Vilas & Gaffey 1989; Vernazza et al. 2016 and references therein). An analysis of the visible and NIR spectral properties of 70 of these bodies was reported by Vernazza et al. (2016), among which all our Ch/Cgh targets are found, as well as the members of some of the largest collisional families. These latter authors showed that the spectral variation observed among these bodies is mostly due to variations in the average regolith grain size. In addition, they showed that the spectral properties of the vast majority (unheated) of CM chondrites resemble those of both the surfaces of the largest bodies and those of the smaller family members, implying a homogeneous internal structure and a "low" temperature (<300°C) thermal evolution of the CM parent body(ies) (Vernazza et al. 2016).

Our derived densities for the largest CM-like bodies are consistent with those of CM chondrites and some level of macroporosity (15–20%), suggesting a homogeneous internal structure for these bodies (Carry et al. 2019), in agreement with spectroscopic observations and numerical simulations of the thermal history of CM chondrite parent bodies (Bland & Travis 2017; Neveu & Vernazza 2019).

7.3.5. C-types

The surfaces of C-type asteroids, including Ceres, appear unsampled by our meteorite collections, similar to P- and D-type asteroids (Vernazza et al. 2015a, 2017). Notably, these abundant asteroid types (DeMeo & Carry 2013) comprise – similarly to S-types – a high number of large asteroid families such as the Hygiea, Themis, Euphrosyne, Nemesis, and Polana-Eulalia

families (see Brož et al. 2013; Nesvorný et al. 2015 for further information on asteroid families). Considering that asteroid families are a major source of meteorites (this is well supported by the connection between the Vesta family and the HED meteorites), we should be receiving plenty of fragments from these bodies. Nevertheless, this seems not to be the case for their surface material, at least not under the form of consolidated meteorites. We note that metamorphosed CI/CM chondrites have been proposed in the past as analogs of C-, Cb-, and Cg-type surfaces (Hiroi et al. 1993). However, such a possibility presently appears untenable (Vernazza et al. 2015a).

Vernazza et al. (2015a) proposed that these asteroid types might (at least their surfaces and/or outer shells) consist largely of friable materials unlikely to survive atmospheric entry as macroscopic bodies. It may therefore not be surprising that these asteroid types are not well represented by the cohesive meteorites in our collections. Vernazza et al. (2015a) proposed that interplanetary dust particles (IDPs) as well as volatiles may, similarly to comets, be more appropriate analogs for these bodies (at least their surfaces and/or outer shells).

Given the lack of well-identified extra-terrestrial analogs for these bodies, it follows that most of our knowledge regarding the origin, formation, and evolution of these bodies is rather limited and so far comes from remote-sensing observations only. Spectroscopic observations of these bodies in the $3\mu m$ region (Takir & Emery 2012; Usui et al. 2019) have allowed their surface compositions and thermal histories to be refined. It appears that most of the large C-type asteroids are found to possess a ~2.7 μm feature associated with the presence of hydrated minerals at their surfaces (Usui et al. 2019). This implies that their present outer shell has witnessed aqueous alteration. Furthermore, visible and NIR spectroscopic observations of two major C-type collisional families (Themis and Euphrosyne; Marsset et al. 2016; Yang et al. 2020a) indicate some degree of spectral variation (from C to P/X) that may hint at a primordial heterogeneous internal structure of their parent bodies (Marsset et al. 2016).

Our derived average density for C-type asteroids (1.74 $g\,cm^{-3}$) is the same within uncertainties as that of CM-like C-types (1.70 $g\,cm^{-3}$). However, the average diameter of our C-type targets is 313 km, whereas this is 181 km for CM-like C-types, and the factor difference in average mass between the two C-type groups is ~5. It follows that the average macroporosity may be significantly reduced in the interiors of our C-type targets with respect to the 20% value inferred for our CM-like targets (see Sect. 5). Given that the average mass of our C-type targets is comparable to that of our S-type sample, we assume by direct analogy an average macroporosity of at most 10% for our C-type sample leading to a maximum density of the analog material of 1.97 $g\,cm^{-3}$. This implies an average bulk composition for large C types that likely consists of material that is less dense than CM chondrites ($\rho_{CM} = 2.13$ $g\,cm^{-3}$). Such material may contain (i) more microporosity due in some cases to more limited aqueous alteration of the interior, (ii) fewer chondrules by analogy with the less dense CI chondrites and/or the Tagish Lake meteorite (whose density amounts to ~1.6 $g\,cm^{-3}$), and/or (iii) more volatiles and/or water. In any case, thermally metamorphosed volatile-poor CI/CM chondrites appear as unlikely analogs for these bodies based on our density estimates.

Notably, there are some major differences in density among the largest C-types (with $D \geq 300$ km) with densities ranging between ~1.5 $g\,cm^{-3}$ (52 Europa) and 2.16 $g\,cm^{-3}$ (1 Ceres) and for which the macroporosity may be negligible. We speculate that the thermal histories of these bodies may be an important factor at the origin of these density differences and that the denser targets may have a more lithified (*cemented*) interior due to aqueous alteration. Indeed, all large C-types with higher densities (Ceres, Hygiea, Interamnia, Davida) possess a well-defined 2.7 μm band in their spectra (Usui et al. 2019) implying the presence of hydrated minerals at their surfaces, whereas such a band is nearly absent or significantly shallower in the spectrum of (52) Europa. This may imply that Europa may have a partially aqueously altered interior whereas the four other objects experienced significant aqueous alteration up to their current surface. Considering C/P-type objects with similar diameters and masses, both features (a lower density and a less hydrated surface) place (52) Europa in between P-type asteroid (87) Sylvia and C-complex asteroids Interamnia and Davida (see Sect. 7.4 for possible implications). Finally, Ceres' density is abnormally high (2.16 $g\,cm^{-3}$; Russell et al. 2016) compared to the average density of Hygiea, Interamnia, and Davida (1.94 $g\,cm^{-3}$) on the one hand, and that of Callisto, Ganymede, Pluto, and Charon (in the 1.71–1.93 $g\,cm^{-3}$ range) on the other hand. This suggests the possibility of loss of volatile material in the case of Ceres. The scenario in which Ceres once possessed an icy shell of ~30–50 km in thickness as a consequence of its early thermal evolution that was lost following its implantation in the asteroid belt (Castillo-Rogez et al. 2016) has some merit following our results. For instance, a 30 km icy shell would imply a primordial density of ~2.05 $g\,cm^{-3}$ for Ceres, still higher than that of the other large C-types.

7.3.6. P-types

P- and D-type asteroids represent the vast majority of the Jupiter Trojans and about 10% of all main-belt asteroids (DeMeo & Carry 2013, 2014). Their visible, NIR, and MIR spectral properties resemble those of comets (Emery et al. 2006; Vernazza et al. 2015a; Vernazza & Beck 2017) implying a similar surface composition (at least for the silicate component). So far, chondritic porous interplanetary dust particles appear to be the most likely representative samples of the surface material of these bodies (Vernazza et al. 2015a; Vernazza & Beck 2017). In particular, the volatile-rich Tagish Lake meteorite appears to be non-representative of the surface composition of most P- and D-type asteroids with well-characterised NIR and MIR spectral properties as suggested earlier (Hiroi et al. 2001). So far, only one P-type asteroid has been tentatively linked to that meteorite, namely 368 Haidea (Vernazza et al. 2013). Spectroscopic observations in the $3\mu m$ region have revealed that most P-type and all D-type asteroids possess an anhydrous surface composition (Takir & Emery 2012; Usui et al. 2019) which contrasts with the aqueously altered surfaces of C-complex asteroids. Notably, the spectral characterisation of the members of the Eurybates family, the largest collisional family among the Jupiter Trojans (P/D types), has revealed significant spectral variety (Fornasier et al. 2007; De Luise et al. 2010), with about half of the family members being C-types and the remaining objects being P-types. These observations could suggest that P-/D-type asteroids did differentiate and that their cores may consist of C-type-like material (Vernazza et al. 2017).

Our observations of triple P-type asteroid (87) Sylvia likely imply the presence of a core, and therefore a differentiated internal structure (Carry et al. 2021). Sylvia's low density and likely differentiated interior can be explained by partial melting and mass redistribution through water percolation. The outer shell would be composed of material similar to interplanetary dust particles (IDPs) and the core similar to aqueously altered IDPs or

carbonaceous chondrite meteorites. By analogy with the Eurybates family, the core may have spectral properties similar to those of C-type asteroids. In the case of (87) Sylvia, our density estimate for its $D \sim 200$ km large core amounts to ~ 1.7 g cm^{-3}, a value consistent with the density of C-type asteroids. Finally, a differentiated interior has also been advocated in the case of the second largest P-type asteroid (107) Camilla (Pajuelo et al. 2018).

7.4. Does the main asteroid belt comprise former trans-Neptunian objects and do we recognize all of them?

The Nice model, which invokes an outward migration of Uranus and Neptune (Tsiganis et al. 2005; Morbidelli et al. 2005; Levison et al. 2009), implies that the P/D- type main-belt asteroids (and thus P/D near-Earth asteroids) and the Trojans of Jupiter likely have the same origin as outer Solar System small bodies such as Centaurs, short-period comets, and small ($D \leq 300$ km) trans-Neptunian objects. Available spectroscopic observations of these populations as well as the similarity in size distributions between the Jupiter Trojans and trans-Neptunian objects (Fraser et al. 2014) support such a hypothesis.

Our density estimate of P-type (87) Sylvia (Carry et al. 2021) as well as that of (107) Camilla (Pajuelo et al. 2018) appear compatible with those of several $D \leq 300$ km TNOs (Brown 2013; Kovalenko et al. 2017) providing support for a direct link between P/D types and TNOs. However, the same applies for C-type asteroids. Based on our density estimates for all C-complex bodies, we cannot discard a link between these asteroid types and current TNOs. We note the existence of a few TNOs with extremely low densities (Brown 2013; Kovalenko et al. 2017) whose counterparts were not identified by our survey of main-belt asteroids.

Based on our density estimates and spectrophotometric observations, which we detail below, we speculate that many of the C-types could be former TNOs and that these C-types may simply represent the aqueously altered version of primordial P/D-type material. Here is a list of measurements that support such an idea:

- Large ($D \geq 130$ km) P-types likely partially differentiated (Pajuelo et al. 2018; Carry et al. 2021) and their interior (core) may not simply have a C-type-like density (typically 1.7 g cm^{-3}; Carry et al. 2021) but also C-type spectral properties as suggested by the spectroscopic observations of the Eurybates family (Fornasier et al. 2007; De Luise et al. 2010). We note that spectroscopic observations of two large C-type families in the outer belt (Themis, Euphrosyne) show a mix of C- and P-types bodies, and therefore a similar spectral heterogeneity as observed in the case of the Eurybates family (Marsset et al. 2016; Yang et al. 2020a).
- The compositional (spectral type) mass distribution throughout the asteroid belt shows a rather sharp transition from the C- to the P-types (DeMeo & Carry 2013, 2014 and Fig. 9). This transition occurs in the outer belt (~ 2.8–3.3 AU), which corresponds exactly to the heliocentric range where the sublimation of water ice starts (e.g., Schorghofer 2008). For bodies located beyond 3.3 AU from the Sun, water ice can persist within the top few meters of the surface over billions of years. At such distances, mostly P- and D-type asteroids (DeMeo & Carry 2013, 2014) with anhydrous surfaces are observed (Takir & Emery 2012; Usui et al. 2019). Large P- and D-type asteroids that were implanted inward of 3.3 AU would have lost their comet-like P/D type outer shell due
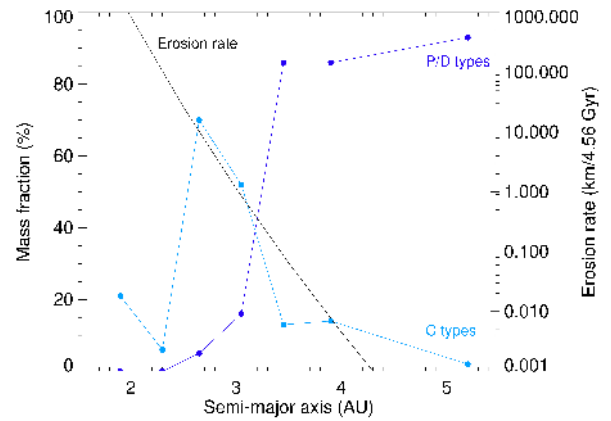
Fig. 9. Percentage of mass for C and P/D-type asteroids (DeMeo & Carry 2013) and the theoretical erosion rate due to the sublimation of water ice (Schorghofer 2008) as a function of the semi-major axis. For the calculation of the theoretical loss rate, we assumed a spherical shape, a geometric albedo of 0.05, zero obliquity, and an eccentricity of 0.145 (Morbidelli et al. 2015). The abrupt decrease in the fraction of P/D type asteroids (and conversely the abrupt increase in the fraction of C-types) occurs exactly where the erosion rate due to water sublimation becomes significant.

to water-ice sublimation (see Fig. 9 and Schorghofer 2008) in addition to collisional erosion, which would naturally explain why we are currently observing the exposed aqueously altered C-type-like interiors of these bodies. The same could apply for Ceres (see above) whose density appears higher (2.16 g cm^{-3}) than the typical density of large TNOs (1.8–2.0 g cm^{-3}; Kovalenko et al. 2017) and that may have lost a primordial ~ 30–50 km thick icy shell following its implantation in the middle belt (see above).
- The size distribution of TNOs does not reach its maximum at ~ 270 km which corresponds to the diameter of the largest inner Solar System P/D-type (namely 87 Sylvia). Instead, the current TNO population comprises a few hundred $D \geq 300$ km bodies (Lawler et al. 2018; Bannister et al. 2018). It is therefore difficult to imagine that no $D \geq 300$ km bodies were trapped in the asteroid belt following the outward migration of Uranus and Neptune as described in the Nice model. Considering C-complex bodies along with P/D-type asteroids as implanted TNOs would help to solve this issue. We note that in Vokrouhlický et al. (2016), the efficiency of TNO capture is too high in the main belt (by a factor of 10 in some parts). As a solution, they propose for example a weaker scaling law along with substantial collisional grinding, long-term dynamical removal by the Yarkovsky effect, or thermal destruction. Considering C-types along with P/D types (as proposed here) implies that the high capture efficiency may no longer be a problem.

In conclusion, we propose that some C-complex bodies (so-called IDP-like C-types) could be intrinsically related to IDP-like P- and D-type asteroids, representing different layers of a same body (C: core; P/D: outer shell). In this scenario, aqueously altered chondritic smooth IDPs appear as the most likely analogs of IDP-like C-types with anhydrous chondritic porous IDPs being the analogs of P/D-type asteroids. We thus highlight the possibility that P/D-types and some C-complex bodies may have the same origin in the primordial trans-Neptunian disk. We note that this suggestion is not incompatible with a different formation location for the remaining C-complex bodies (including
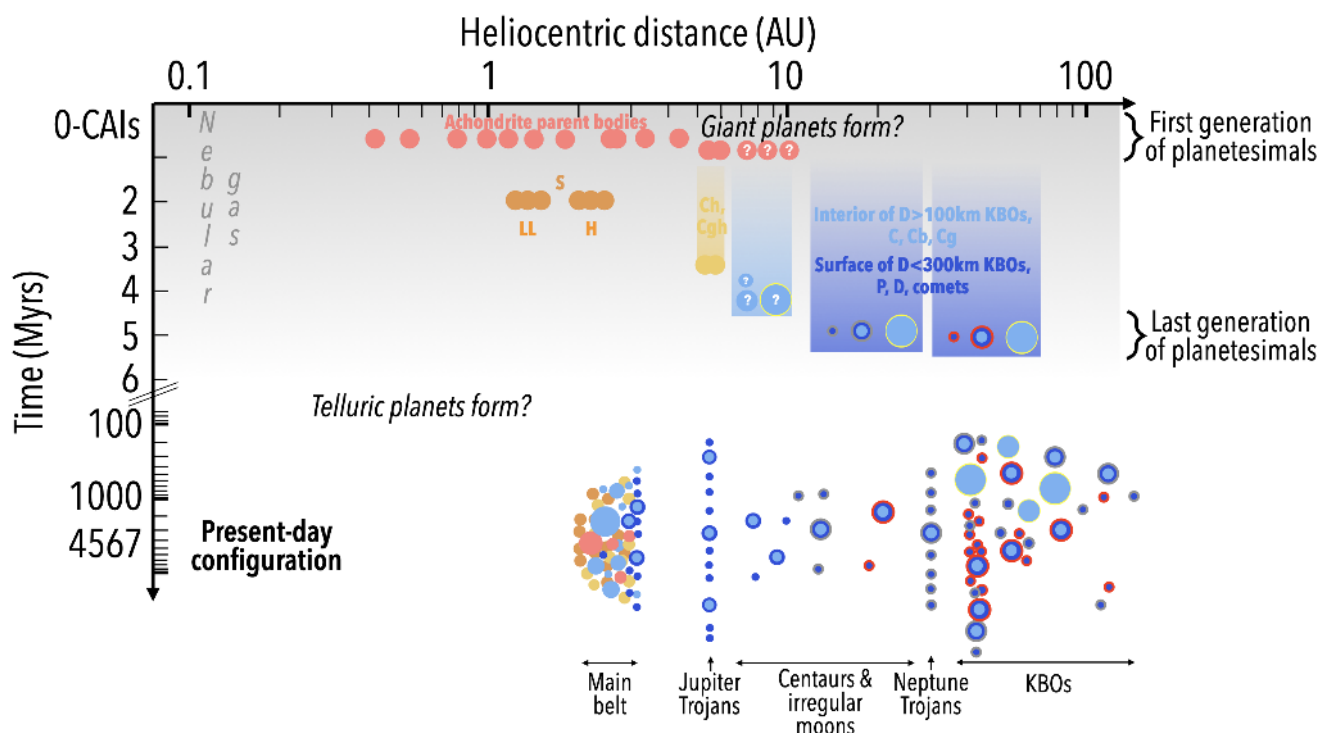
Fig. 10. Postulated sequence of events tracing the time, place, and duration of formation of the main compositional classes of small bodies (top) to present-day observed characteristics (bottom; vertical spread reproducing roughly the distribution of orbital inclinations). The accretion duration is shown as gradient boxes ending at the fully formed bodies. This graph is adapted from Vernazza & Beck (2017) and Neveu & Vernazza (2019) with the following novelty: we highlight the possibility that so-called IDP-like C-types could be intrinsically related to IDP-like P- and D-type asteroids, representing different layers of a same body (C: core; P/D: outer shell). Therefore, C, P, and D-types may all have the same origin in the primordial trans-Neptunian disk. Kuiper belt objects (KBOs) that were implanted inward of the snowline following giant planet migration may have lost their P/D outer shell due to water ice sublimation revealing their C-type interiors.

CM-like bodies; see Fig. 10) in regions between the giant planets (Raymond & Izidoro 2017). In particular, we speculate that chondrule-rich CM-like bodies, while sharing a similar density with other C-complex bodies, may have a different origin. As a matter of fact, chondritic porous IDPs (analogs of P/D types and comets) are chondrule-poor materials suggesting that CM-like bodies and P/D-types did not form in the same region of the Solar System.

7.5. What physical properties drive the formation of companions around large asteroids?

At the time of writing the Asteroid III book, seven multiple systems were known among the largest ($D \geq 90$ km) main-belt asteroids (Merline et al. 2002) and this number increased by a factor of two at the time of writing the Asteroid IV book (Margot et al. 2015). Since then, only one multiple system has been discovered among large main-belt asteroids ((31) Euphrosyne and its moon discovered via our observing programme; Yang et al. 2020b). Among these 15 multiple systems, six are triple systems, the first discovered being that of (87) Sylvia (Marchis et al. 2005). Two-thirds of these multiple systems belong to the C-complex while the remaining ones belong either to the P or M classes. Surprisingly, there are currently no large S-types with known companions. Whereas the observed S/CP type dichotomy may be interpreted as a consequence of compositional differences (hence different material strengths), implying a different response to impacts between the volatile-poor silicate-rich S-types and the volatile-rich CP-types, the existence of the dense metal- and silicate-rich Kalliope and Kleopatra systems renders this interpretation unlikely.

Instead of composition, the main physical properties that seem to favor the creation and/or long-term survival of moons appear to be rotation period and oblateness (Fig. 4). It appears that both of these physical quantities are lower than threshold values for most large asteroids with companions, namely $P \leq 6$ h and $c/a \leq 0.65$. This also applies to large binary systems not covered by our large programme. Among our large programme targets, (31) Euphrosyne appears to be an exception as one of these two physical quantities (c/a) appears much higher than the threshold value. Given the young age (~0.3 Gyr) of the Euphrosyne family (Yang et al. 2020b,a), and therefore of the moon, future studies should attempt to determine the long-term stability of the moon in order to reach a better overall understanding of moon formation and long-term survival.

As proposed in the extreme case of Kleopatra (Marchis et al. 2021), mass ejection at the edges of rapidly rotating elongated bodies, the gravity of which is significantly lower at such locations (up to ~50% in the case of Kleopatra) than that of a spherical body of equivalent mass, might be a plausible explanation for the formation of some companions. The case of Euphrosyne might be different and may result from the large collision at the origin of its re-accumulation and the formation of its large family.

8. Conclusions and perspective

Here, we report the analysis of a high-angular-resolution imaging survey of 42 large main-belt asteroids conducted with VLT/SPHERE/ZIMPOL as an ESO large programme (199.C-0074; PI: P. Vernazza). Our asteroid sample comprises 39 bodies

with $D \geq 100$ km and in particular most $D \geq 200$ km main-belt asteroids (20/23). Furthermore, it reflects well the compositional diversity present in the main belt as the sampled bodies belong to the following taxonomic classes: A, B, C, Ch/Cgh, E/M/X, K, P/T, S, V.

The SPHERE/ZIMPOL images were first used to reconstruct the 3D shape of all targets with both the ADAM and MPCD reconstruction methods. We subsequently performed a detailed shape analysis and constrained the density of each target using available mass estimates including our own mass estimates in the case of multiple systems. We summarize the main results below.

- Size (and therefore mass) and the rotation period are the two main physical properties determining the shape of large asteroids. First, both the asphericity and the departure from an ellipsoid are highly anti-correlated with the size, and therefore the mass, of our targets. Second, the distribution of the asphericity values as a function of diameter appears bimodal with a group of "spherical" bodies and a group of "elongated" bodies. A difference in rotation period appears to be the main origin of such bimodality with more elongated bodies possessing a shorter rotation period with respect to more spherical ones. In addition, there is a statistically significant correlation between the rotation period and the c/a axis ratio of our targets. Finally, re-accumulation following large impacts completes the picture leading to the formation of rather spherical bodies.

- A comparison of the specific angular momentum and the normalized angular velocity of our targets with the expected values for Maclaurin and Jacobi ellipsoids as well as dumb-bell shapes shows that all bodies but one (Kleopatra) fall along the Maclaurin sequence. The only body falling onto the dumb-bell sequence is 216 Kleopatra. Furthermore, it appears that large ($D \geq 220$ km) volatile-rich bodies (except 31 Euphrosyne which is an odd case) tend to be the closest to the Maclaurin sequence (in terms of chi-square). The equilibrium shapes of large volatile-rich bodies may suggest that the interiors and/or outer shells of these bodies behaved like fluids (i.e., significantly relaxed) until recent times, a likely consequence of their high content of volatile material and of thermal heating due to the decay of long lived radionuclides (e.g., Carry et al. 2021) leading to continuous relaxation. The evolutionary history of these bodies may therefore have followed that of Ceres for which a paucity of large impact basins has been observed, suggesting that large-scale relaxation has occurred for billions of years and may still be ongoing (Marchi et al. 2016).

- Five out of six multiple systems possess a rotation period of shorter than 6 h and a c/a axis ratio of less than 0.65. Hence, both the rotation period and the oblateness of a body appear to be key factors for the formation and/or long-term stability of companions. Mass ejection at the edges of rapidly rotating elongated bodies might be a plausible explanation for the formation of some multiple systems.

- Densities in our sample range from ~1.3 g cm^{-3} (P-type asteroids 87 Sylvia) to ~4.3 g cm^{-3} (M/X-type asteroids 22 Kalliope), highlighting the wide diversity in composition of the asteroid belt. Furthermore, the density distribution appears bimodal to first order with volatile-poor ($\rho \geq$ 2.7 g cm^{-3}) bodies and volatile-rich bodies ($\rho \leq 2.2$ g cm^{-3}). Given that asteroid albedos also follow a bimodal distribution (Masiero et al. 2011), two main groups of asteroids emerge, namely (a) asteroids with a geometric albedo of below 0.1 and a density below 2.2 g cm^{-3} and (b) asteroids with a geometric albedo of higher than 0.145 and a

density of greater than 2.7 g cm^{-3}. Finally, our density estimates imply, in agreement with the findings of Carry (2012), that the amount of macroporosity decreases with increasing size, and therefore mass, and that macroporosity is minimal ($\leq$5–10%) only in the case of the largest objects with masses $\geq 10^{19}$ kg.

- Regarding the thermal evolution of the main compositional classes, our conclusions are as follows. Most ordinary chondrite-like and CM chondrite-like asteroids likely did not differentiate. However, this is not the case for large P-type asteroids and at least a fraction of X/M-type asteroids. The cores of P-type asteroids may consist of C-type material. This is well supported by our density estimate of these cores as well as spectroscopic observations of the Eurybates family. We speculate that a large fraction of nonCM-like C-type asteroids (Ch/Cgh types) may be genetically linked to P- and D-type asteroids and thus share a similar origin in the trans-Neptunian region.

Although our large programme has allowed us to make significant progress in our understanding of the formation and evolution of the largest asteroids, it has generated new questions for which future investigations should provide an answer. For example, the first pertains to whether or not our collections contain meteoritic analogs of high-density asteroids such as Kalliope, Psyche, and Kleopatra. If so, are these analogs CH or CB chondrites? An in depth characterization of these meteorite classes (spectroscopy, density) would help to make progress in this respect. Also, we do not know which asteroids are the parent bodies of metallic meteorites. Our density estimates for the largest M-types exclude a direct link between these objects and those meteorites, implying that the parent bodies could be found among smaller M-types. Also, thanks to our large programme, the volumes of ~40 large asteroids are now constrained with high accuracy (2–10%). However, the same cannot be said for the mass estimates for about half of these bodies. Exploitation of the high-accuracy astrometry delivered by the ESA Gaia mission for these bodies will help in constraining their mass with an uncertainty in the 10%-30% range (Mouret et al. 2008).

Another unknown is the number of multiple systems comprised by large asteroids ($D \geq 100$ km). Our program focused on ~40 large asteroids but the main asteroid belt comprises ~230 such bodies. High-angular-resolution imaging observations of the remaining $D \geq 100$ km bodies should be of high priority in the near future to tackle this question.

Most large volatile-rich asteroids with $D \geq 220$ km have shapes close to equilibrium. The slight deviation of their shapes from that of perfect ellipsoids is likely a consequence of the high collisional rate in the asteroid belt. Whether or not TNOs of similar sizes possess perfect equilibrium shapes is also unknown.

In the present work, we reveal the possibility that a fraction of C-complex asteroids (typically C-, Cb types) could be directly connected to P/D-type asteroids and TNOs. Several investigations should be conducted to prove or disprove this suggestion. These include: (1) the spectroscopic characterization of chondritic, smooth IDPs and a better understanding of their relation to chondritic, porous IDPs; (2) the spectroscopic characterization in the NIR and MIR (including the 3 micron region) of TNOs at all sizes and that of asteroid collisional families that show a mix of C and P-types (e.g., Eurybates); (3) a comparison of the size frequency distribution of C, P, and D-type asteroids with that of TNOs expanding previous investigations that focused on P/D type asteroids only (e.g., Vokrouhlický et al. 2016); and finally (4) dynamical simulations that should test the ability of the Nice

model to implant a Ceres-like and a Hygiea-like body in the asteroid belt along with a few $D \sim 300$ km C-type asteroids.

Our imaging observations demonstrate in a striking manner how the gap between interplanetary missions and ground-based observations is getting narrower (Fétick et al. 2019; Vernazza et al. 2020). With the advent of extremely large telescopes (ELT, GMT, TMT), the science objectives of future interplanetary missions to main-belt asteroids will have to be carefully thought out so that these missions will complement – and not duplicate – the achievements of Earth-based telescopic observations. For instance, first-generation ELT adaptive-optics NIR imaging observations of main-belt asteroids will allow the resolution of bodies with diameters down to 35–80 km (depending on their main-belt location) and craters down to ~10–25 km in size implying that we shall be able to characterize the global geological history of a much larger sample of main-belt asteroids from the ground. This implies that geological and geomorphological studies (based on high-angular-resolution imaging data) are likely to become – during the coming decade – the prime science objectives conducted from Earth in the case of $D \geq 35$–80 km asteroids, dethroning studies related to the nature and origin of these bodies deduced from the analysis of their spectra. Interplanetary missions to main-belt asteroids performing cosmochemistry experiments and/or a sample return should be given preference at the forefront of in situ exploration as these would ideally complement the investigations conducted from Earth. In particular, IDP-like asteroids as well as the rare B, L, Xc/Xe/Xk, and O types should be preferred targets as little is known regarding these bodies because of the paucity or absence of samples for these objects in our collections.

References

Bannister, M. T., Gladman, B. J., Kavelaars, J. J., et al. 2018, ApJS, 236, 18
Bartczak, P., & Dudziński, G. 2018, MNRAS, 473, 5050
Beuzit, J. L., Vigan, A., Mouillet, D., et al. 2019, A&A, 631, A155
Bland, P. A., & Travis, B. J. 2017, Sci. Adv., 3, e1602514
Brown, M. E. 2013, ApJ, 778, L34
Brož, M., Morbidelli, A., Bottke, W. F., et al. 2013, A&A, 551, A117
Brož, M., Marchis, F., Jorda, L., et al. 2021, A&A, 653, A56
Burbine, T. H., Greenwood, R. C., Buchanan, P. C., Franchi, I. A., & Smith, C. L. 2007, Lunar Planet. Sci. Conf., 38 2119
Capanna, C., Gesquière, G., Jorda, L., Lamy, P., & Vibert, D. 2013, The Visual Computer, 29, 825
Carry, B. 2012, Planet. Space Sci., 73, 98
Carry, B., Dumas, C., Fulchignoni, M., et al. 2008, A&A, 478, 235
Carry, B., Dumas, C., Kaasalainen, M., et al. 2010, Icarus, 205, 460
Carry, B., Vachier, F., Berthier, J., et al. 2019, A&A, 623, A132
Carry, B., Vernazza, P., Vachier, F., et al. 2021, A&A, 650, A129
Castillo-Rogez, J. C., Bowling, T., Fu, R. R., et al. 2016, Lunar Planet. Sci. Conf., 47 3012
Cloutis, E. A., Gaffey, M. J., Smith, D. G. W., & Lambert, R. S. J. 1990, J. Geophys. Res., 95, 281
Conrad, A. R., Dumas, C., Merline, W. J., et al. 2007, Icarus, 191, 616
Cruikshank, D. P., & Hartmann, W. K. 1984, Science, 223, 281
De Luise, F., Dotto, E., Fornasier, S., et al. 2010, Icarus, 209, 586
DeMeo, F. E., & Carry, B. 2013, Icarus, 226, 723
DeMeo, F. E., & Carry, B. 2014, Nature, 505, 629
DeMeo, F., Binzel, R. P., Slivan, S. M., & Bus, S. J. 2009, Icarus, 202, 160
Descamps, P. 2015, Icarus, 245, 64
Dudziński, G., Podlewska-Gaca, E., Bartczak, P., et al. 2020, MNRAS, 499, 4545
Ďurech, J., Sidorin, V., & Kaasalainen, M. 2010, A&A, 513, A46
Emery, J. P., Cruikshank, D. P., & Van Cleve, J. 2006, Icarus, 182, 496
Ferrais, M., Vernazza, P., Jorda, L., et al. 2020, A&A, 638, L15
Fétick, R. J., Jorda, L., Vernazza, P., et al. 2019, A&A, 623, A6
Fornasier, S., Dotto, E., Hainaut, O., et al. 2007, Icarus, 190, 622
Fraser, W. C., Brown, M. E., Morbidelli, A., Parker, A., & Batygin, K. 2014, ApJ, 782, 100
Fusco, T., Mugnier, L. M., Conan, J.-M., et al. 2003, Proc. SPIE, 4839, 1065
Gradie, J., & Tedesco, E. 1982, Science, 216, 1405
Grice, J., Snodgrass, C., Green, S. F., Parley, N. R., & Carry, B. 2017, in Asteroids, Comets, and Meteors (USA: IAU)
Hanuš, J., Viikinkoski, M., Marchis, F., et al. 2017, A&A, 601, A114
Hanuš, J., Marsset, M., Vernazza, P., et al. 2019, A&A, 624, A121
Hanuš, J., Vernazza, P., Viikinkoski, M., et al. 2020, A&A, 633, A65
Hardersen, P. S., Cloutis, E. A., Reddy, V., Mothé-Diniz, T., & Emery, J. P. 2011, Meteorit. Planet. Sci., 46, 1910
Hartigan, J. A., & Hartigan, P. M. 1985, Ann. Stat., 13, 70
Hiesinger, H., Marchi, S., Schmedemann, N., et al. 2016, Science, 353, aaf4758
Hiroi, T., Pieters, C. M., Zolensky, M. E., & Lipschutz, M. E. 1993, Science, 261, 1016
Hiroi, T., Zolensky, M. E., & Pieters, C. M. 2001, Science, 293, 2234
Huss, G. R., Rubin, A. E., & Grossman, J. N. 2006, Thermal Metamorphism in Chondrites, eds. D. S. Lauretta, & H. Y. McSween (Tucson: University of Arizona Press), 567
Jehin, E., Gillon, M., Queloz, D., et al. 2011, The Messenger, 145, 2
Jorda, L., Spjuth, S., Keller, H. U., Lamy, P., & Llebaria, A. 2010, SPIE Conf. Ser., 7533, 753311
Jorda, L., Gaskell, R., Capanna, C., et al. 2016, Icarus, 277, 257
Kovalenko, I. D., Doressoundiram, A., Lellouch, E., et al. 2017, A&A, 608, A19
Krämer Ruggiu, L., Beck, P., Gattacceca, J., & Eschrig, J. 2021, Icarus, 362, 114393
Lawler, S. M., Shankman, C., Kavelaars, J. J., et al. 2018, AJ, 155, 197
Levison, H. F., Bottke, W. F., Gounelle, M., et al. 2009, Nature, 460, 364
Macke, R. J., Consolmagno, G. J., Britt, D. T., & Hutson, M. L. 2010, Meteorit. Planet. Sci., 45, 1513
Macke, R. J., Consolmagno, G. J., & Britt, D. T. 2011, Meteorit. Planet. Sci., 46, 1842
Marchi, S., Ermakov, A. I., Raymond, C. A., et al. 2016, Nat. Commun., 7, 12257
Marchi, S., McSween, H. Y., O'Brien, D. P., et al. 2012, Science, 336, 690
Marchis, F., Descamps, P., Hestroffer, D., & Berthier, J. 2005, Nature, 436, 822
Marchis, F., Vachier, F., Ďurech, J., et al. 2013, Icarus, 224, 178
Marchis, F., Jorda, L., Vernazza, P., et al. 2021, A&A, 653, A57
Margot, J.-L., Pravec, P., Taylor, P., Carry, B., & Jacobson, S. 2015, Asteroids IV, Asteroid Systems: Binaries, Triples, and Pairs, eds. P. Michel, F. E. DeMeo, & W. F. Bottke (Tucson: University of Arizona Press), 355
Marsset, M., Vernazza, P., Birlan, M., et al. 2016, A&A, 586, A15
Marsset, M., Carry, B., Dumas, C., et al. 2017, A&A, 604, A64
Marsset, M., Brož, M., Vernazza, P., et al. 2020, Nat. Astron., 4, 569
Masiero, J. R., Mainzer, A. K., Grav, T., et al. 2011, ApJ, 741, 68
Merline, W. J., Weidenschilling, S. J., Durda, D. D., et al. 2002, Asteroids III, Asteroids Do Have Satellites, eds. W. F. Bottke, Jr., A. Cellino, P. Paolicchi, & R. P. Binzel (Tucson: University of Arizona Press), 289
Merline, W. J., Drummond, J. D., Carry, B., et al. 2013, Icarus, 225, 794
Monnereau, M., Toplis, M. J., Baratoux, D., & Guignard, J. 2013, Geochim. Cosmochim. Acta, 119, 302
Morbidelli, A., Levison, H. F., Tsiganis, K., & Gomes, R. 2005, Nature, 435, 462
Morbidelli, A., Walsh, K. J., O'Brien, D. P., Minton, D. A., & Bottke, W. F. 2015, Asteroid IV, The Dynamical Evolution of the Asteroid Belt (Tucson: University of Arizona Press), 493
Mouret, S., Hestroffer, D., & Mignard, F. 2008, Planet. Space Sci., 56, 1819
Mugnier, L. M., Fusco, T., & Conan, J.-M. 2004, JOSA A, 21, 1841
Nesvorný, D., Brož, M., & Carruba, V. 2015, Identification and Dynamical Properties of Asteroid Families, eds. P. Michel, F. E. DeMeo, & W. F. Bottke (Tucson: niversity of Arizona Press), 297
Neveu, M., & Vernazza, P. 2019, ApJ, 875, 30
Ockert-Bell, M. E., Clark, B. E., Shepard, M. K., et al. 2010, Icarus, 210, 674
Pajuelo, M., Carry, B., Vachier, F., et al. 2018, Icarus, 309, 134
Raymond, S. N., & Izidoro, A. 2017, Sci. Adv., 3, e1701138
Reddy, V., Pearson, N., Agee, C. B., et al. 2019, Lunar Planet. Sci. Conf., 50, 2212
Russell, C. T., Raymond, C. A., Coradini, A., et al. 2012, Science, 336, 684
Russell, C. T., McSween, H. Y., Jaumann, R., & Raymond, C. A. 2015, The Dawn Mission to Vesta and Ceres (Berlin: Springer), 419
Russell, C. T., Raymond, C. A., Ammannito, E., et al. 2016, Science, 353, 1008

Scheeres, D. J., Britt, D., Carry, B., & Holsapple, K. A. 2015, Asteroids IV (Tucson: University of Arizona Press)

Schenk, P., Castillo-Rogez, J., Otto, K. A., et al. 2021, Icarus, 359, 114343

Schmidt, B. E., Thomas, P. C., Bauer, J. M., et al. 2009, Science, 326, 275

Schorghofer, N. 2008, ApJ, 682, 697

Shepard, M. K., Taylor, P. A., Nolan, M. C., et al. 2015, Icarus, 245, 38

Shepard, M. K., Richardson, J., Taylor, P. A., et al. 2017, Icarus, 281, 388

Shepard, M. K., Timerson, B., Scheeres, D. J., et al. 2018, Icarus, 311, 197

Sierks, H., Lamy, P., Barbieri, C., et al. 2011, Science, 334, 487

Sunshine, J. M., Bus, S. J., Corrigan, C. M., McCoy, T. J., & Burbine, T. H. 2007, Meteorit. Planet. Sci., 42, 155

Takir, D., & Emery, J. P. 2012, Icarus, 219, 641

Thomas, P. C., Binzel, R. P., Gaffey, M. J., et al. 1997, Science, 277, 1492

Thomas, P. C., Parker, J. W., McFadden, L. A., et al. 2005, Nature, 437, 224

Tsiganis, K., Gomes, R., Morbidelli, A., & Levison, H. F. 2005, Nature, 435, 459

Usui, F., Hasegawa, S., Ootsubo, T., & Onaka, T. 2019, PASJ, 71, 1

Vernazza, P., & Beck, P. 2017, Planetesimals: Early Differentiation and Consequences for Planets (Cambridge: Cambridge University Press), 269

Vernazza, P., Brunetto, R., Binzel, R. P., et al. 2009, Icarus, 202, 477

Vernazza, P., Lamy, P., Groussin, O., et al. 2011, Icarus, 216, 650

Vernazza, P., Fulvio, D., Brunetto, R., et al. 2013, Icarus, 225, 517

Vernazza, P., Zanda, B., Binzel, R. P., et al. 2014, ApJ, 791, 120

Vernazza, P., Marsset, M., Beck, P., et al. 2015a, ApJ, 806, 204

Vernazza, P., Zanda, B., Nakamura, T., Scott, E. R. D., & Russell, S. 2015b, The Formation and Evolution of Ordinary Chondrite Parent Bodies (Tucson: University of Arizona Press), 617

Vernazza, P., Marsset, M., Beck, P., et al. 2016, AJ, 152, 54

Vernazza, P., Castillo-Rogez, J., Beck, P., et al. 2017, AJ, 153, 72

Vernazza, P., Brož, M., Drouard, A., et al. 2018, A&A, 618, A154

Vernazza, P., Jorda, L., Ševeček, P., et al. 2020, Nat. Astron., 4, 136

Viikinkoski, M., Kaasalainen, M., & Ďurech, J. 2015a, A&A, 576, A8

Viikinkoski, M., Kaasalainen, M., Ďurech, J., et al. 2015b, A&A, 581, L3

Viikinkoski, M., Vernazza, P., Hanuš, J., et al. 2018, A&A, 619, L3

Vilas, F., & Gaffey, M. J. 1989, Science, 246, 790

Vokrouhlický, D., Bottke, W. F., & Nesvorný, D. 2016, AJ, 152, 39

Wadell, H. 1935, J. Geol., 43, 250

Weiss, B. P., & Elkins-Tanton, L. T. 2013, Ann. Rev. Earth Planet. Sci., 41, 529

Yang, B., Hanuš, J., Brož, M., et al. 2020a, A&A, 643, A38

Yang, B., Hanuš, J., Carry, B., et al. 2020b, A&A, 641, A80

[1] Aix Marseille Université, CNRS, CNES, Laboratoire d'Astrophysique de Marseille, Marseille, France
e-mail: pierre.vernazza@lam.fr

[2] Institute of Astronomy, Charles University, Prague, V Holešovičkách 2, 18000 Prague 8, Czech Republic

[3] Université Côte d'Azur, Observatoire de la Côte d'Azur, CNRS, Laboratoire Lagrange, France

[4] Department of Earth, Atmospheric and Planetary Sciences, MIT, 77 Massachusetts Avenue, Cambridge, MA 02139, USA

[5] Mathematics and Statistics, Tampere University, 33720 Tampere, Finland

[6] SETI Institute, Carl Sagan Center, 189 Bernado Avenue, Mountain View CA 94043, USA

[7] IMCCE, CNRS, Observatoire de Paris, PSL Université, Sorbonne Université, Paris, France

[8] Astronomical Institute of the Romanian Academy, 5-Cuţitul de Argint, 040557 Bucharest, Romania

[9] Astronomical Observatory Institute, Faculty of Physics, Adam Mickiewicz University, Słoneczna 36, 60-286 Poznań, Poland

[10] NASA Goddard Space Flight Center, University of Maryland College Park, USA

[11] Space sciences, Technologies and Astrophysics Research Institute, Université de Liège, Allée du 6 Août 17, 4000 Liège, Belgium

[12] Institut de Planetologie et d'Astrophysique de Grenoble, UGA-CNRS, France; Institut Universitaire de France, Paris, France

[13] Jet Propulsion Laboratory, California Institute of Technology, 4800 Oak Grove Drive, Pasadena, CA 91109, USA

[14] European Space Agency, ESTEC - Scientific Support Office, Keplerlaan 1, Noordwijk 2200 AG, The Netherlands

[15] TMT Observatory, 100 W. Walnut Street, Suite 300, Pasadena, CA 91124, USA

[16] Open University, School of Physical Sciences, The Open University, MK7 6AA, UK

[17] Laboratoire Atmosphères, Milieux et Observations Spatiales, CNRS & Université de Versailles Saint-Quentin-en-Yvelines, Guyancourt, France

[18] Departamento de Fisica, Ingeniería de Sistemas y Teoría de la Señal, Universidad de Alicante, Alicante, Spain

[19] Institut de Ciències del Cosmos (ICCUB), Universitat de Barcelona (IEEC-UB), Martí Franquès 1, E08028 Barcelona, Spain

[20] European Southern Observatory (ESO), Alonso de Cordova 3107, 1900 Casilla Vitacura, Santiago, Chile

[21] Observatoire des Hauts Patys, 84410 Bédoin, France

[22] Observatoire de Chinon, Mairie de Chinon, 37500 Chinon, France

[23] Aix Marseille Université, CNRS, OHP (Observatoire de Haute Provence), Institut Pythéas (UMS 3470), 04870 Saint-Michel-l'Observatoire, France

[24] Geneva Observatory, 1290 Sauverny, Switzerland

[25] High Energy Physics and Astrophysics Laboratory, Cadi Ayyad University, Marrakech, Morocco

[26] B74, Avinguda de Catalunya 34, 25354 Santa Maria de Montmagastrell (Tarrega), Spain

[27] I39, Cruz del Sur Observatory, San Justo city, Buenos Aires, Argentina

[28] Observatoire du Bois de Bardon, 16110 Taponnat, France

[29] Association T60, Observatoire Midi-Pyrénées, 14 avenue Edouard Belin, 31400 Toulouse, France

[30] Hong Kong Space Museum, Tsimshatsui, Hong Kong, PR China

[31] I64, SL6 1XE Maidenhead, UK

[32] Korea Astronomy and Space Science Institute, 776, Daedeokdae-ro, Yuseong-gu, Daejeon 34055, Korea

[33] Chungbuk National University, 1, Chungdae-ro, Seowon-gu, Cheongju-si, Chungcheongbuk-do 28644, Korea

[34] Faculty of Physics, Astronomical Observatory Institute, Adam Mickiewicz University, ul. Słoneczna 36, 60-286 Poznań, Poland

[35] Observatoire OPERA, 33820 Saint Palais, France

[36] Uranoscope, Avenue Carnot 7, 77220 Gretz-Armainvilliers, France

[37] Institut d'Astrophysique de Paris, 98 bis boulevard Arago, UMR 7095 CNRS et Sorbonne Universités, 75014 Paris, France

[38] Anunaki Observatory, Calle de los Llanos, 28410 Manzanares el Real, Spain

[39] Club d'Astronomie de Lyon Ampere (CALA), Place de la Nation, 69120 Vaulx-en-Velin, France

[40] Kingsgrove, NSW, Australia

[41] Planetary Science Institute, 1700 East Fort Lowell Road, Tucson, AZ 85719, USA

[42] Rio Cofio Observatory, Robledo de Chavela (Madrid), Spain

[43] Cicha 43, 44-144 Nieborowice, Poland

Appendix A: Additional table

Table A.1: Absolute magnitude *H*, Sidereal rotation period *P*, spin-axis ecliptic J2000 coordinates λ and β, obliquity, asphericity, ellipsoid deviation, and dimensions along the major axis of the best-fit triaxial ellipsoids ($a > b > c$). Uncertainties correspond to 1 σ values.

N	H	P	λ	β	Obl	Asph	Ell. dev.	a	b	c
		[h]	[deg]	[deg]	[deg]			[km]	[km]	[km]
*1	3.34	$9.07417\pm1\times10^{-6}$	348.832±0.007	81.553±0.002	2	0.0012	0.0039	964.4±0.2	964.2±0.2	891.8±0.2
2	4.09	$7.81321\pm2\times10^{-5}$	42±3	-15±3	78	0.0151	0.0286	568±12	530±12	450±12
3	5.31	$7.209531\pm1\times10^{-6}$	105±3	18±3	60	0.0340	0.0526	288±5	250±5	225±5
*4	3.29	$5.34212767\pm1\times10^{-8}$	330.82±0.01	57.72±0.01	27	0.0139	0.0213	572.6±0.2	557.2±0.2	446.4±0.2
6	5.71	$7.274467\pm1\times10^{-6}$	342±2	50±1	36	0.0481	0.0679	220±9	205±8	166±7
7	5.51	$7.138843\pm1\times10^{-6}$	20±3	23±3	72	0.0645	0.0495	260±5	225±4	150±18
8	6.54	$12.86667\pm1\times10^{-5}$	337±2	-1±3	87	0.0198	0.0361	154±7	148±6	127±4
9	6.31	$5.079176\pm1\times10^{-6}$	181±2	22±2	73	0.0604	0.0624	218±10	176±10	133±8
10	5.43	$13.82559\pm5\times10^{-5}$	306±3	-29±3	120	0.0030	0.0134	450±10	430±10	424±20
11	6.55	$13.72204\pm1\times10^{-5}$	312±2	17±4	73	0.0301	0.0465	156±6	152±6	138±6
12	7.24	$8.660345\pm5\times10^{-6}$	177±2	-27±3	110	0.0625	0.0802	140±4	116±3	96±3
13	6.74	$7.046664\pm3\times10^{-6}$	38±5	31±5	59	0.0590	0.0869	238±12	199±11	182±10
15	5.28	$6.082753\pm1\times10^{-6}$	355±2	-70±2	169	0.0324	0.0434	340±14	248±13	229±14
16	5.90	$4.195948\pm1\times10^{-6}$	35±2	-9±2	96	0.0452	0.0402	277±5	238±6	164±4
18	6.51	$11.570306\pm5\times10^{-6}$	12±2	19±2	64	0.0319	0.0518	161±8	135±8	131±7
19	7.13	$7.443224\pm1\times10^{-6}$	103±3	60±3	29	0.0251	0.0428	242±10	203±10	192±10
*21	7.35	$8.168271\pm1\times10^{-6}$	52±1	-8±1	97	0.0682	0.0659	125±4	98±3	81±2
22	6.45	$4.1482\pm1\times10^{-6}$	195±3	4±3	97	0.0700	0.0717	207±5	145±4	122±4
24	7.08	$8.374187\pm1\times10^{-6}$	146±3	73±3	18	0.0238	0.0359	232±14	220±14	176±14
29	5.85	$5.390119\pm1\times10^{-6}$	323±2	-29±2	116	0.0205	0.0401	222±6	209±6	183±5
30	7.57	$13.68717\pm5\times10^{-6}$	106±2	19±2	72	0.0913	0.1101	112±5	84±5	76±4
31	6.74	$5.529595\pm1\times10^{-6}$	94±5	67±3	48	0.0112	0.0292	286±16	274±14	247±15
41	7.12	$5.98798\pm6\times10^{-5}$	199±5	-32±5	126	0.0546	0.0696	235±17	183±16	153±14
45	7.46	$5.699151\pm1\times10^{-6}$	128±2	-35±2	123	0.0596	0.0381	252±9	191±9	138±7
48	6.90	$11.890105\pm1\times10^{-6}$	294±2	51±2	45	0.0339	0.0443	257±3	211±3	185±3
51	7.35	$7.78484\pm1\times10^{-6}$	170±4	-66±4	153	0.0319	0.0559	167±6	158±5	128±4
52	6.31	$5.629954\pm1\times10^{-6}$	255±2	40±2	56	0.0314	0.0352	378±14	336±14	255±12
63	7.55	$9.297587\pm1\times10^{-6}$	121±2	-27±2	120	0.1172	0.0819	152±4	77±4	69±3
87	6.94	$5.18364\pm4\times10^{-5}$	75±5	64±5	28	0.0613	0.0464	363±5	249±5	191±5
88	7.04	$6.041321\pm1\times10^{-6}$	350±3	116±3	21	0.0168	0.0306	241±13	221±12	195±12
89	6.60	$11.388336\pm1\times10^{-6}$	14±2	-24±2	128	0.0525	0.0675	165±4	142±5	115±4
128	7.49	$38.9325\pm1\times10^{-4}$	313±2	-19±1	104	0.0253	0.0456	178±5	163±5	147±5
130	7.05	$5.224663\pm1\times10^{-6}$	68±180	-89±1	156	0.0525	0.0441	268±8	195±9	153±9
145	8.13	$15.07081\pm1\times10^{-5}$	101±4	48±3	48	0.0311	0.0608	153±3	142±3	141±3
173	7.80	$6.110939\pm1\times10^{-6}$	28±2	-17±2	95	0.0397	0.0553	162±8	152±8	123±8
187	7.98	$10.667033\pm2\times10^{-6}$	115±2	-79±2	179	0.0439	0.0623	151±9	122±8	130±8
216	7.30	$5.3852824\pm1\times10^{-7}$	74±0	22±0	61	0.2622	0.1305	267±6	61±6	48±6
230	7.35	$23.98475\pm1\times10^{-5}$	111±2	66±2	18	0.0374	0.0558	136±9	120±7	103±7
324	6.82	$29.4403\pm5\times10^{-5}$	17±4	-57±5	154	0.0101	0.0304	234±9	224±9	225±7
354	6.44	$4.277185\pm1\times10^{-6}$	154±2	24±2	71	0.0345	0.0561	191±14	162±12	144±12
511	6.22	$5.129365\pm1\times10^{-6}$	300±2	26±2	62	0.0269	0.0305	359±18	293±20	253±17
704	5.94	$8.71234\pm1\times10^{-5}$	87±5	62±5	36	0.0109	0.0233	354±9	343±8	303±7

Notes. * Values for Ceres, Vesta and Lutetia are derived using shape models from the NASA Dawn and ESA Rosetta space missions.

Appendix B: Individual mosaics

Comparison between VLT/SPHERE/ZIMPOL deconvolved images of our targets (top row) and the corresponding synthetic images generated by OASIS of our MPCD (second row) and ADAM (third row) shape models. The red arrows indicate the direction of the spin axis. Fourth and fifth rows: residuals in units of instrumental noise between the observed images and the synthetic images of the MPCD and ADAM shape models, respectively.
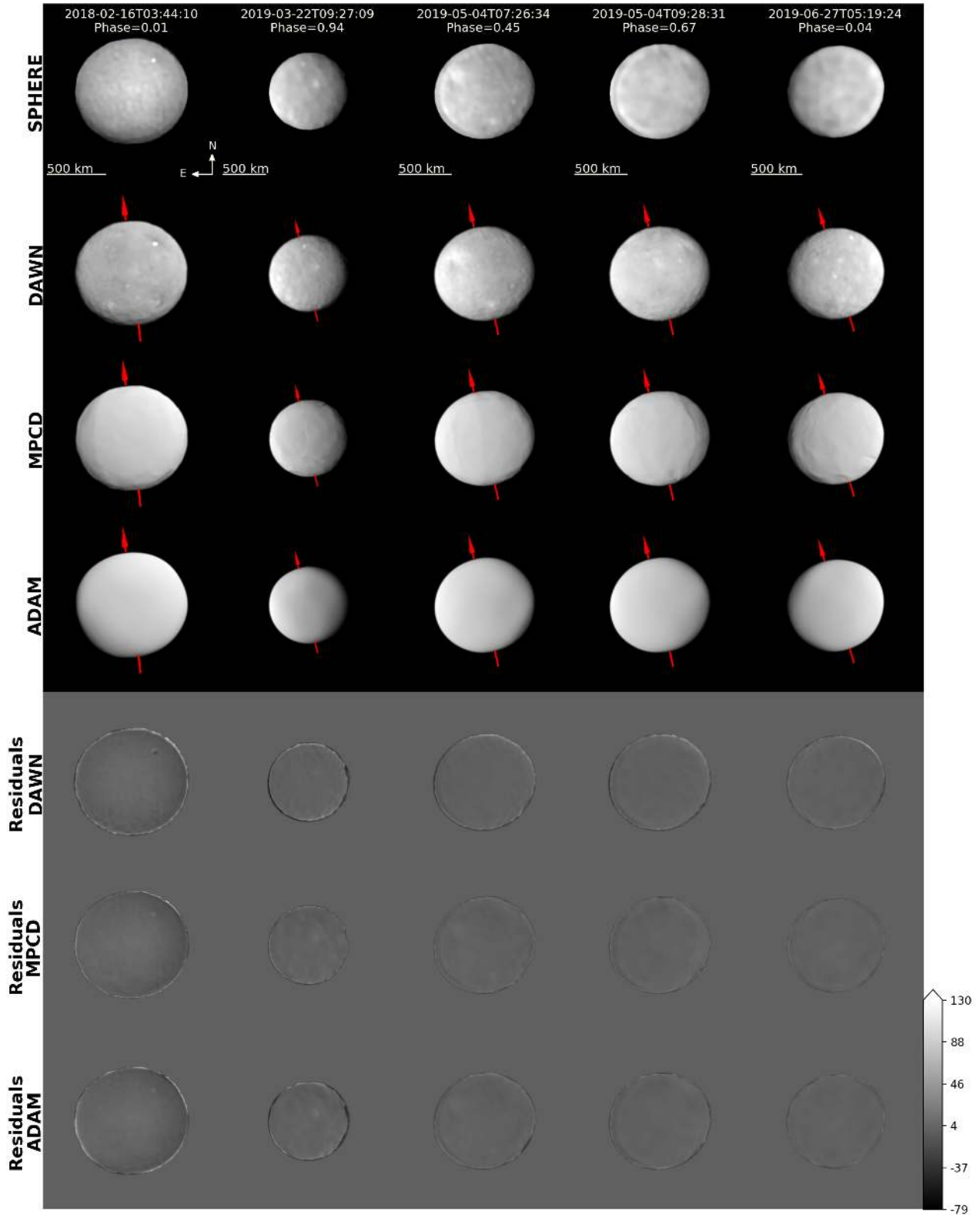
Fig. B.1: (1) Ceres.
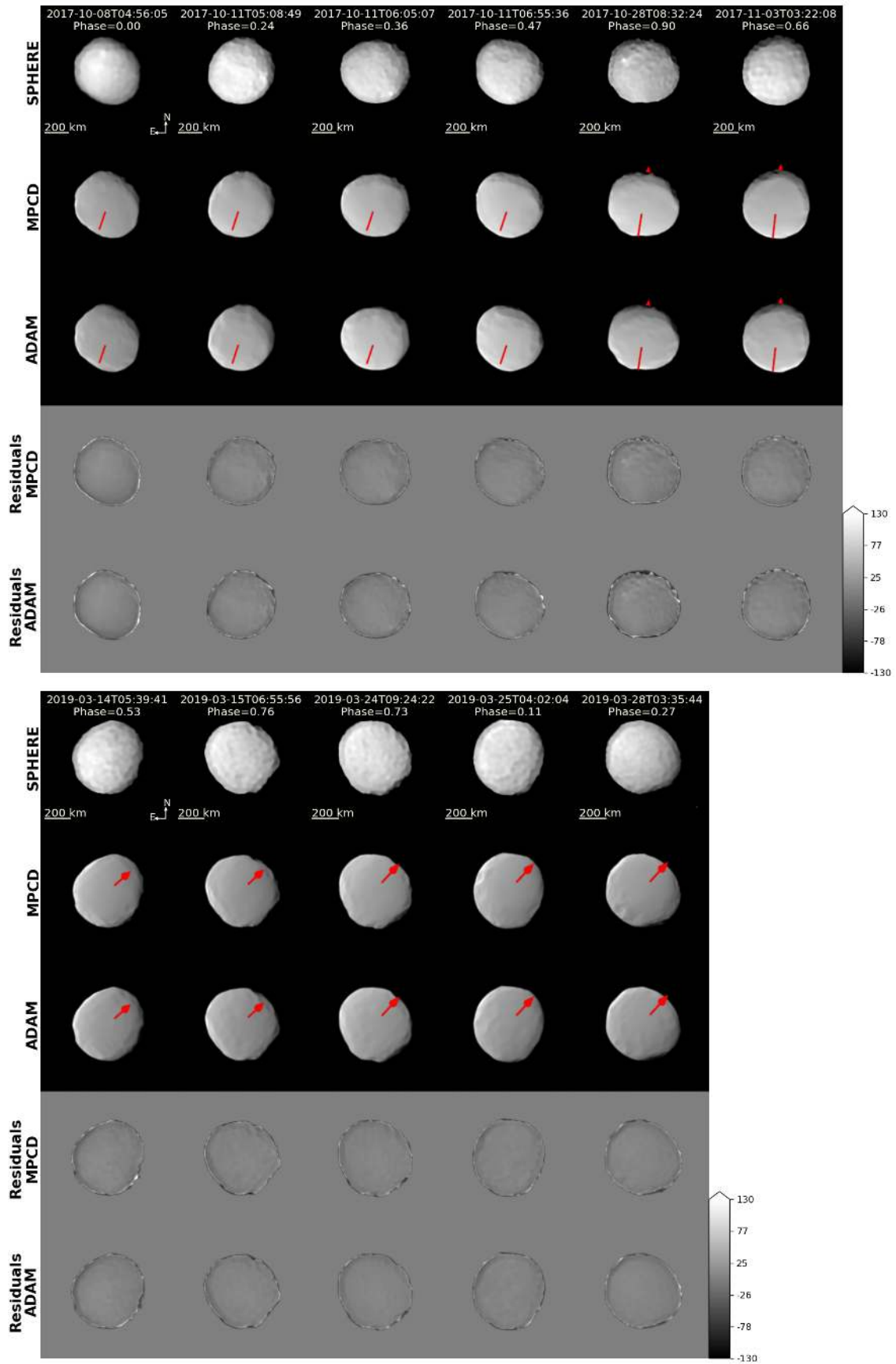
Fig. B.2: (2) Pallas.
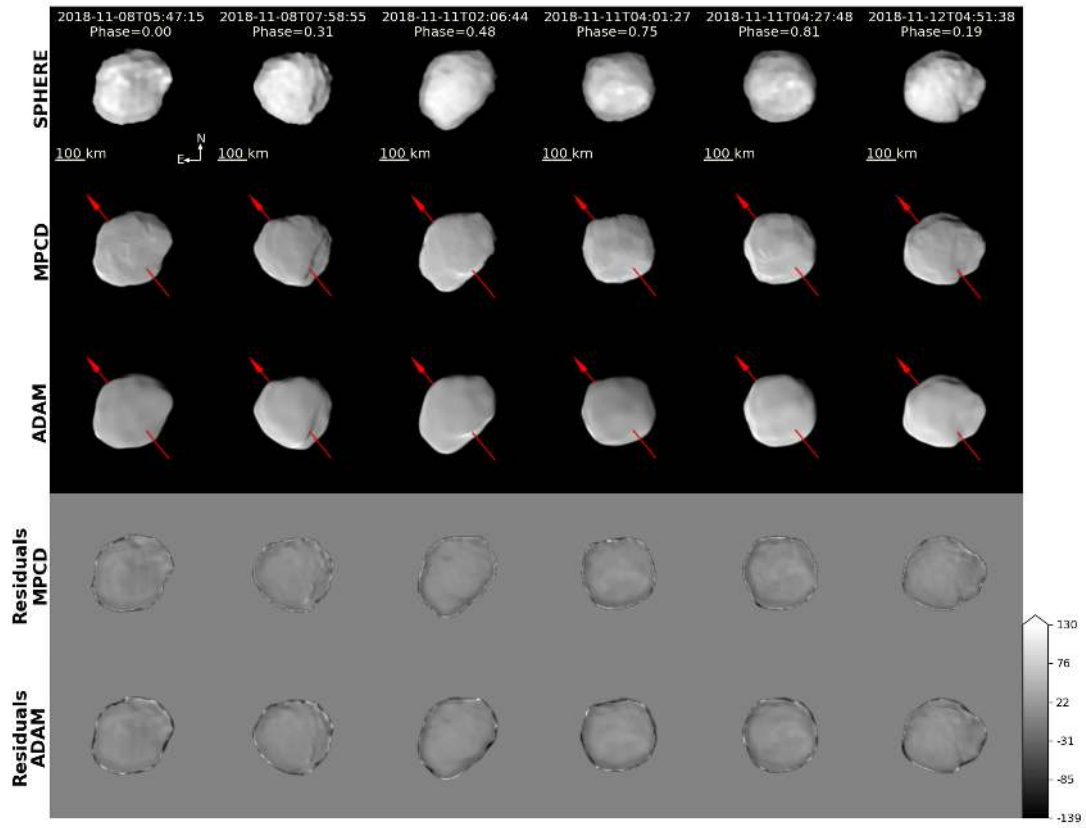
Fig. B.3: (3) Juno.
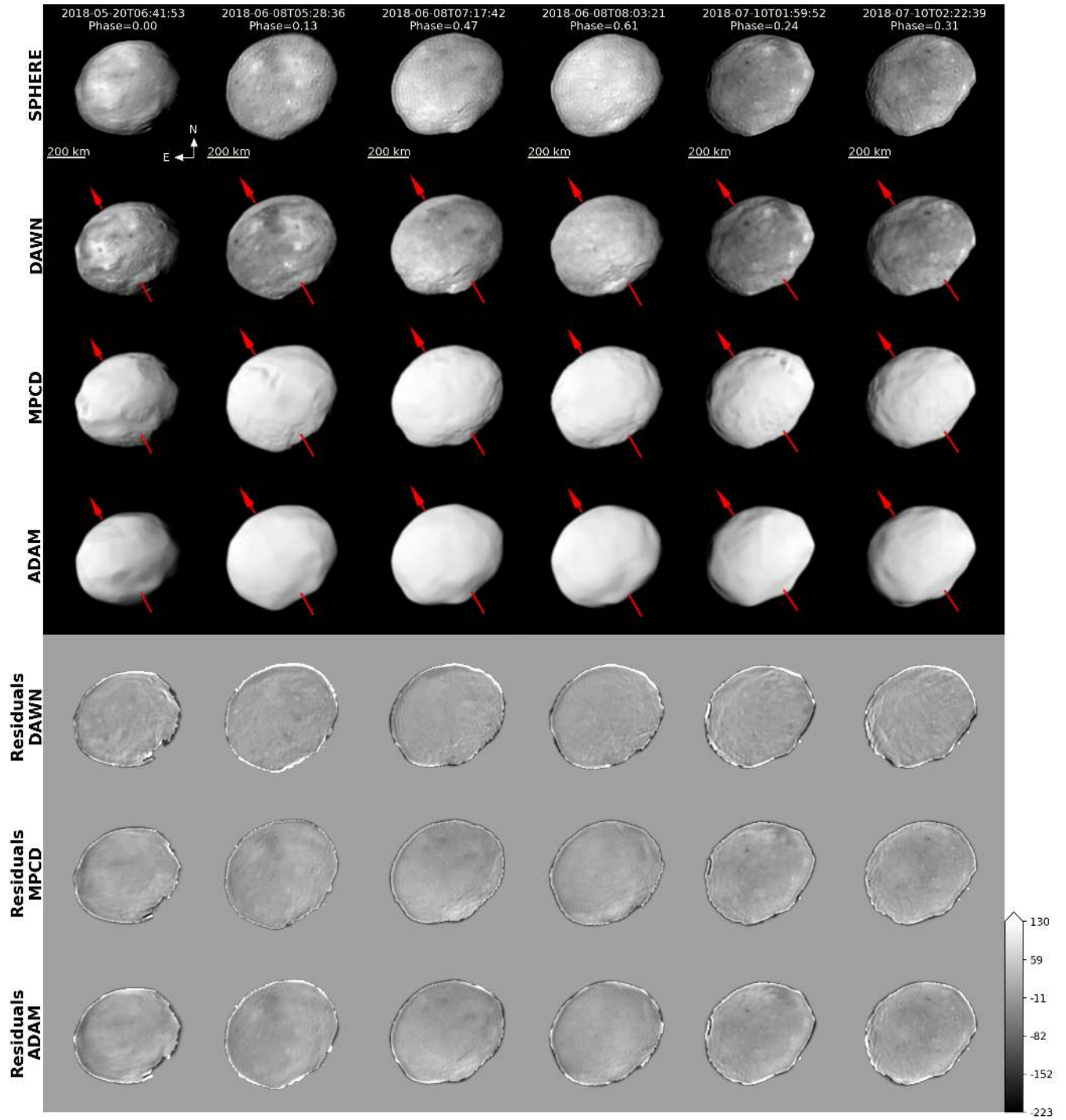
Fig. B.4: (4) Vesta.
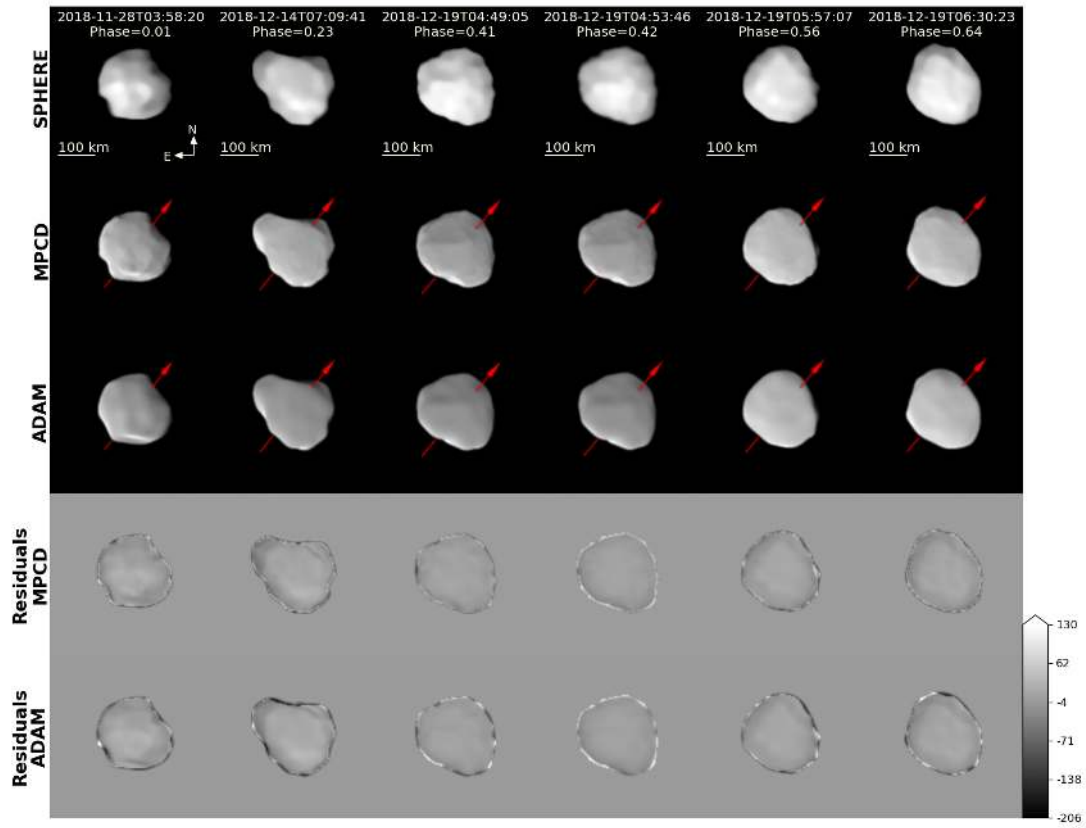
Fig. B.5: (6) Hebe.
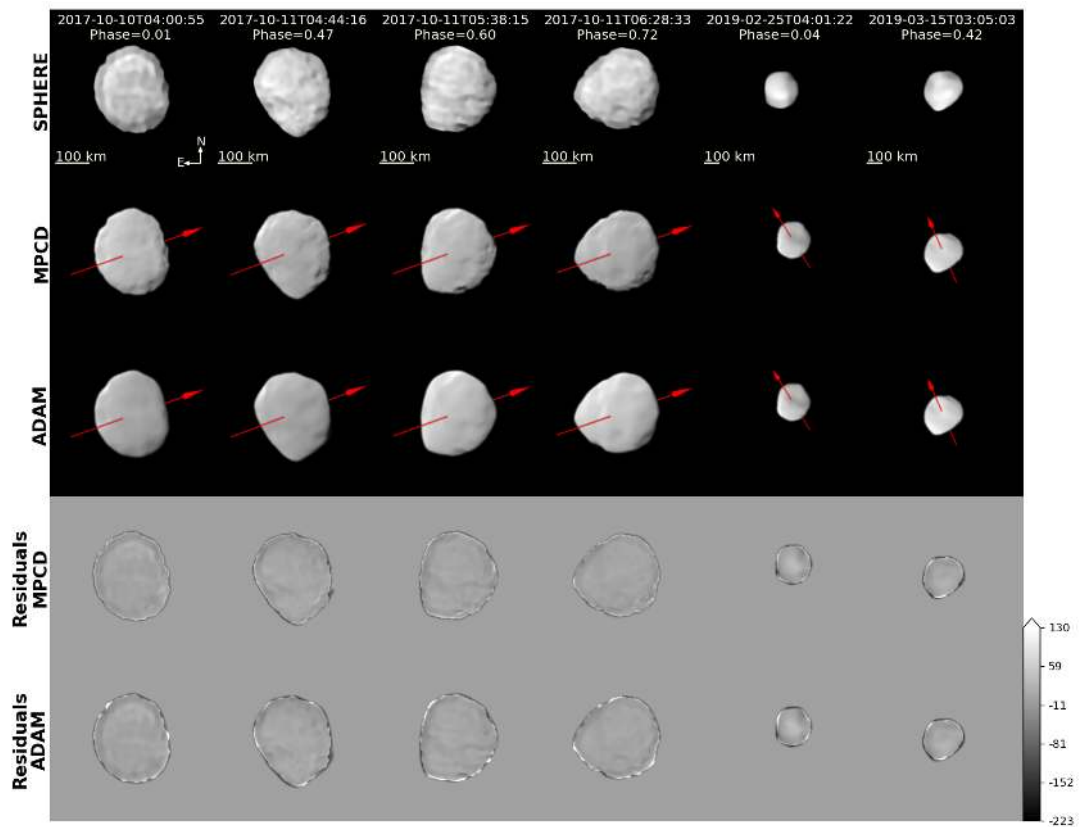
Fig. B.6: (7) Iris.
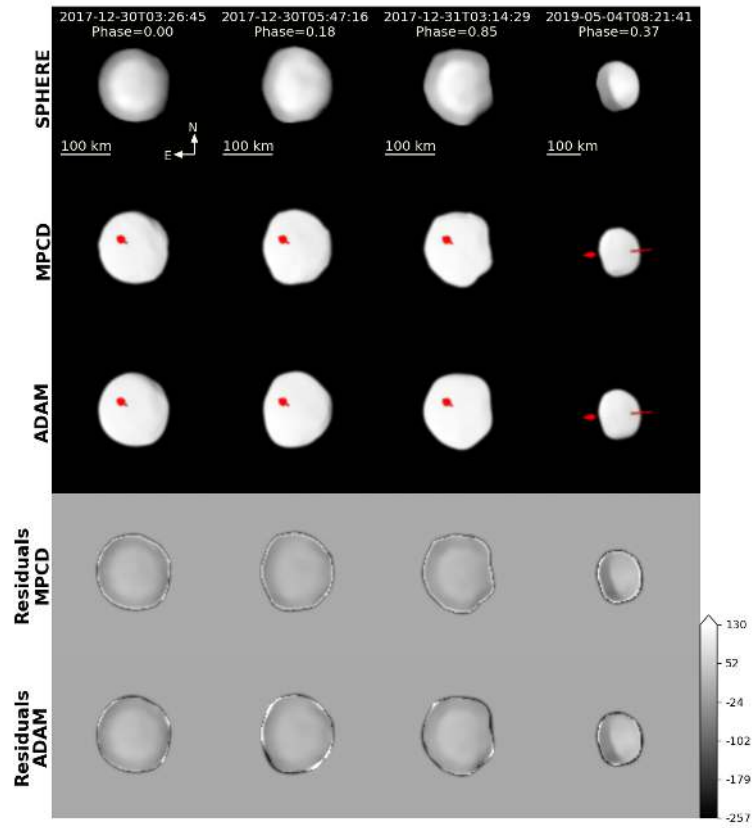
Fig. B.7: (8) Flora.
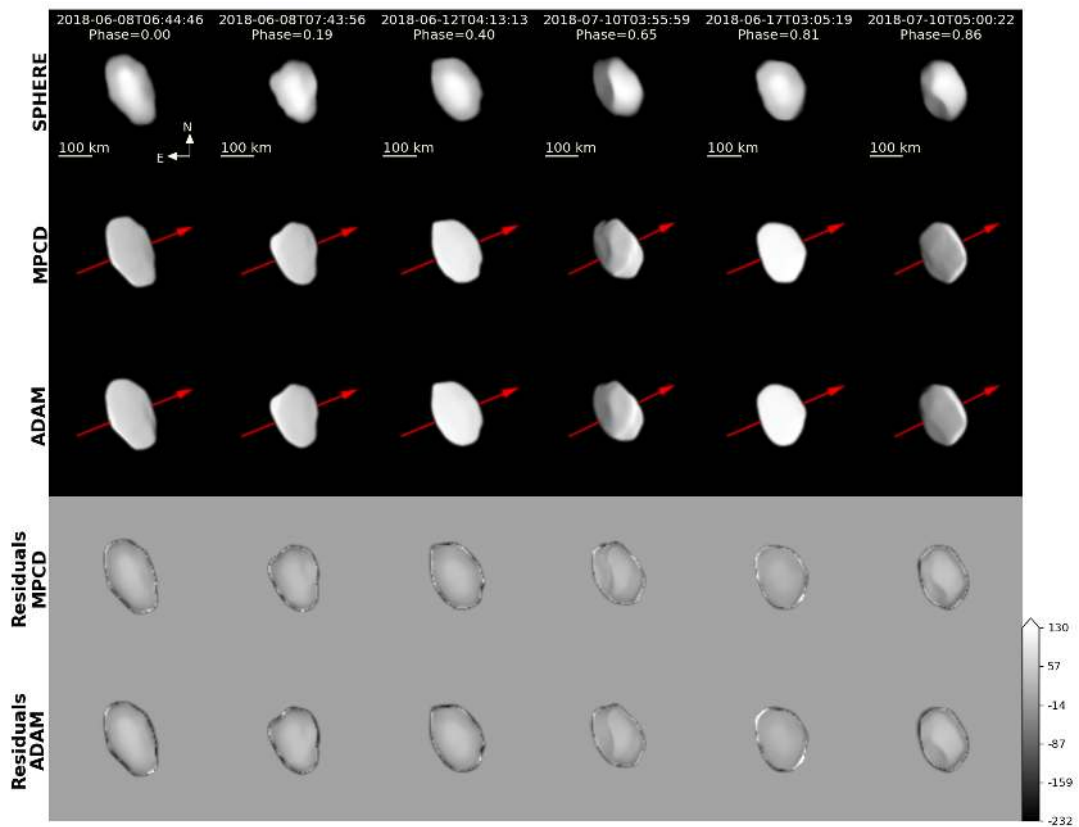
Fig. B.8: (9) Metis.
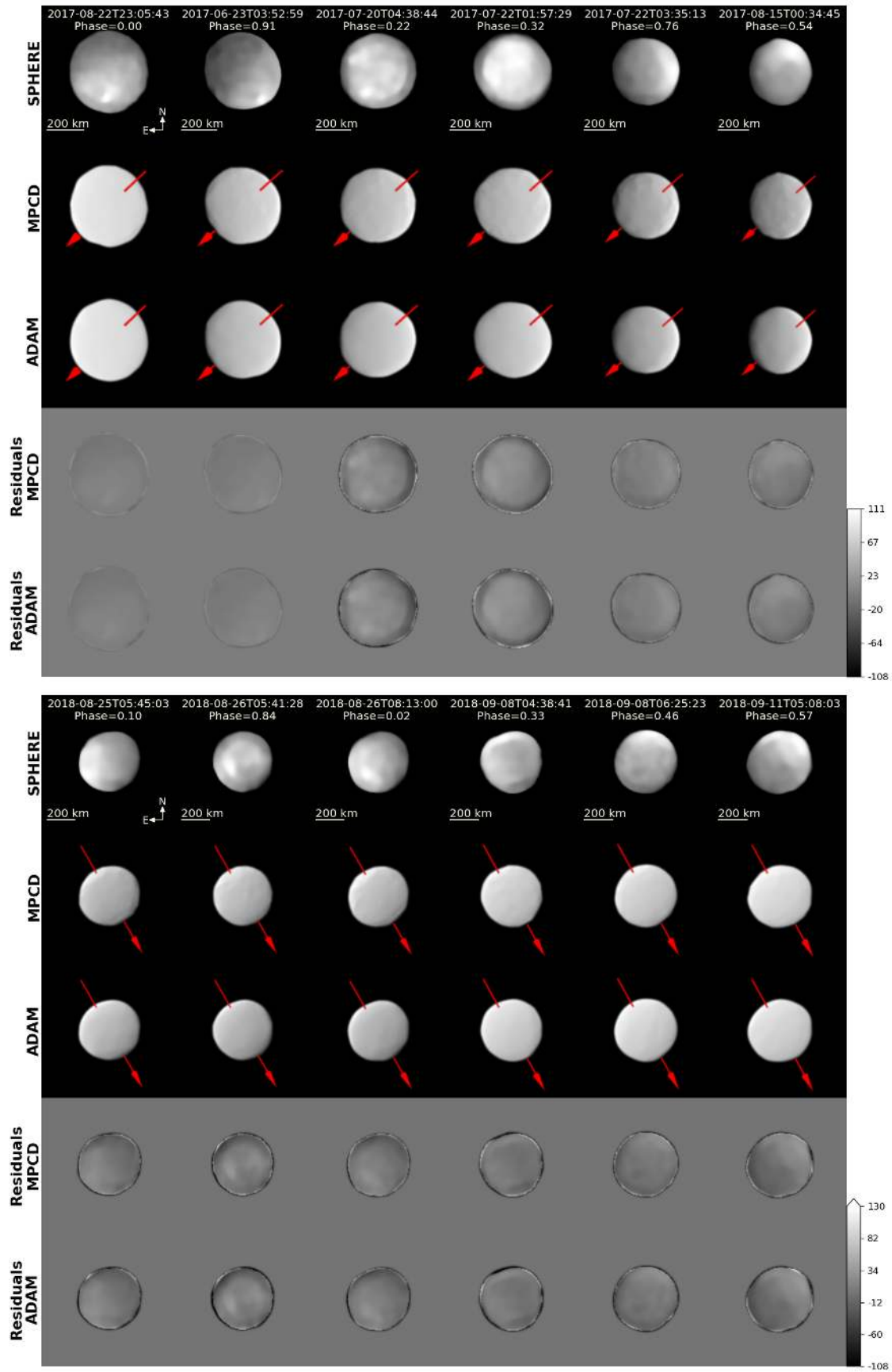
Fig. B.9: (10) Hygiea.
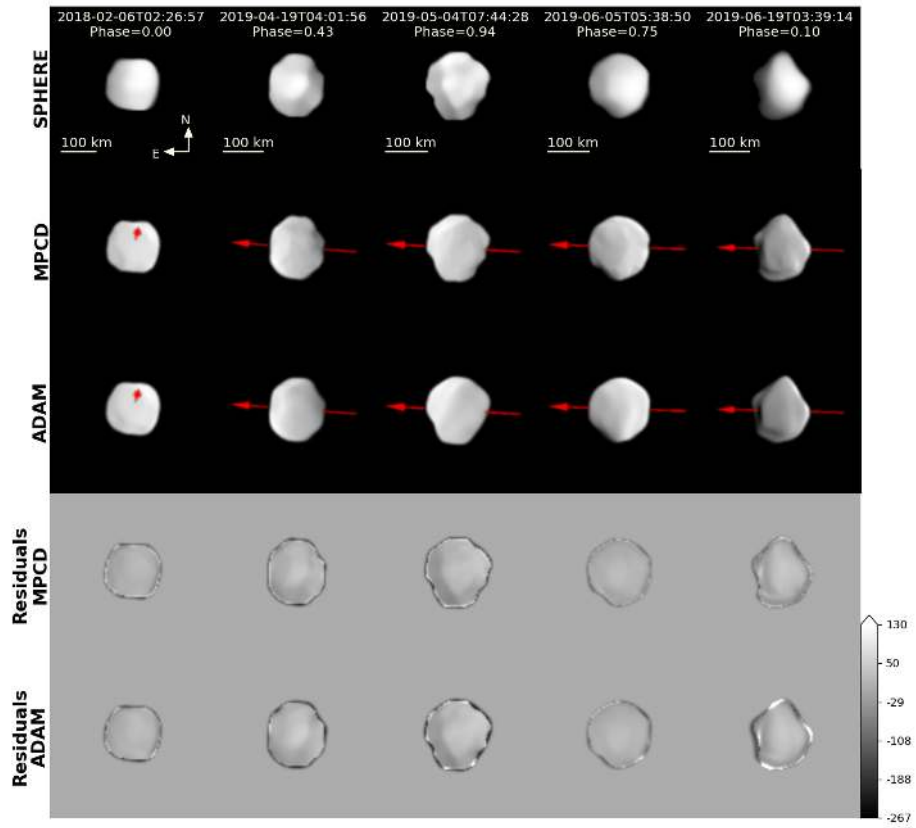
Fig. B.10: (11) Parthenope.
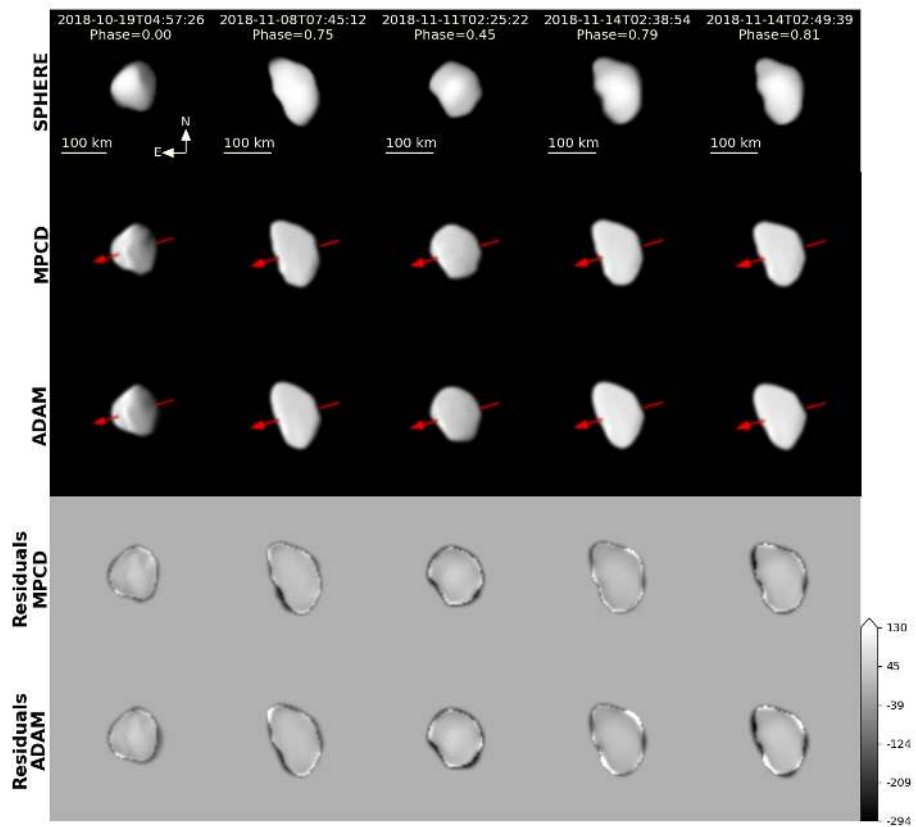
Fig. B.11: (12) Victoria.
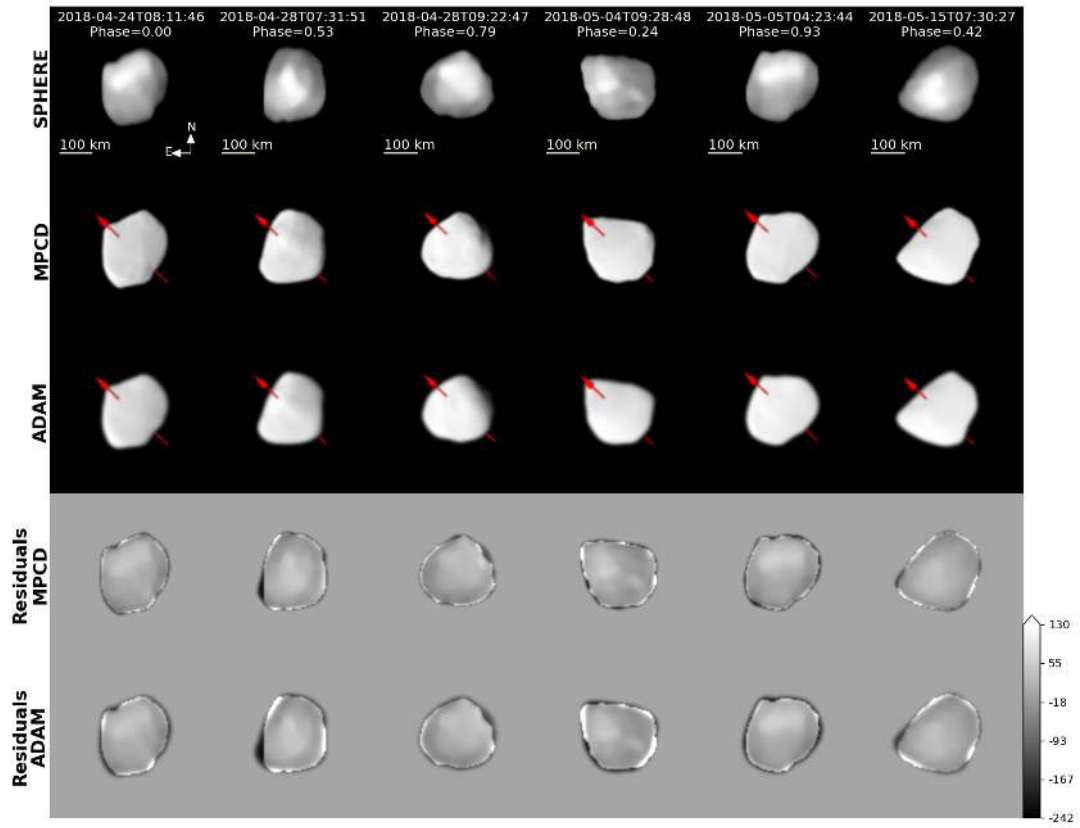
Fig. B.12: (13) Egeria.
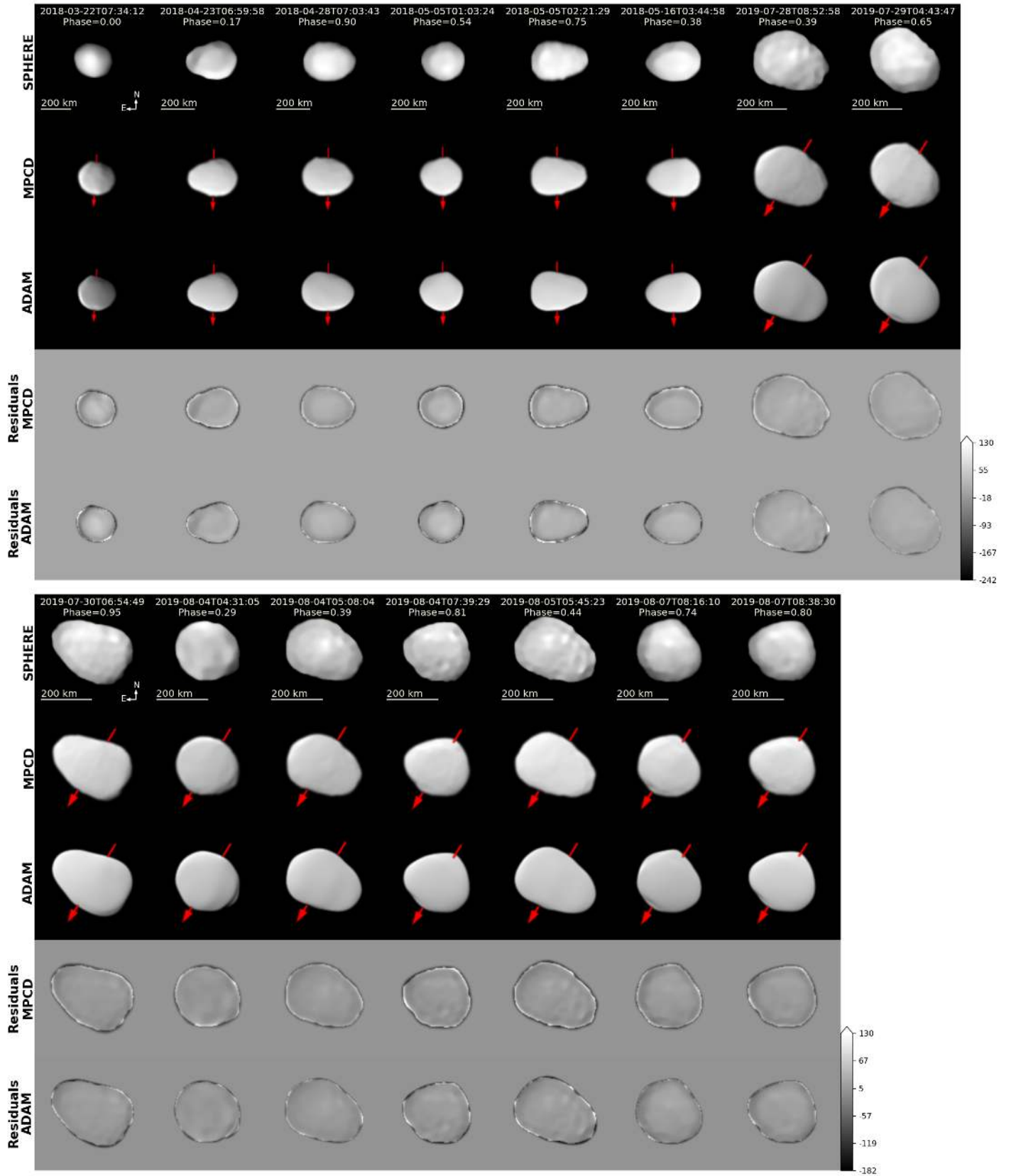
Fig. B.13: (15) Eunomia.
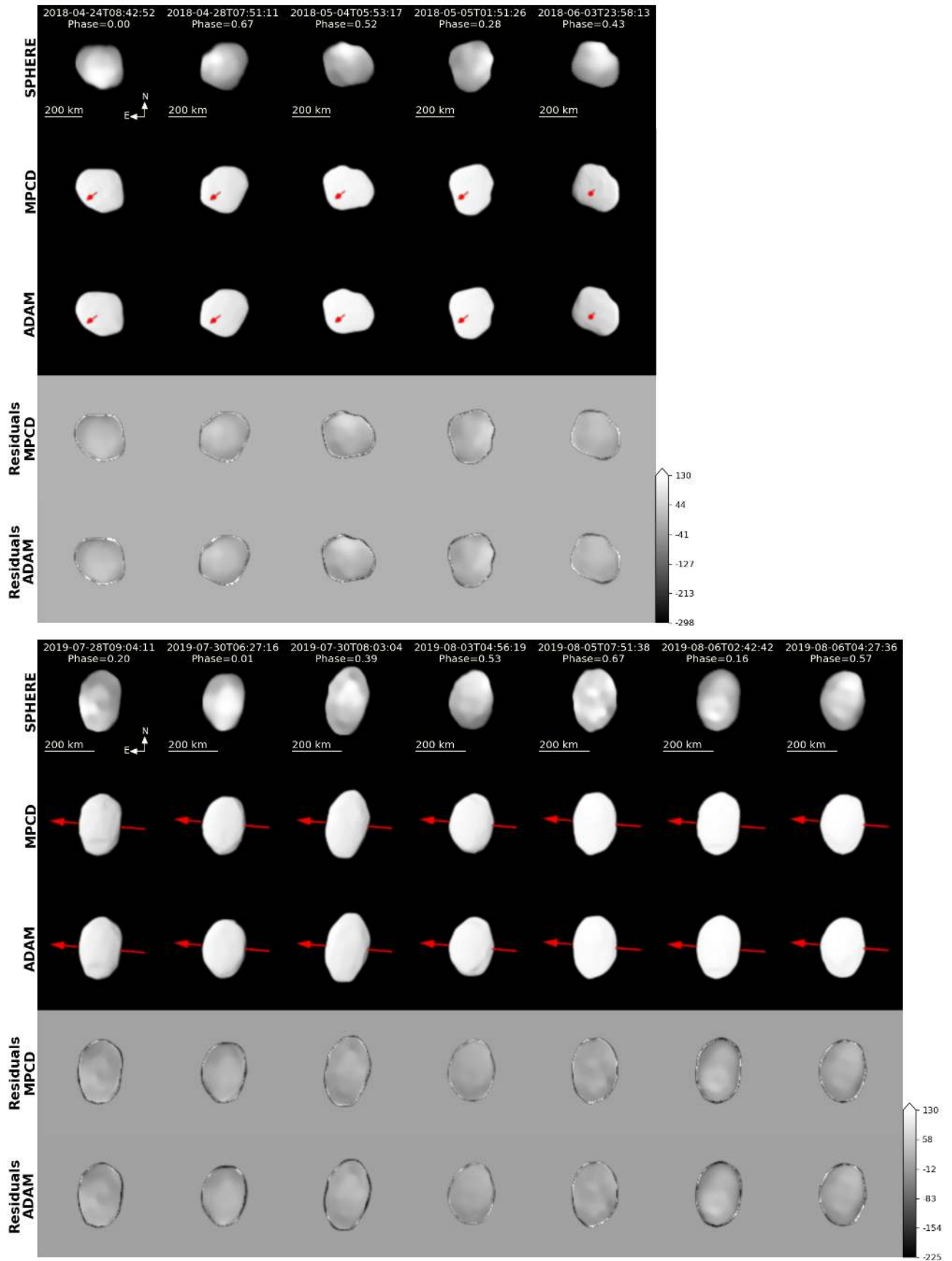
Fig. B.14: (16) Psyche.
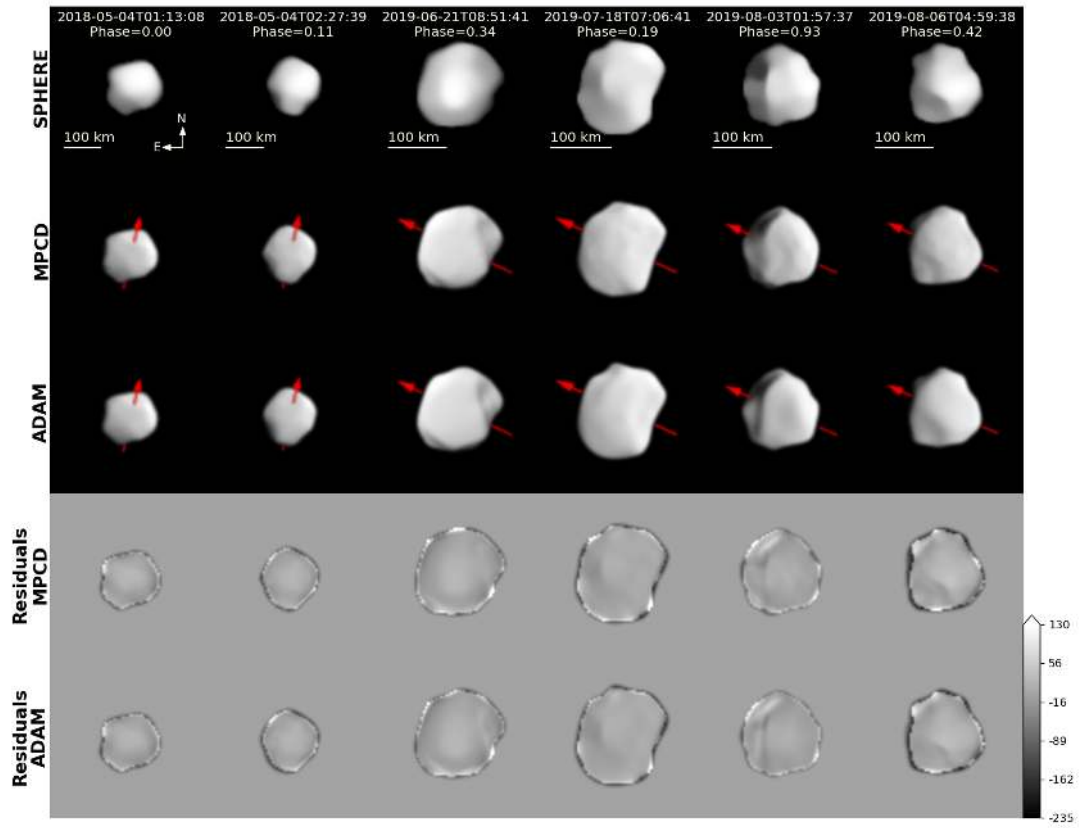
Fig. B.15: (18) Melpomene.
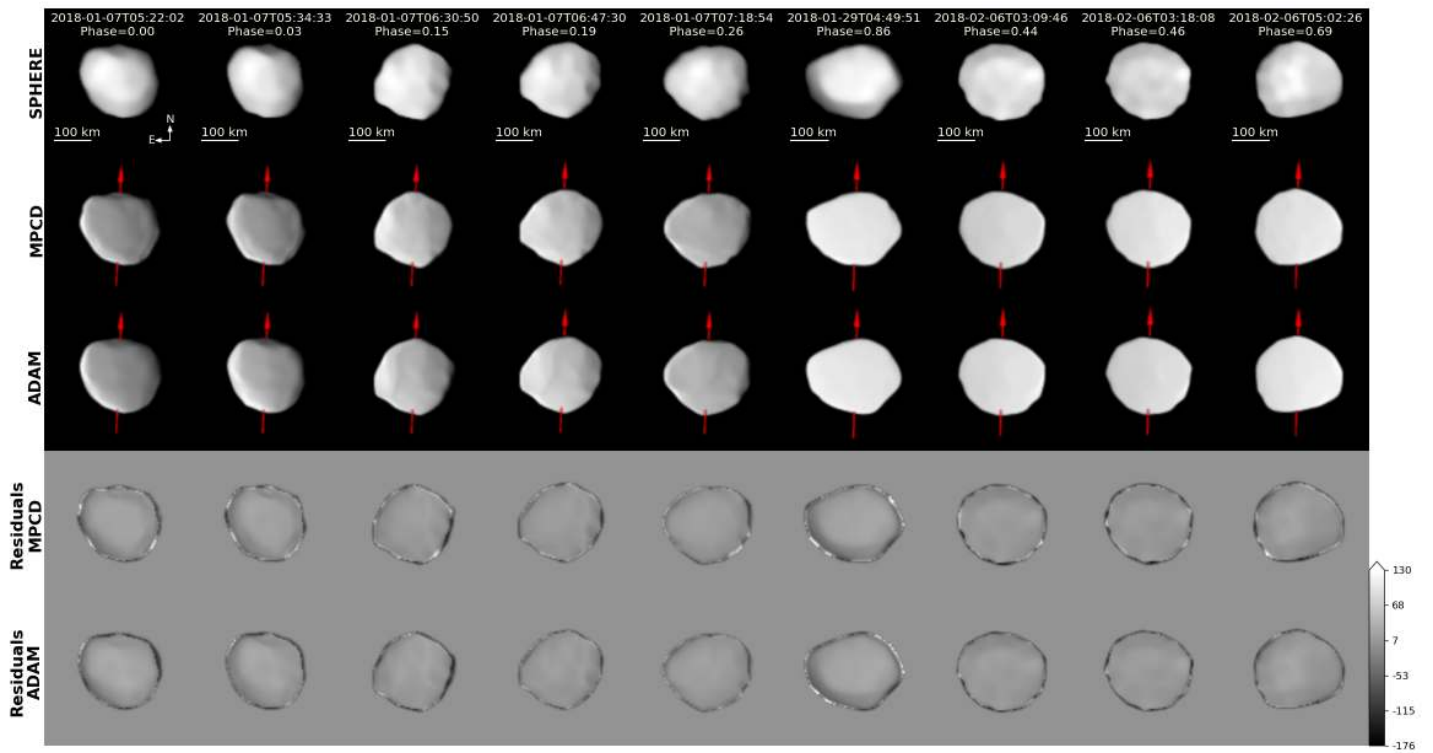
Fig. B.16: (19) Fortuna.
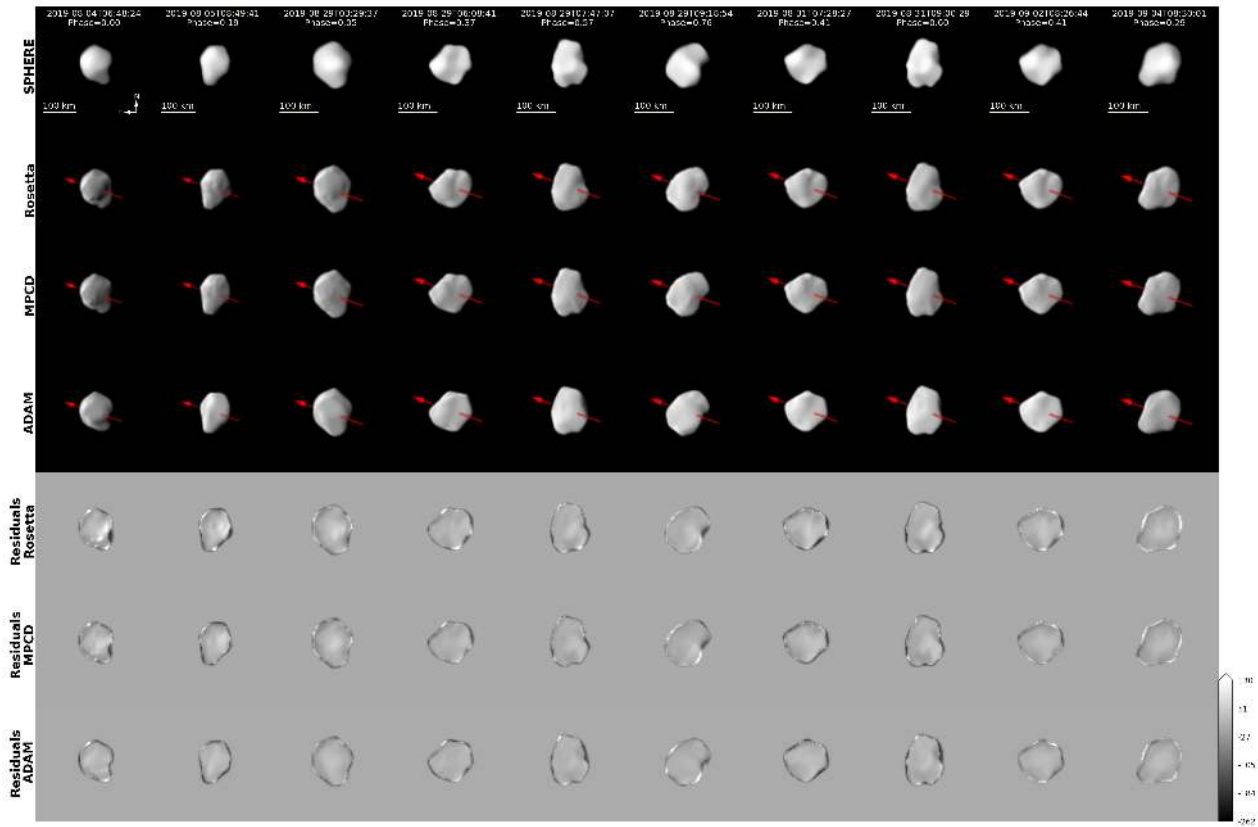
Fig. B.17: (21) Lutetia.
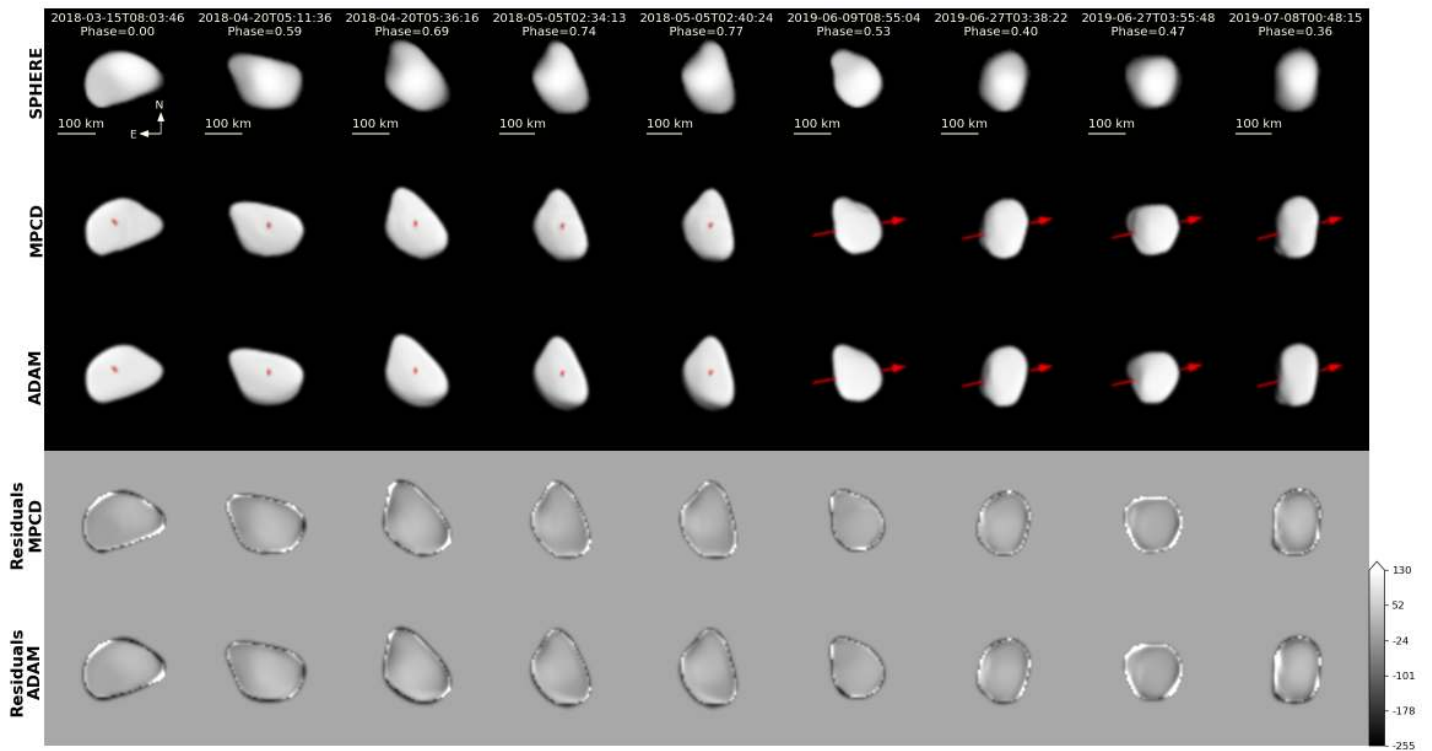
Fig. B.18: (22) Kalliope.
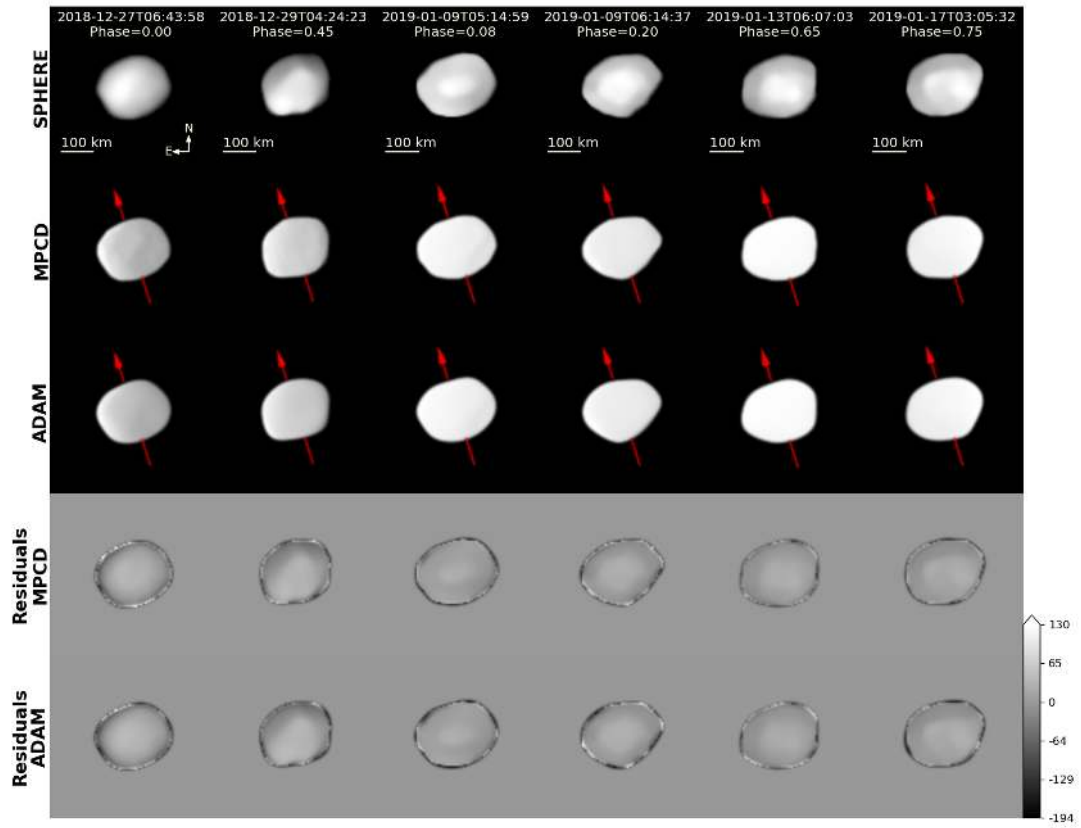
Fig. B.19: (24) Themis.
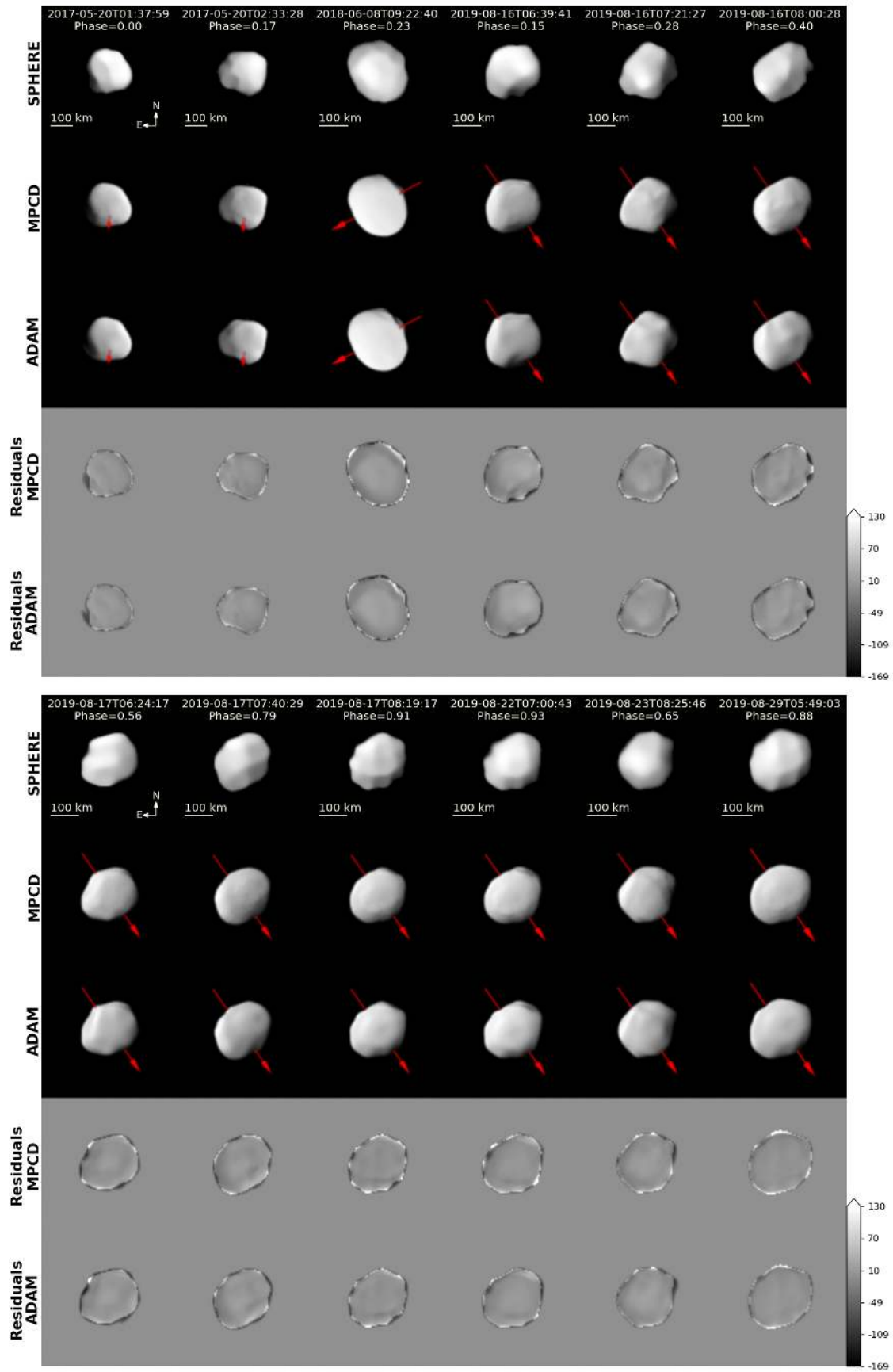
Fig. B.20: (29) Amphitrite.
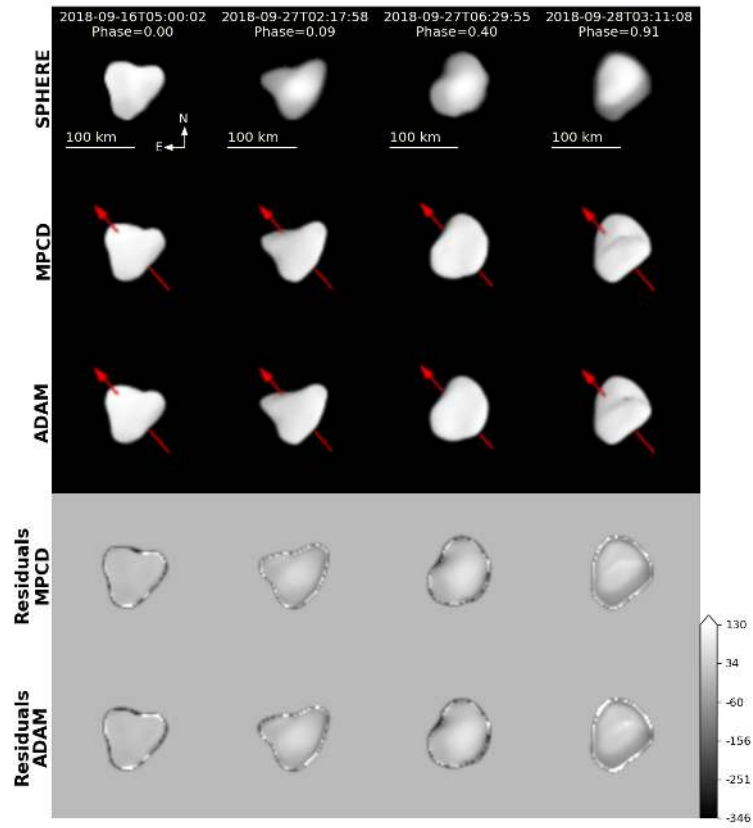
Fig. B.21: (30) Urania.
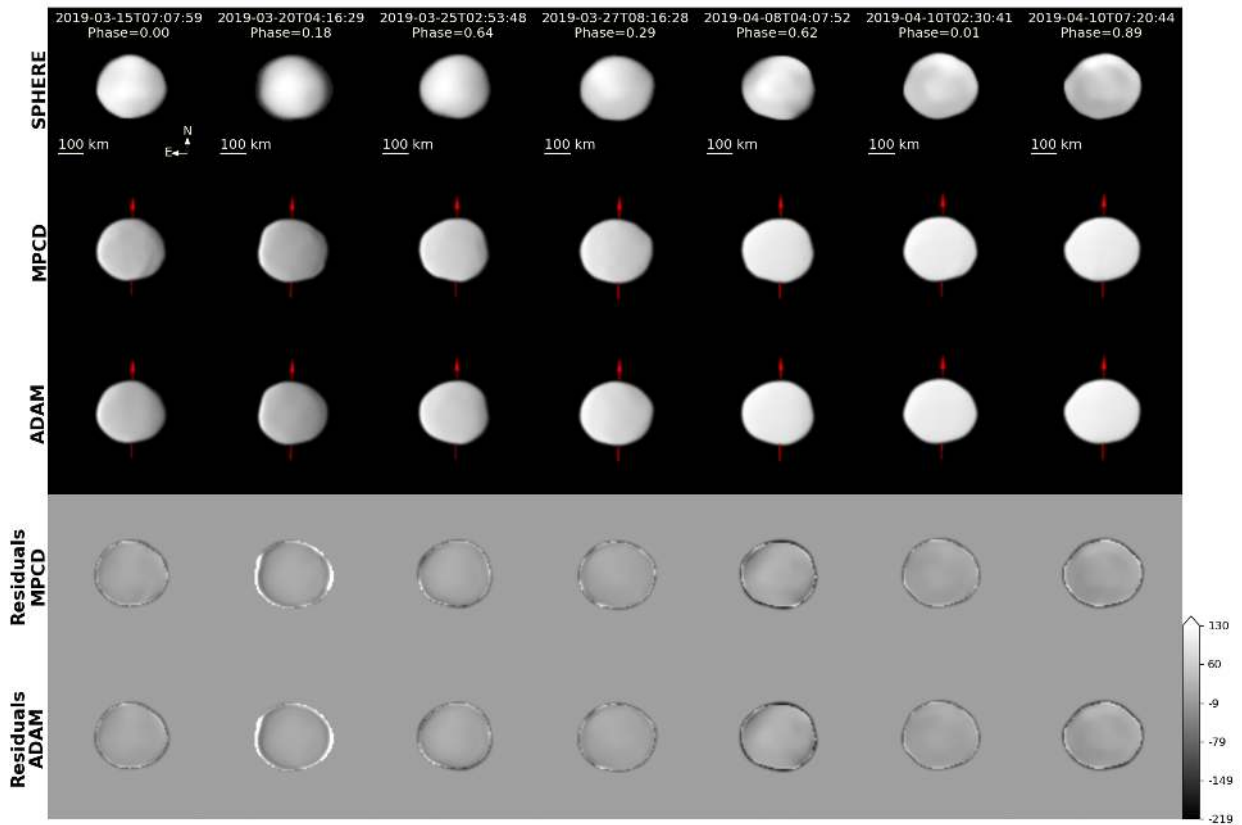
Fig. B.22: (31) Euphrosyne.
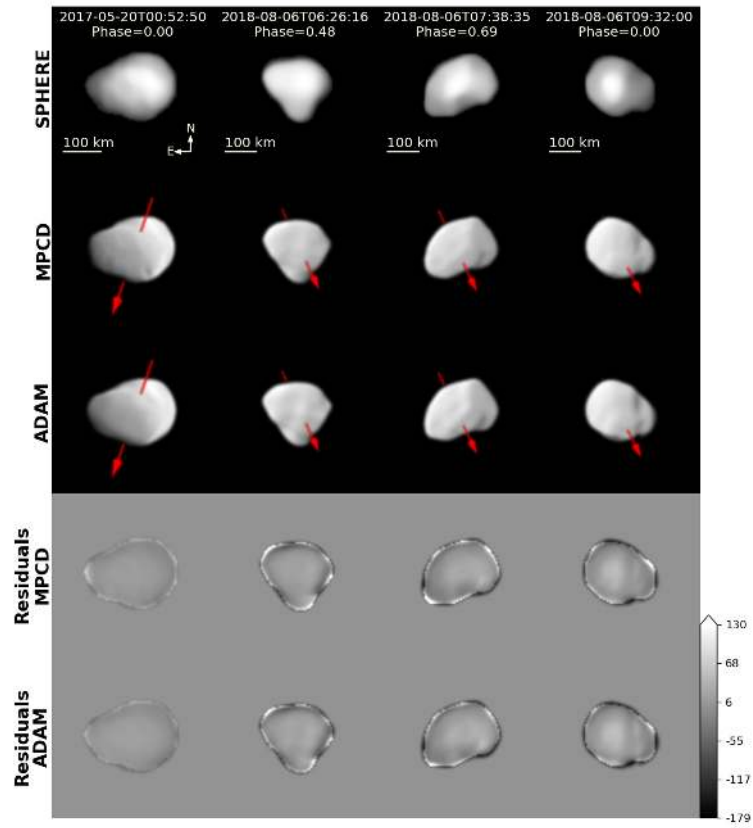
Fig. B.23: (41) Daphne.
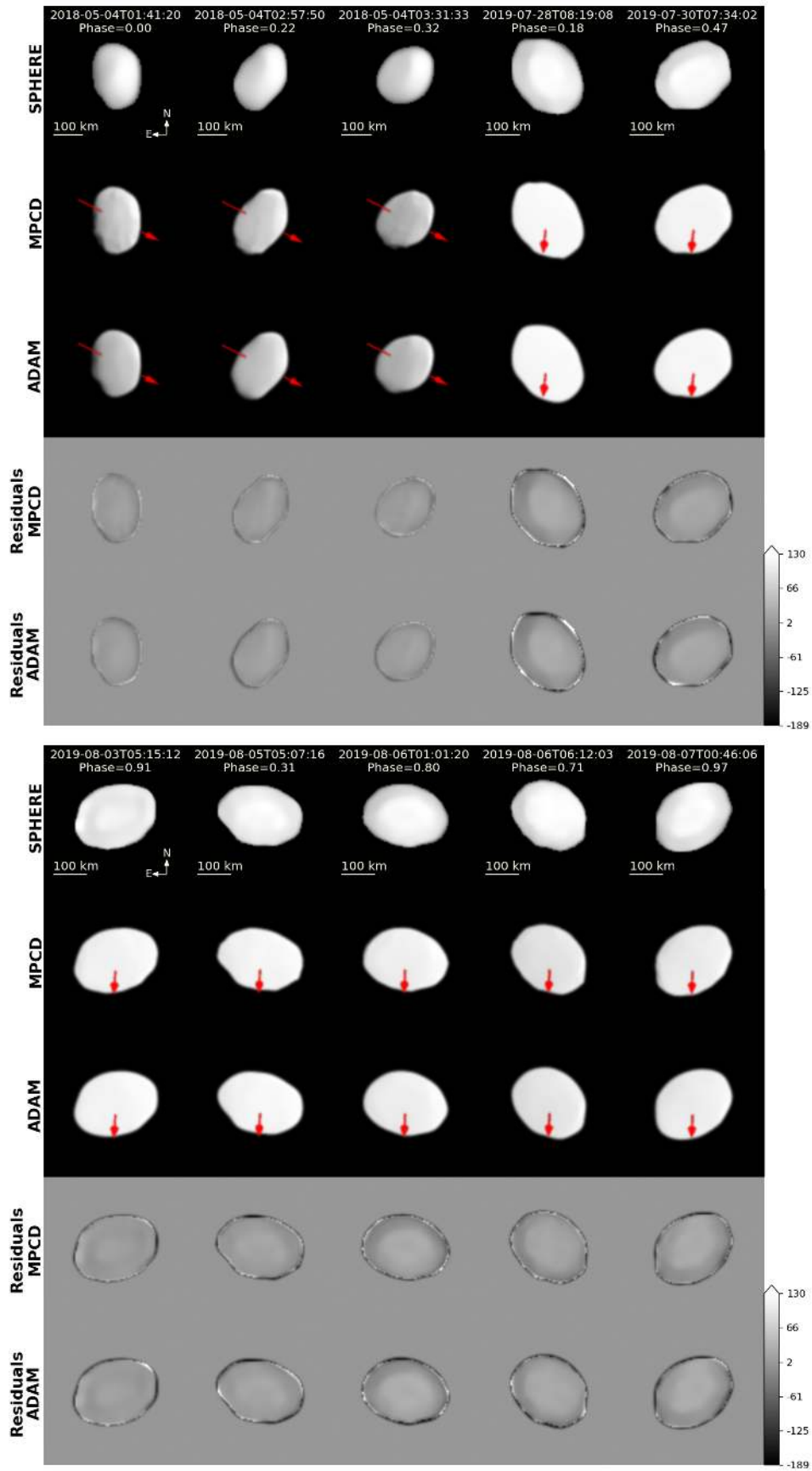
Fig. B.24: (45) Eugenia.
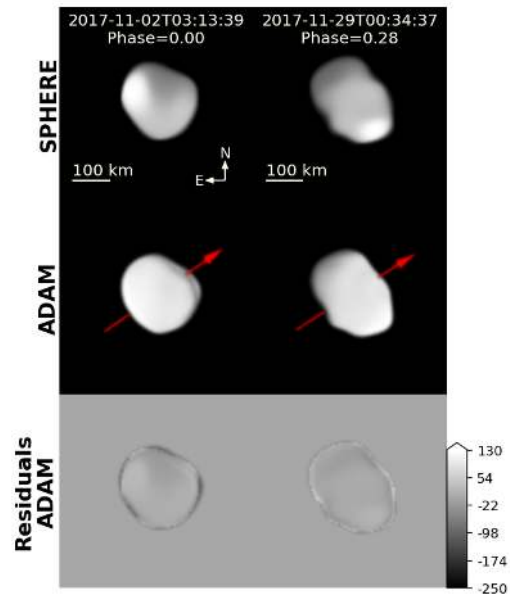
Fig. B.25: (48) Doris.
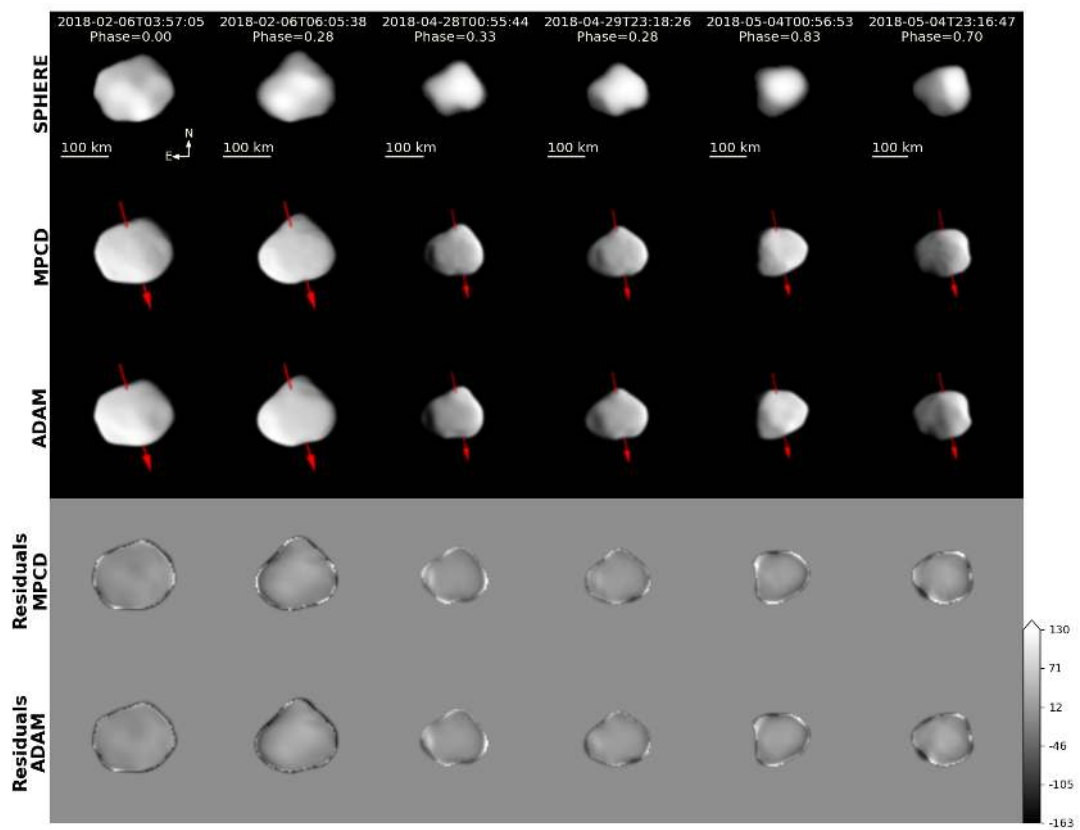
Fig. B.26: (51) Nemausa.
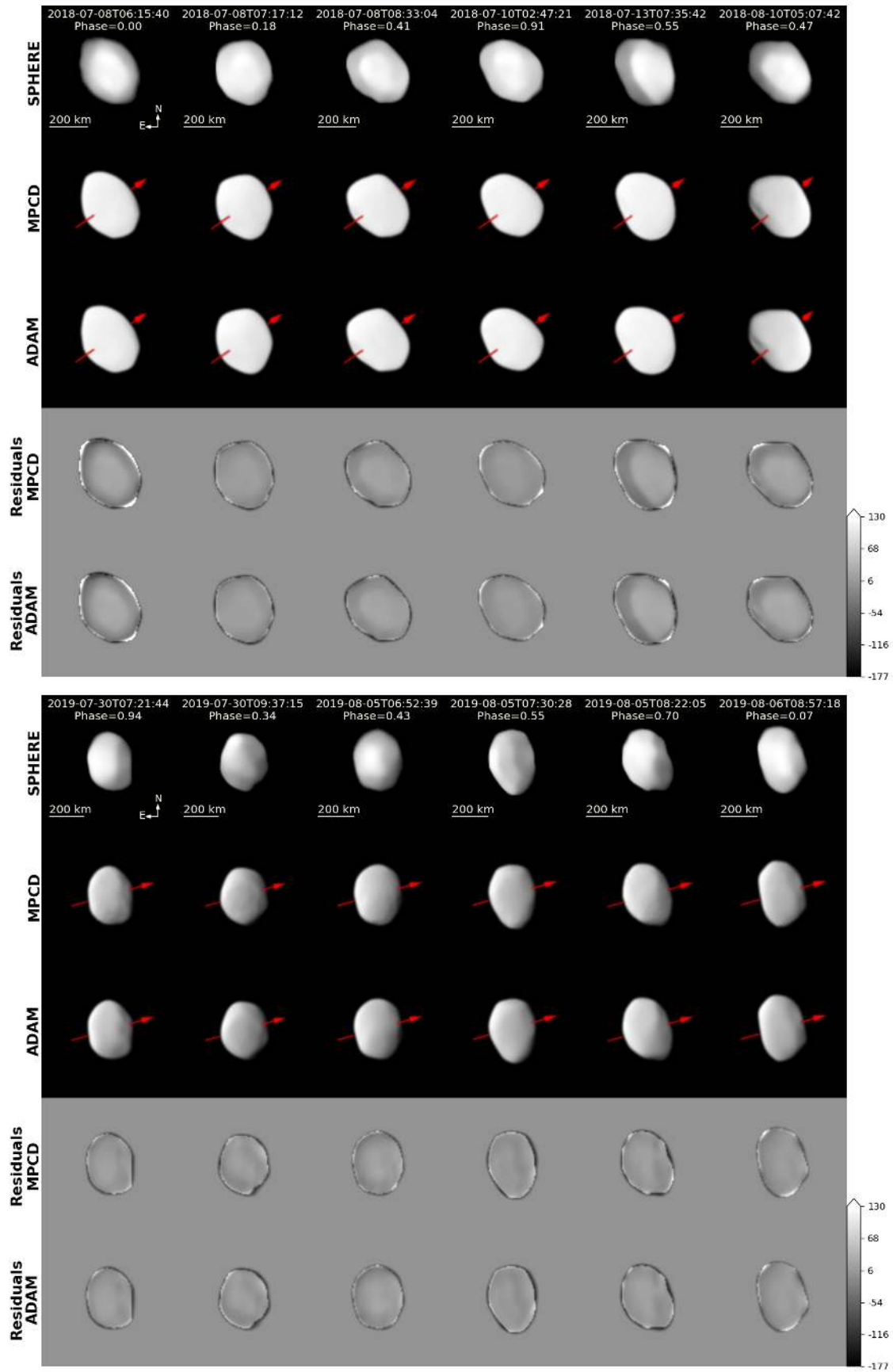
Fig. B.27: (52) Europa.
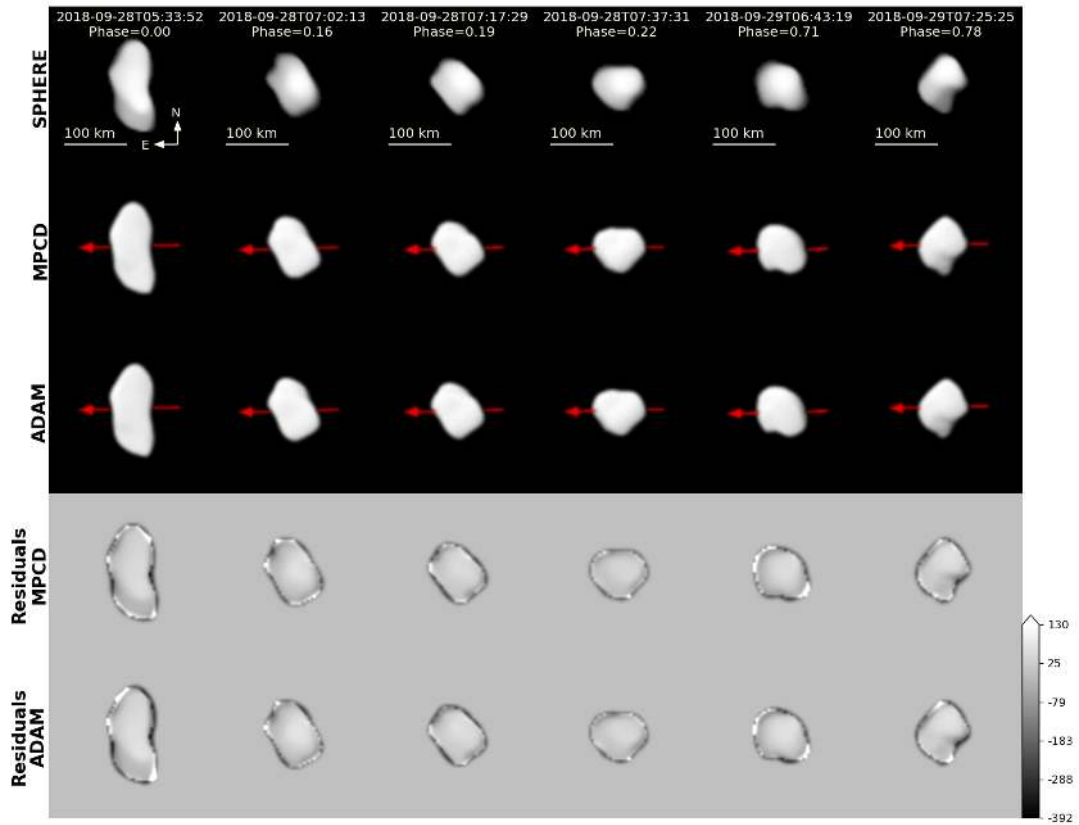
Fig. B.28: (63) Ausonia.
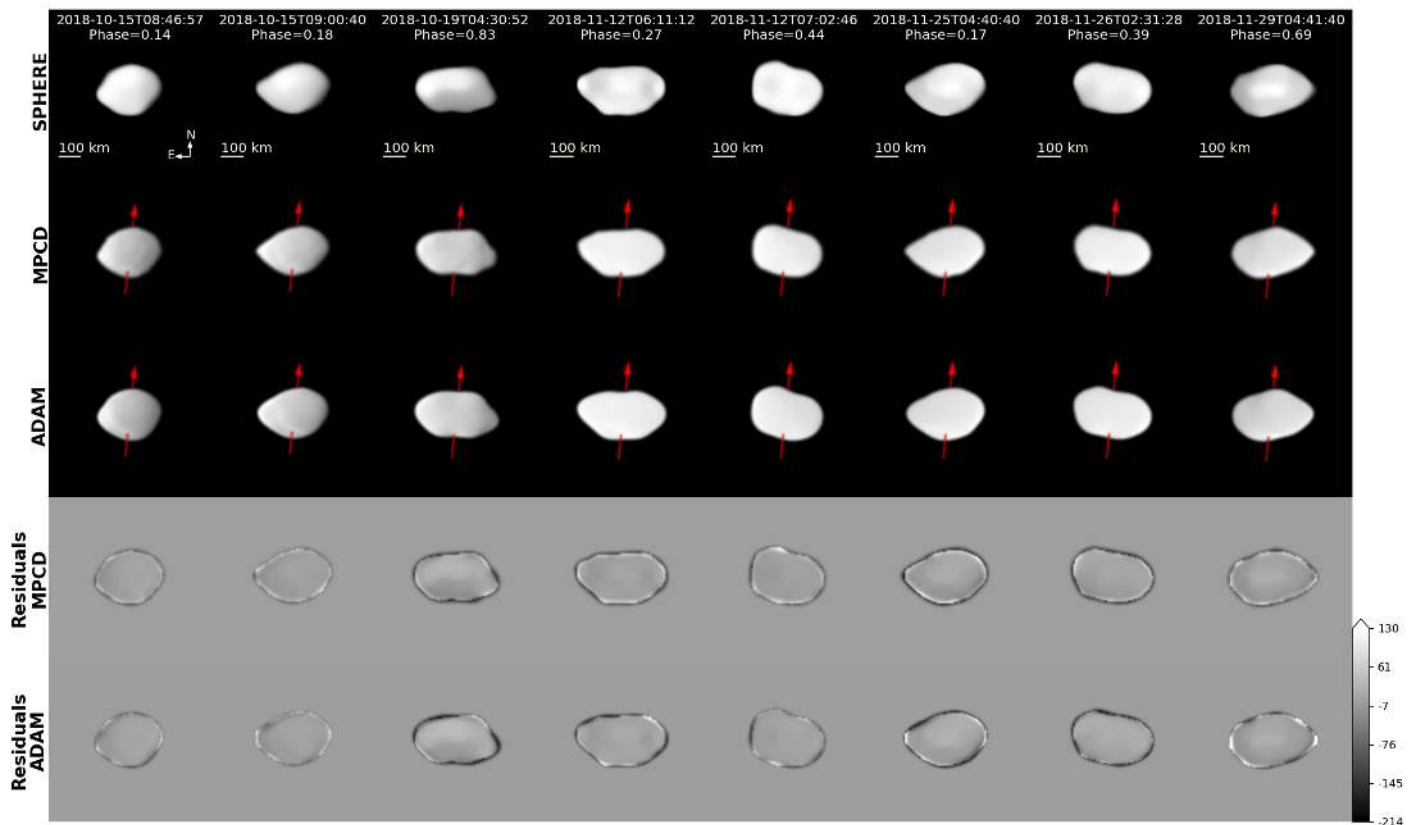
Fig. B.29: (87) Sylvia.
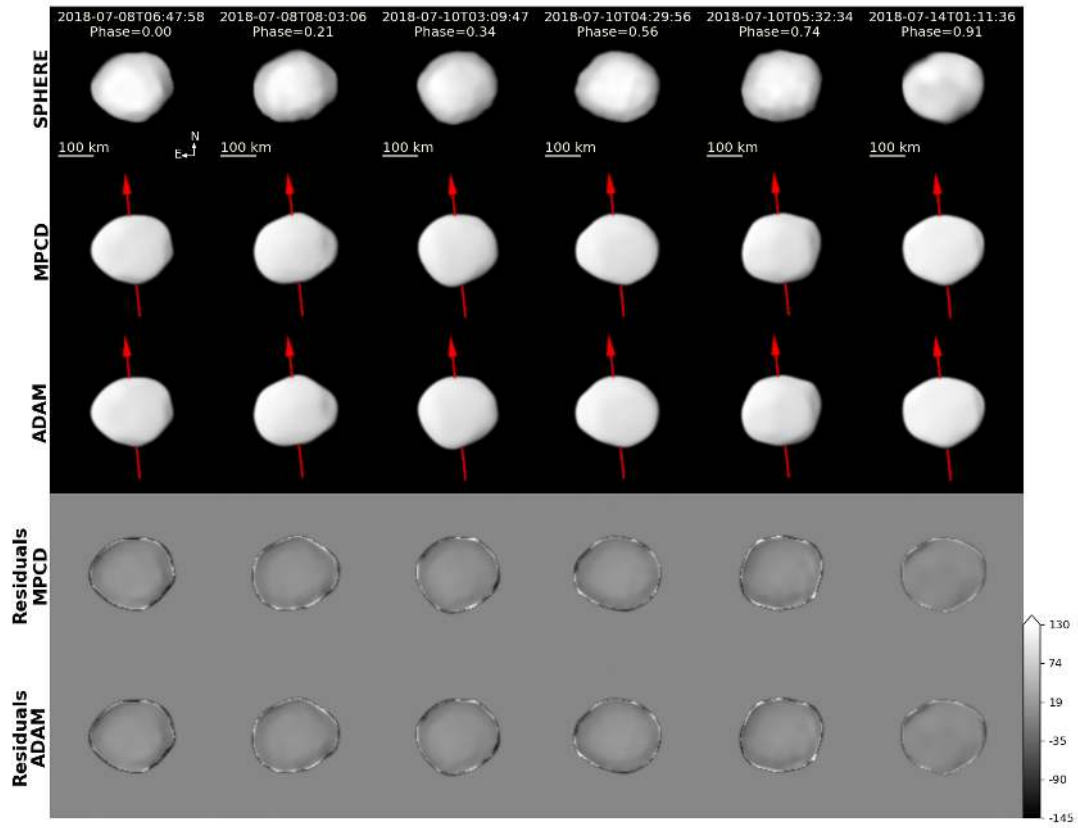
Fig. B.30: (88) Thisbe.
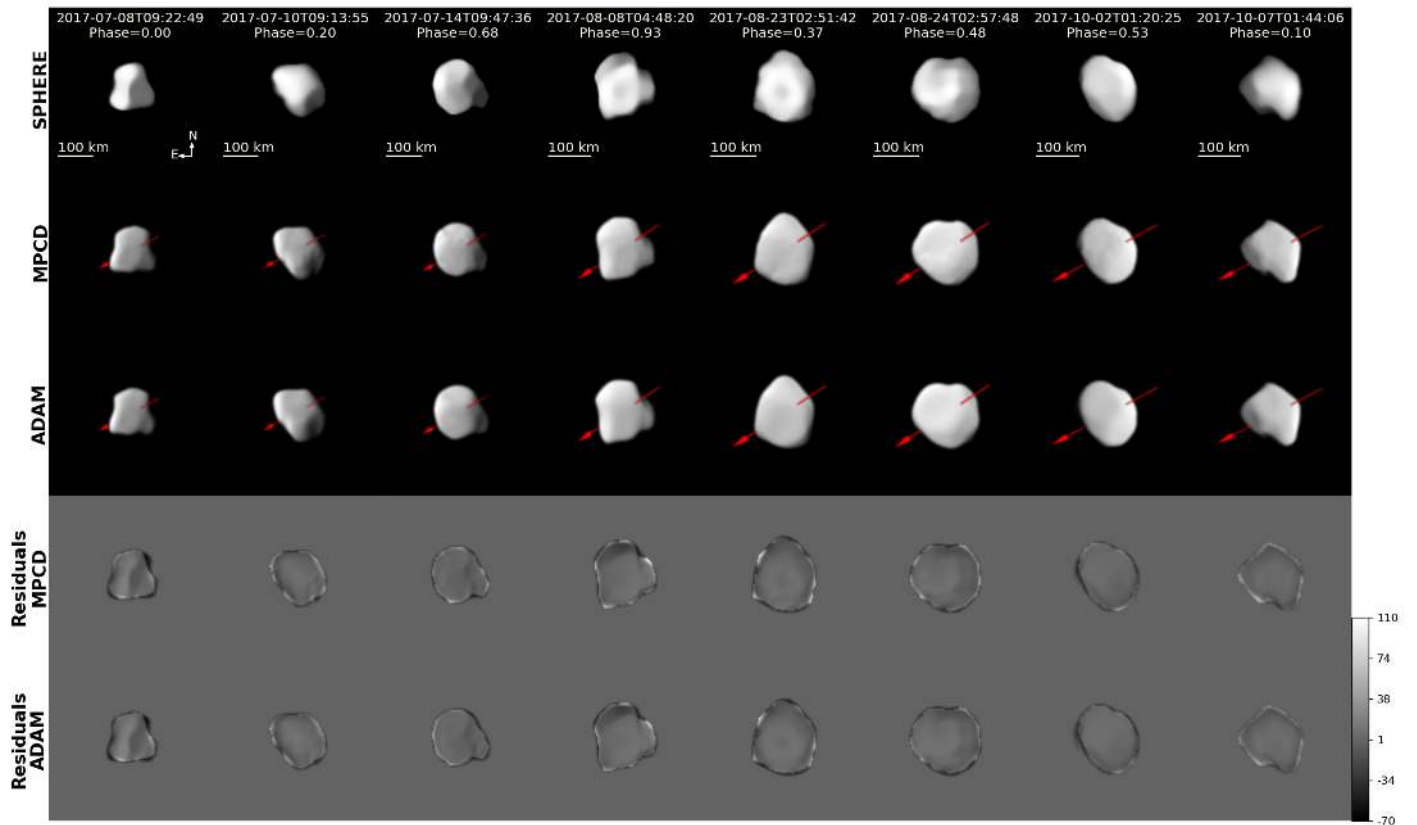
Fig. B.31: (89) Julia.
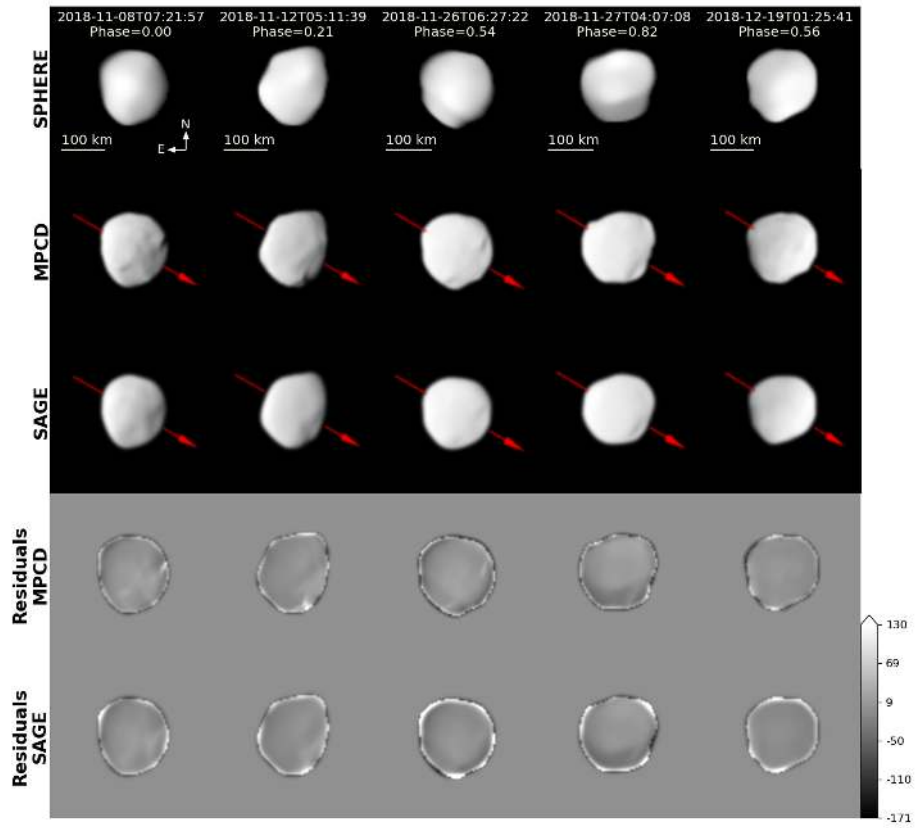
Fig. B.32: (128) Nemesis.
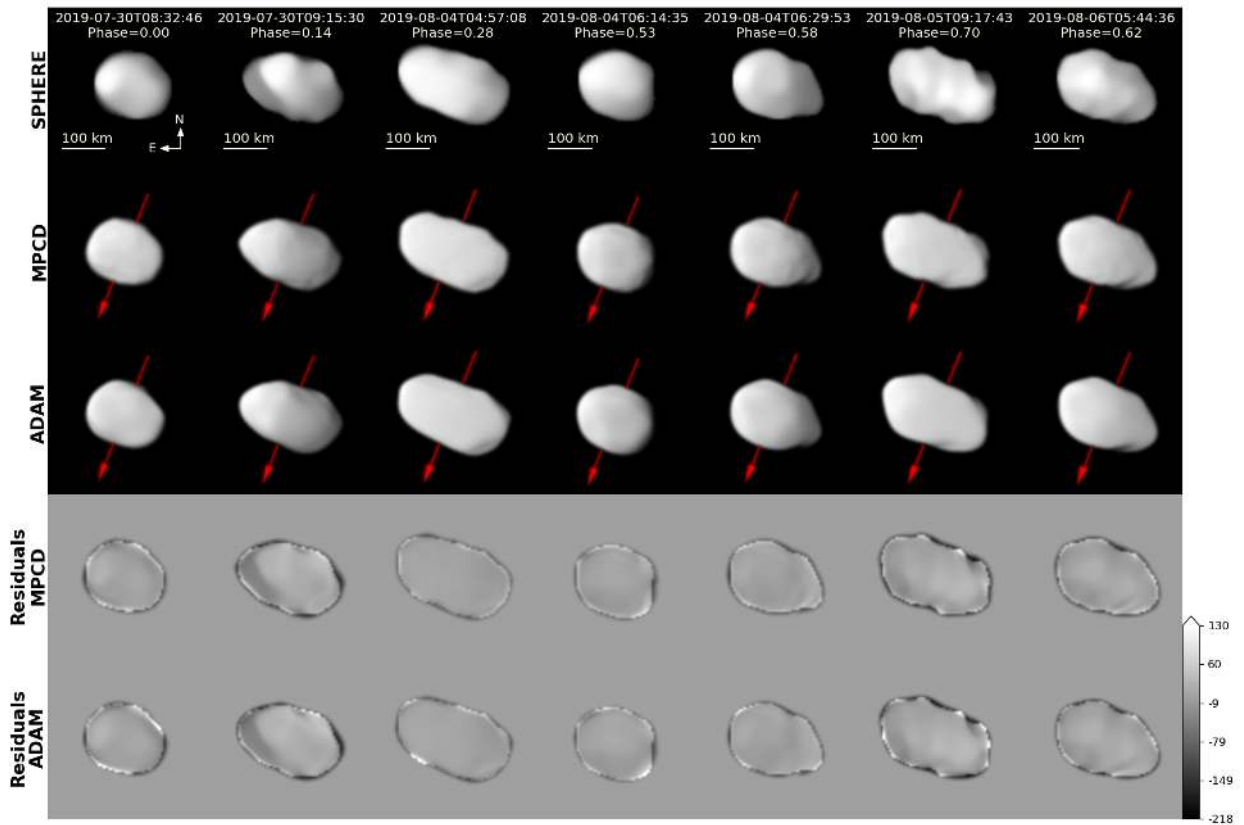
Fig. B.33: (130) Elektra.
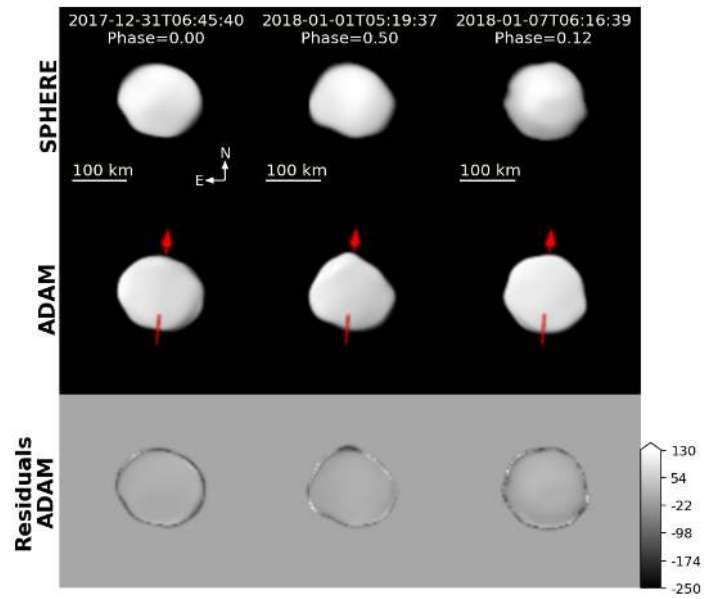
Fig. B.34: (145) Adeona.
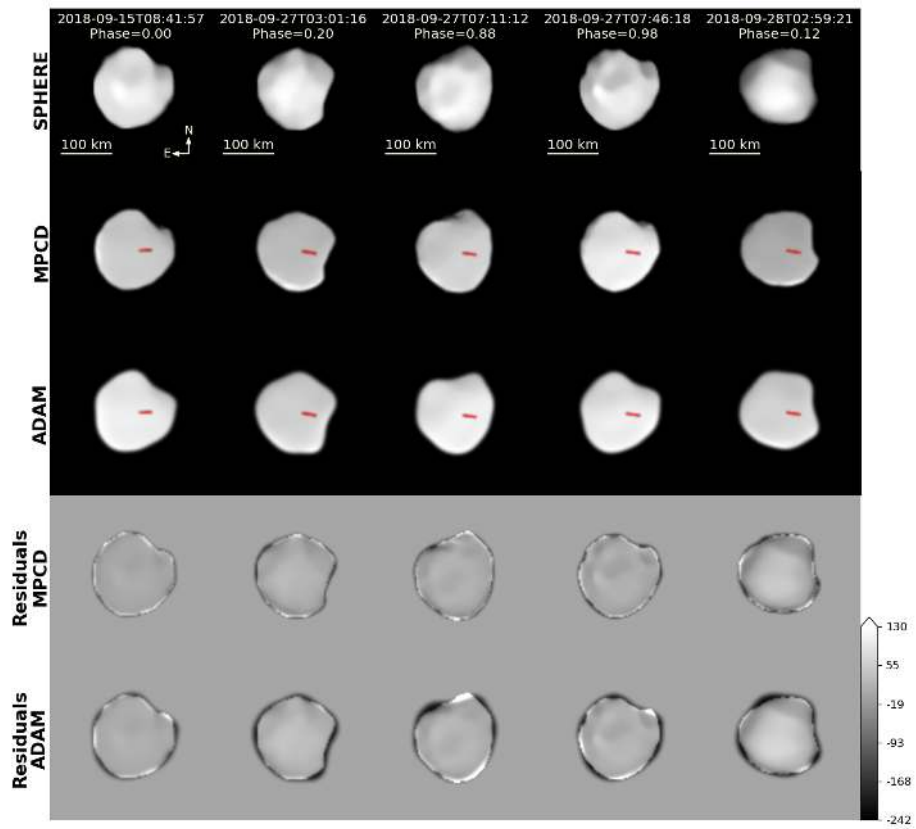
Fig. B.35: (173) Ino.
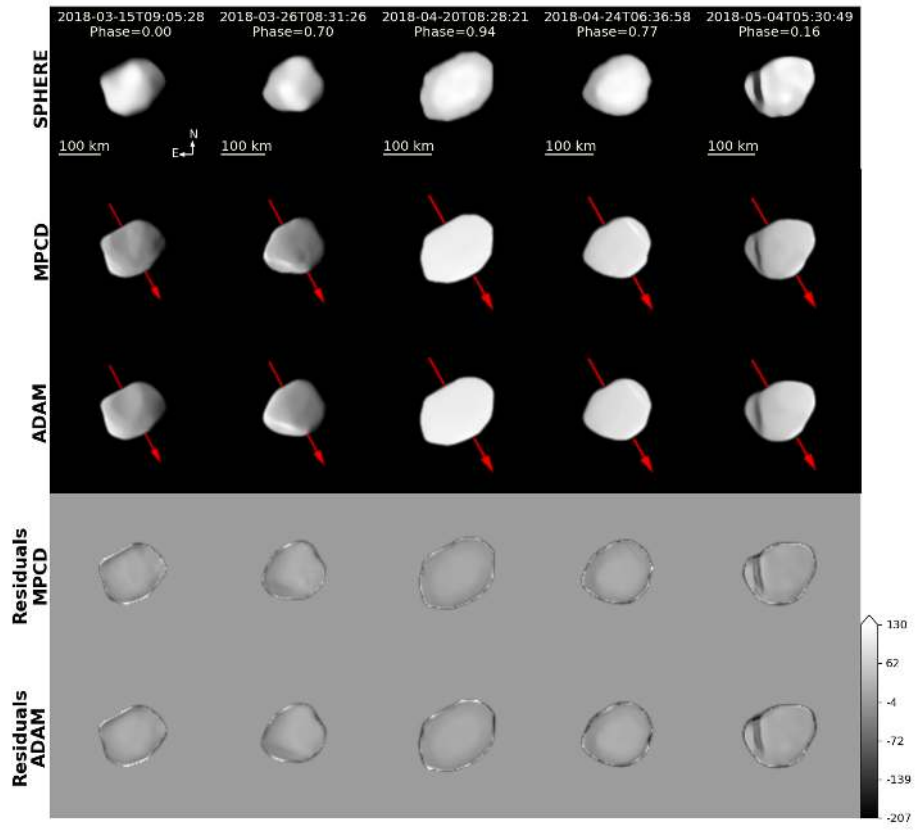
Fig. B.36: (187) Lamberta.
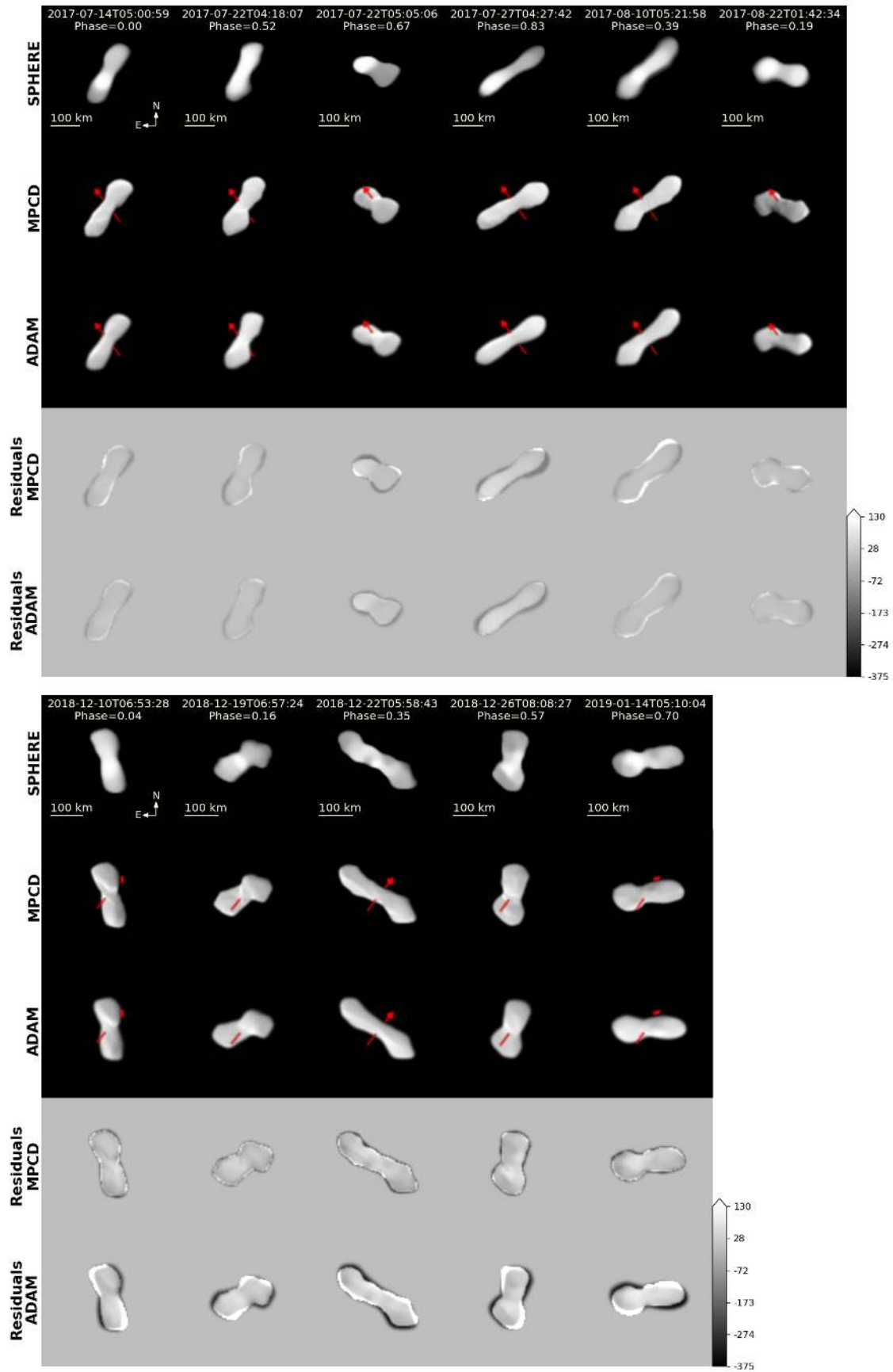
Fig. B.37: (216) Kleopatra.
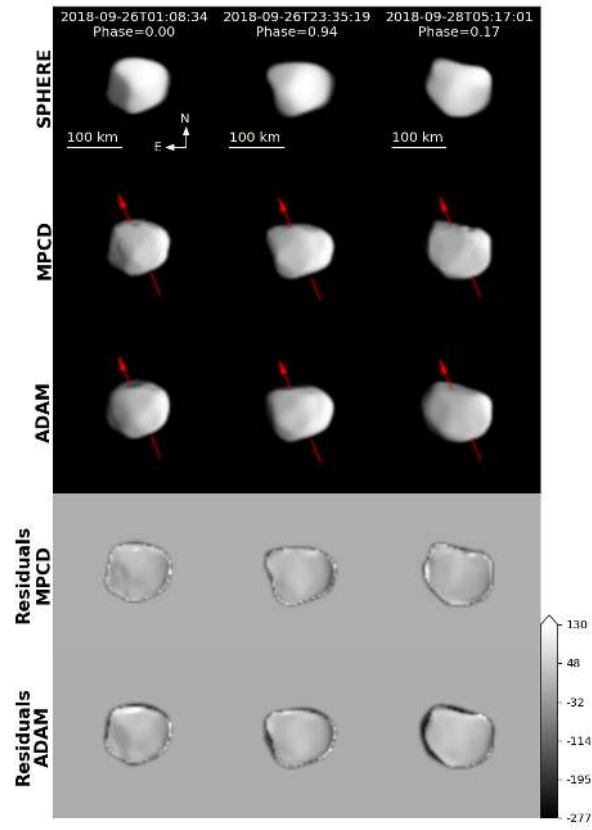
Fig. B.38: (230) Athamantis.
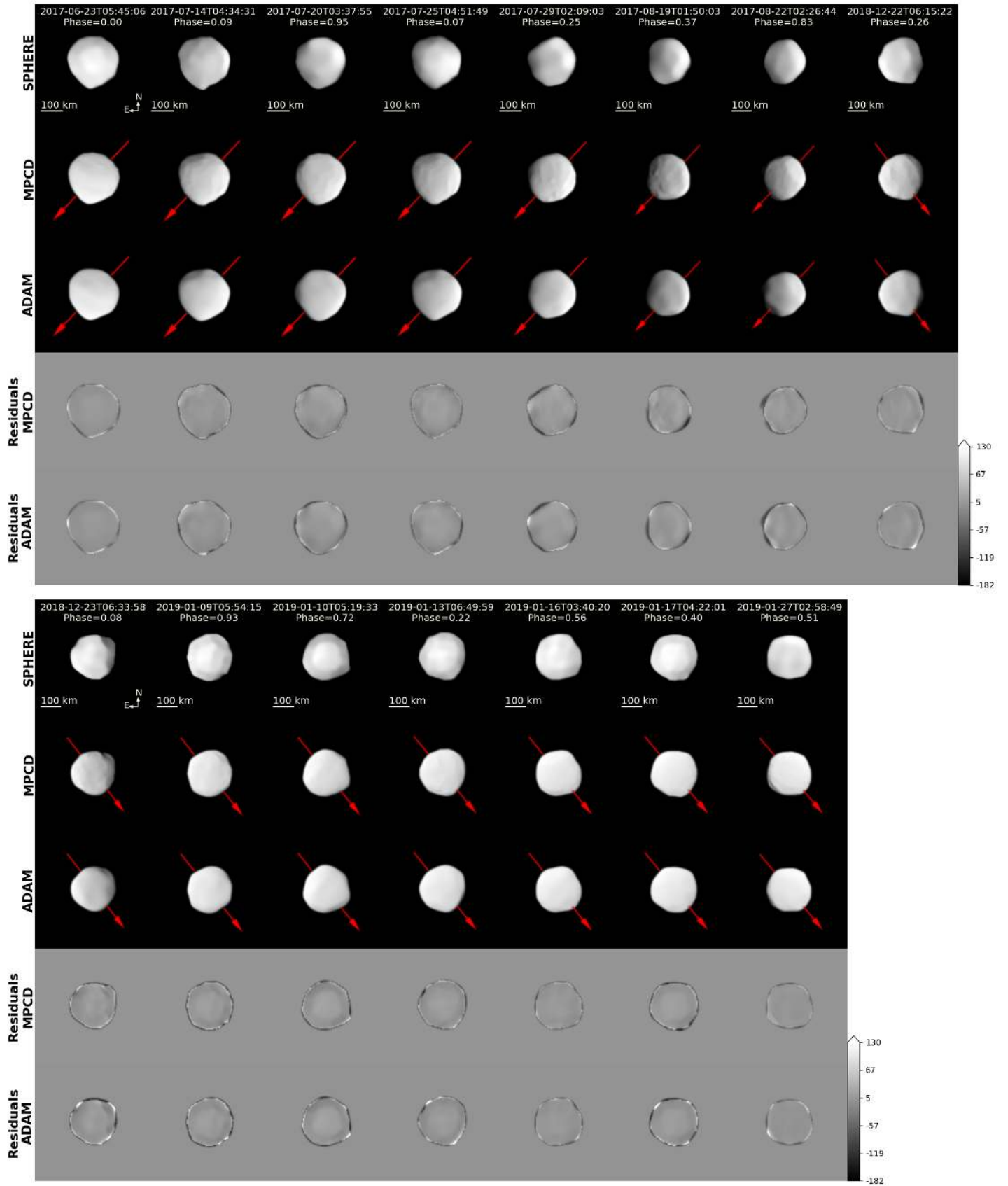
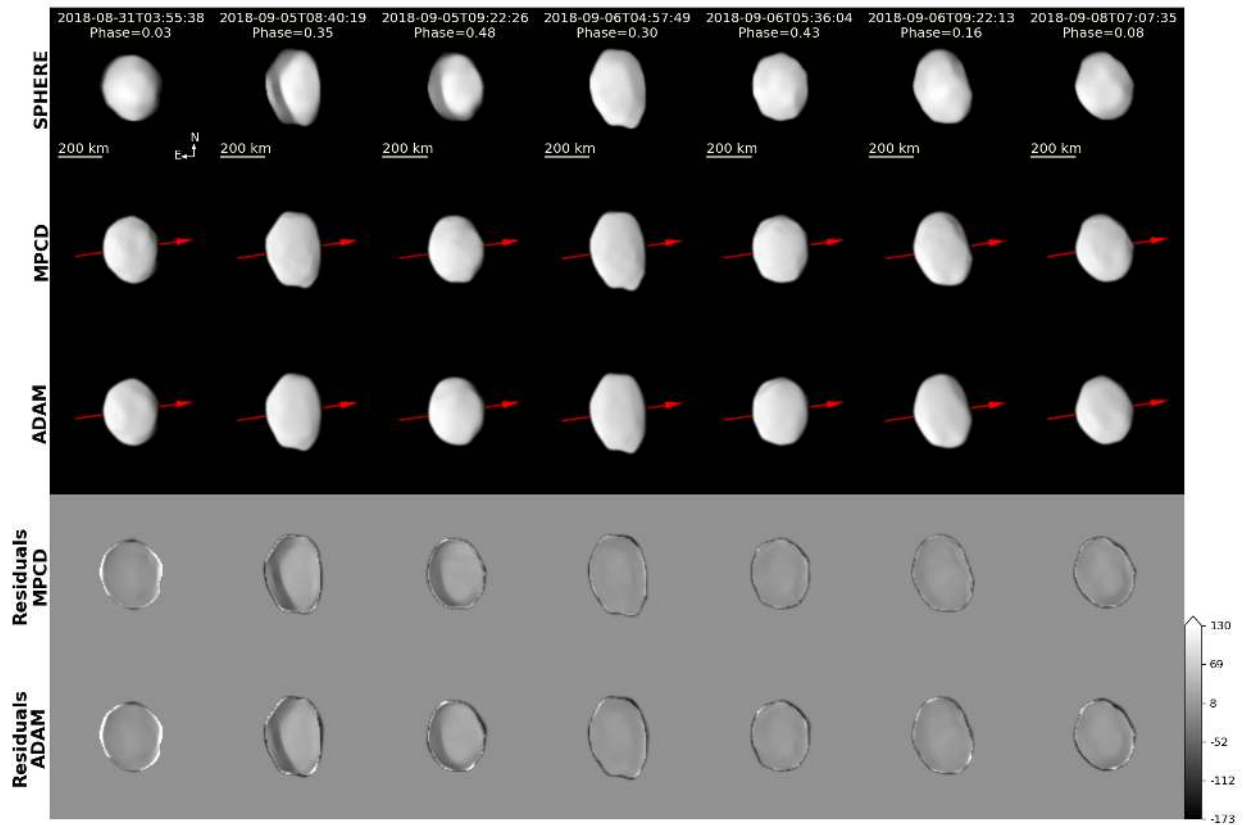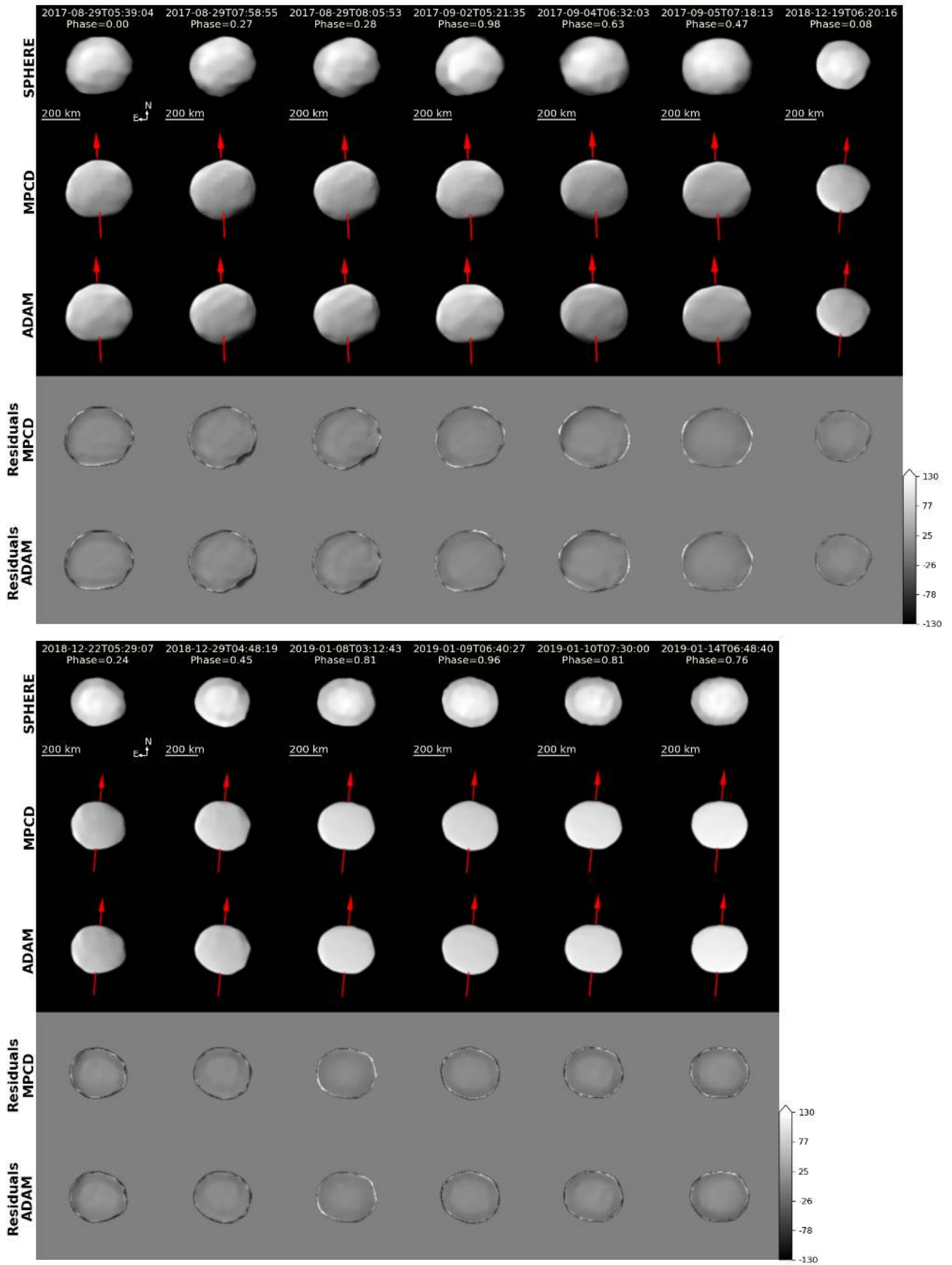**Fig. B.39:** (324) Bamberga.
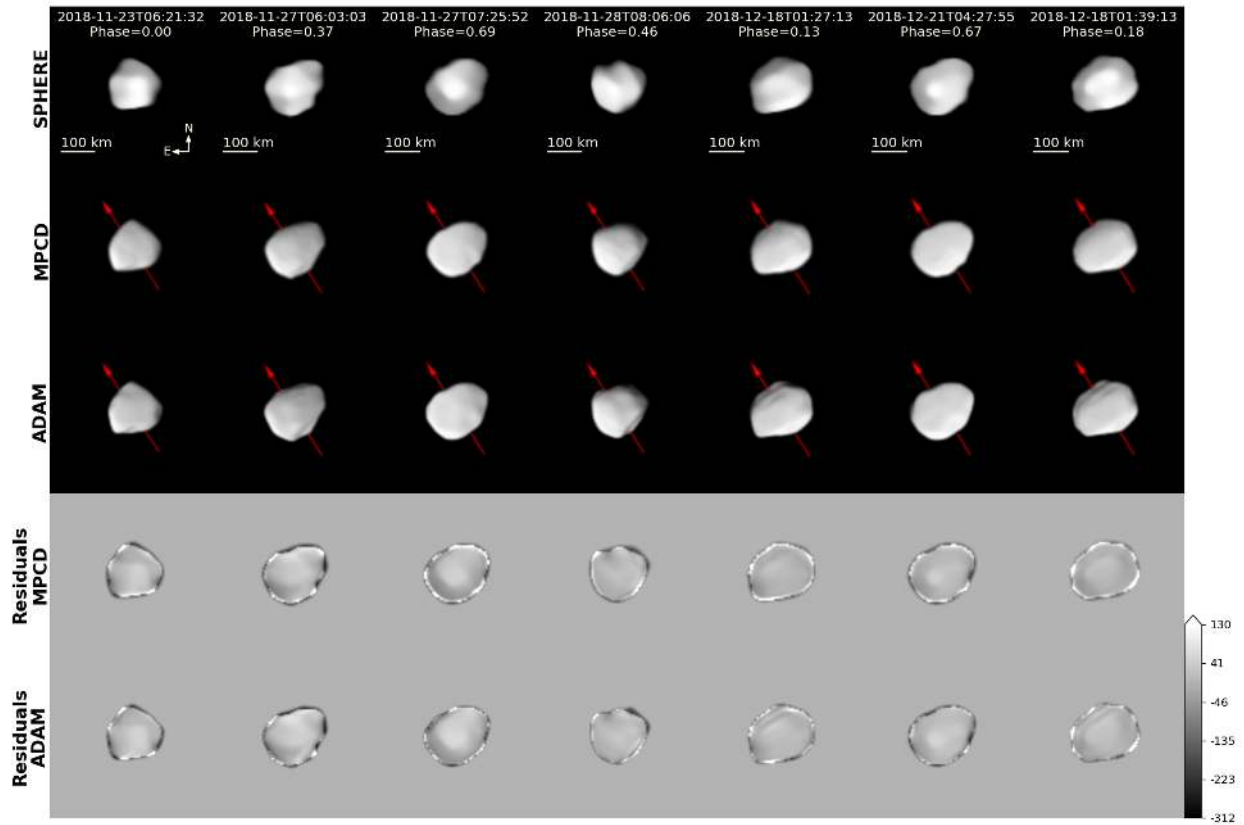
Fig. B.40: (354) Eleonora.

Fig. B.41: (511) Davida.

Fig. B.42: (704) Interamnia.